The impact of scattering-induced atomic motion on temperature measurements of Bose-Einstein Condensates

Paul N. Summers

A thesis submitted for the degree of
Master of Philosophy in Physics at
The Australian National University

July, 2008


THE AUSTRALIAN
LIBRARY
NATIONAL UNIVERSITY

Declaration

This thesis is an account of research undertaken between February 2006 and December 2007 at The Department of Physics, College of Science, The Australian National University, Canberra, Australia.

Except where acknowledged in the customary manner, the material presented in this thesis is, to the best of my knowledge, original and has not been submitted in whole or part for a degree at any university.

Paul N. Summers
July, 2008

Acknowledgements

"Life is short, and the Art long; the occasion fleeting; experience fallacious, and judgement difficult."

- Hippokrates of Kos

Firstly, I would like to thank John Close for the opportunity to study with the Atom Laser group, his patient supervision and assistance, his efforts in providing valuable feedback on the drafts of this thesis and of course, the occasional axe grind. I would also like to thank Nick Robins and Cristina Figl for all their supervision and assistance in the lab, help with aspects of the numerical model, Wee Jasper camps and many a hearty roast. Thanks also to Joe Hope for his time and valuable assistance with the theoretical analysis presented in Chapter 2; the analysis provided a solid foundation upon which the numerical model was validated. I'm also grateful to colleagues with whom I shared an office; you provided an enjoyable and stimulating environment to work in, as well as enjoyable house parties and the occasional night out on the town. For their essential help in developing many Matlab skills, I'd also like to thank Mattias Johnsson, Graham Dennis and Matthew Jeppesen - thanks for your patience and enduring the endless questions! I depart the group wiser and with more skills - oh, and a neurological imprint of the words "signal to noise", chanted to Bheethoven's Symphony No. 5. Wise words indeed!

I would also to thank my families. Firstly to my partner Sarah Giufrè, who selflessly made personal sacrifices, relocated to Canberra and supported me throughout my years of study; thank you so much. Thank you also to Manny & Karen Giufrè, Lisa Giufrè and Subik Baso for their support throughout my study and their visits to Canberra; your support is greatly appreciated. Almost last, and most certainly not least, I would like to thank my parents, Michael & Valerie Summers, my brother Greg Summers and my grandmother Marjory Bourke. I would like to thank you for your unconditional love and support in all my pursuits and for teaching me that the most important lessons in life are those learnt through example. You inspire me to be a better person.

Finally, thanks also to: Stephan, Dan, Leah, the altar ego that is Juicer-M, Russ, Rob, T-Bone, Avril, Hughes, Mike, Rosh, Fatty & Simone, Carl & Mel, Nick & Kim, Jesse, Simon, Phelan, Peter Johnston and the welcoming arms of the city of Melbourne.

This thesis is dedicated to the loving memory of grandmother, Marjory Bourke.

Abstract

The temperature measurement of a Bose-Einstein Condensed cloud of atoms is a unique process, owing to the equally unique nature of Bose-Einstein Condensates (BEC). Temperature is inferred from a bimodal fit of the column-density distribution of a BEC, usually obtained from an absorption image. The relative size of each mode is directly related to the temperature of the BEC. Not considered in the fitting functions currently used to obtain temperature is the effect of atomic motion due to the scatting of photons during the imaging process. The aim of this study is to determine if and when this atomic motion affects the temperature measurement process and consequently if an optimal imaging regime can be found.

Contents

List of Figures

List of Tables

Chapter 1

Introduction

"...when I read that water boils at a definite degree of heat, I immediately felt a great desire to make myself a thermometer so that I might examine with my own eyes this beautiful phenomenon of nature and be convinced of the truth of the experiment..."

- Daniel Gabriel Fahrenheit

The primary physical parameter calculated and measured in the present study is temperature, specifically in the context of absorption imaging of Bose-Einstein condensates (BECs). In this chapter, the key theoretical and experimental papers outlining the development of Bose-Einstein condensation are presented, followed by the motivation for the present study. Further, BECs constitute a unique primary thermometer. To place this in historical context, a brief history of temperature and primary thermometry is then discussed. Finally, techniques for measuring the temperature of BECs are explored.

1.1 Introduction and study motivation

Bose-Einstein condensation was first verified in 1995, when several groups observed the phenomenon in atomic vapours of rubidium [1], lithium [11], and sodium [15]. The ability to produce a coherent, macroscopic sample of atoms occupying the same quantum state offered the prospect of many new avenues of research; indeed, the field of atom optics has boomed since.

As Anderson *et al* point out in their seminal experimental paper [1], a key signature of Bose-Einstein condensation is the narrow atomic density peak, centered at zero velocity, which appears atop a broad thermal velocity distribution. Further, the fraction of atoms in this peak increases rapidly below a critical temperature T_c. These features of Bose-Einstein condensation were not only a means of validating that condensation had been observed, but are also intrinsicly linked to the temperature of the system (discussed at length in section 1.4.2). As the temperature of the system can be extracted from the atomic density distribution alone, a Bose-condensed system constitutes a primary thermometer, as the system being measured does not need to be calibrated against some other known quantity.

As a primary thermometer, the Bose-Einstein condensate is historically unique. To fully appreciate the context of BEC in primary thermometry, a brief history of temperature and the development of primary thermometry is given in sections 1.2 and 1.3.

The link between the atomic distribution of a Bose-condensed system and its temperature has its origins in the work of Einstein in 1925 [17]. Building on Bose's work on the statistical mechanics of photons [10], Einstein studied the statistics of 'bosons' with mass,

which resulted in the derivation of the Bose-Einstein distribution (discussed at length in section 1.4.1). These statistics implied that in principle, any number of bosons could occupy the ground state of a particular system if its temperature was low enough. Despite this startling revelation, Bose-Einstein condensation was not a popular subject, possibly because it could not be tested at the time, and also because leading physicists of the day were focussed on the general development of quantum theory.

A resurgence in interest of Bose-Einstein condensation took place in the 1950s, when theoretical developments in the dynamics of liquid Helium led to several papers being published. Huang and Yang studied phase transitions and energy levels of low-temperature many body systems with "hard sphere" interactions [23, 24, 25], while others like Feynman studied the dynamics of a 'two-fluid' model of liquid helium [18]. But this was Bose-Einstein condensation in the context of strongly interacting systems; not the weekly interacting systems commonly studied today, as in the present study. Further, the technology needed to experimentally validate any theoretical studies into BEC had still not been developed.

Advances in atom trapping and cooling made throughout the 1980s re-inspired interest in Bose-Einstein condensation. The prospect of experimentally observing Bose-Einstein condensation for the first time, in weekly interacting systems, excited the small band of physicists working in atomic physics at the time. In 1981, Phillips *et al* used resonant, counterpropagating laser beams and a spatially varying magnetic field to slow the velocities of sodium atoms in a thermal atomic beam to around 1180 m/s [32]. Building further on their success, Proden *et al* were able to slow atoms to even lower velocities of around 15 m/s in 1982 [34]. Finally, in 1984, Proden *et al* were able to produce a free sample of sodium atoms at rest, thereby deomonstrating that atoms could be stopped using laser light [33].

Having demonstrated that atoms could be stopped using laser light, the natural progression en route to the production of Bose-Einstein condensation was to be able to trap neutral atoms that had been slowed/stopped. In April 1985, Chu *et al* reported the three-dimensional viscous confinement and cooling of atoms using laser light [13]. In that same month, Migdall *et al* reported the first observation of magnetically trapped neutral atoms [29].

The basic technologies were now in place to advance on to the production of Bose-Einstein condensation. Using RF-induced evaporative cooling and the laser slowing/trapping technologies discussed above, the groups mentioned at the beginning of this section [1, 11, 15] finally achieved Bose-Einstein condensation. As discussed at length in section 1.4.2, the harmonic nature of the magnetic traps typically used in trapping atoms yield thermal distributions which are gaussian in nature, and parabolic for pure condensates. Using the relative populations of these two distributions, and a critical temperature T_c based on experimental and atomic parameters, the temperature of the system can be deduced; this technique is employed in the present study. Ketterle *et al* offer a great review on the relationship between distribution fractions and temperature in their paper of 1999 [27].

The ANU BEC & Atom Laser group employs the common technique of absorption imaging to acquire data pertaining to Bose-Einstein condensates and atom lasers. This involves exposing an atomic sample to resonant or near-resonant laser light; the light is partly absorbed by the sample, resulting in a shadow cast onto an imaging camera. The basic imaging setup used in the experiment is shown in figure 1.1.

Atoms in the sample being imaged scatter light during the imaging process, and while

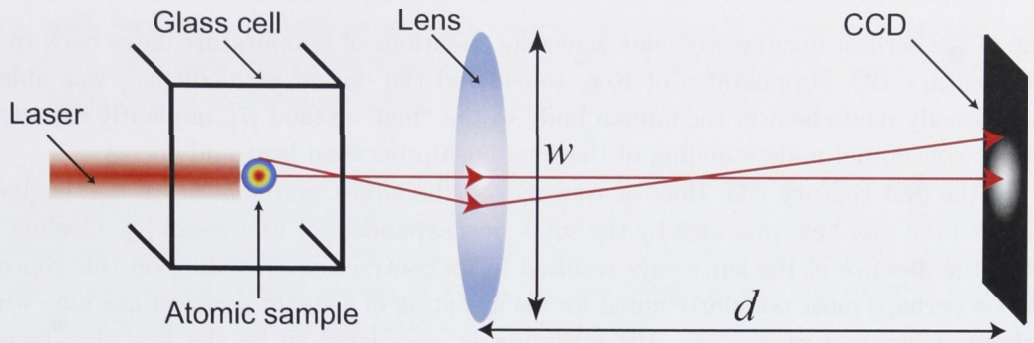

Figure 1.1: The imaging optics used in the present study (not to scale). The width w of the lens and its distance d to the CCD array determine the diffraction limit ℓ_{diff}, discussed in section 5.1.2.

the dynamics of resonant scattering in this context has been understood since the 1930s [35] (see also section 2.1.1), the impact of scattering on the quality of absorption images appears not to be discussed in the literature. It stands to reason that for a long enough exposure time, atoms in a sample being imaged will scatter enough times and acquire enough momentum such that their atomic motion will be evident in an image. For instance, an atom absorbing a resonant, 780nm photon acquires a kinetic energy of $E_{recoil} = h\nu \approx 2.9 \times 10^{-30}$ J/photon. On average, an atom will receive such a kinetic 'kick' every ~27 ns (see section 2.1.1), and given the shortest exposure used in the present study is 30 μs, at least 1,100 kicks are typically experienced by an atom on the *shortest* imaging time scale in the present study. On the largest imaging time scale used in the present study, which is 270 μs, atoms can receive as many as ~10,000 kicks, potentially resulting in random displacements on an observable length scale.

In previous experimental images taken by the group, some 'blurring' effect does appear to occur at long exposure times. But how significant is this effect, and for what exposure times does it become noticeable? And most importantly, does it change the nature of the thermal and condensate distributions, such that temperature measurements are no longer accurate after certain exposure times? The aim of the present study is to answer these questions to assess whether or not the process of absorption imaging can alter the atomic sample under study such that temperature measurements are not longer reliable.

1.2 A brief history of temperature

In the modern world, temperature is one of the most regularly measured and stated physical parameters. For at least as long as man has been acquainted with fire, if not earlier, he has understood temperature in a basic, intuitive sense. Yet despite this, developments in both the measuring and understanding of temperature occurred relatively late in history. Generally, temperature is related to the average kinetic energy of the physical system whose temperature is being measured. To understand contemporary ideas on temperature, it is important to understand the historical context within which these ideas were developed.

1.2.1 'Heat' and 'cold': man's intuitive journey towards temperature

One of the earliest documented and 'scientific' mentions of temperature dates back to the fifth century BC. Hippokrates of Kos, considered the 'father of medicine', was able to conceptually relate heat in the human body to the "fuel" of food [7], implicitly expressing a basic conceptual understanding of the relationship between heat and energy.

In the first century AD, Hero of Alexandria, the Greek mathematician and engineer, observed the way heat provided by the sun's rays expanded air in a vessel [7]. Cooling the air in the absence of the sun's rays resulted in its contraction. Building on this concept, Hero is perhaps most popularly noted for his invention of a steam-powered machine which utilised steam to turn a disk. His invention is considered to be the first documented case of a steam engine where an intuitive understanding of pressure, heat, volume, and temperature was used to harness mechanical motion.

The thermoscope, precursor to the thermometer, was first pioneered by Persian polymath Abū 'Ali al-Ḥusayn ibn 'Abd Allāh ibn Sinā (commonly known as Avicenna in the West) early in the eleventh century [30]. Unlike the thermometer, the thermoscope is a device used to observe changes in temperature rather than to observe an absolute value of temperature or change in temperature. Avicenna's thermoscope was a tube containing water which expanded when heated and contracted when cooled, showing a change of temperature in the local environment had taken place.

The thermometer itself was not invented by a single person but rather developed over time with the ideas of several scientists. Galileo created both thermoscopes and thermometers in the sixteenth century, although they did not measure temperature independent of barometric pressure (such instruments are now known as barothermoscopes)[9].

The word 'temperature' itself was coined by J. Leurechonin in 1624 in his book *La Récréation Mathématique* [6]. In it, Leurechon discusses a thermometer similar to that of Avicenna's in that he describes a thin glass tube ending in a vase full of water, remarking that:

> *...Those who wish to determine changes by numbers and degrees draw a line all along the tube and devide it into 8 degrees, according to the philosphers...*

Like the 'thermometers' built by Avicenna and Galileo, the thermometers described in Leurechon's book were also really barothermoscopes. It wasn't until around 1654 when Ferdinand de' Medici II, Grand Duke of Tuscany, created a temperature sensing device which worked independent of barometric pressure [6]. While the device created by Ferdinan II was still a thermoscope, hermetically sealing the thermometric fluid within the thermoscope meant that observed changes in temperature were isobaric, proving to be an important step toward the development the thermometer.

1.2.2 From thermoscopes to thermometers

With the thermoscope developed to an instrument capable of independently observing changes in temperature, the next logical step was to put an absolute measure and scale on temperature. While the notion of using a scale to observe changes in temperature had at least been around since Galileo, it was Dutch scientist and mathematician Christian Huygens who recognised the impending need for a universal scale and standard for the measurement of temperature [6]. In a letter dated January 2nd, 1665, Huygen's wrote:

> ...It would be well to have a universal and determinate *standard* for heat and cold, securing a definite proportion between the capacity of the bulb and the tube, and then taking for the commencement of the degree of cold at which water begins to freeze or better the temperature of boiling water...

Yet despite Huygen's foresight, it was another 29 years until, in 1694, mathematician Carlo Renaldini suggested using two fixed points in a thermometric scale and creating equal increments of measurement in-between [6]. Renaldini suggested the sensible temperatures of the freezing and boiling points of water for the fixed values, but chose a seemingly arbitrary scale of 12 increments between the two points.

Despite Renaldini's clever suggestion, his efforts appeared to have largely gone unnoticed. In 1701, Newton independently developed his own scale with two fixed points [6]. Consistent with the zero-points chosen by others before him, Newton also used the freezing point of water. However, for the 'upper' point, Newton chose the somewhat unusual and less consistent 'armpit temperature of a healthy Englishman'.

In 1706, Daniel Gabriel Fahrenheit developed a scale which utilised the melting point of ice at a value of 32 and the boiling point of water at 212 [6]. In 1742, Anders Celsius used the same points but suggested a scale which had the zero point chosen as the boiling point of water and the melting point of ice as 100 [6]. Coincident with Celsius's death in 1744, Swedish botanist Carolus Linnaeus reversed the scale to the intuitive, current form of the Celsius scale whereby the zero point is at the freezing point of water and the boiling point marked as 100, being the hundredth increment after zero [6]. Despite the wide use of the Celsius scale by the end of the eighteenth century, thermometers did not generally agree with each other when placed in thermal equilibrium. A universal, absolute thermodynamic temperature scale needed to be developed, but could not be done so before advances in thermodynamics were made.

1.3 The development of thermodynamics

1.3.1 The Ideal Gas and absolute temperature scale

Between 1662 and 1676, the observation that the product of the pressure P and volume V of a fixed mass of gas remained constant, along a given isotherm (constant temperature T), was made independently by Robert Boyle and Edme Mariotte [22]. Despite Boyle's caution that the accuracy of his observation was limited, the relationship he co-discovered nevertheless became known as the Boyle-Mariotte Law

$$(PV)_T = K_T, \tag{1.1}$$

where K_T is some constant for a given temperature.

Further, between 1787 and 1802, Jacques-Alexandre César Charles and Joseph Louis Gay-Lussac found that equal volumes of real gases expand by the same amount for an equal change in temperature, under isobaric (constant pressure) conditions. This concept, the Charles-Gay-Lussac Law, is expressed as

$$\frac{1}{V_0}\left(\frac{V - V_0}{T - T_0}\right)_P = \alpha_{0P}, \tag{1.2}$$

where α_{0P} has units of K^{-1}.

This relationship can also be expressed in the case where the volume of a gas is held constant (isochoric), such that a change in temperature results in a proportional change in pressure

$$\frac{1}{P_0}\left(\frac{P-P_0}{T-T_0}\right)_V = \alpha_{0V}. \tag{1.3}$$

The concepts of the Boyle-Mariotte and Charles-Gay-Lussac Laws were combined by Edmile Clapeyron in 1834 to give Clapeyron's equation of state of a gas [36]. Building on the idea that the volume of a gas of fixed mass is a function of both pressure and temperature, Claperyron suggested that

$$\frac{dP}{P}+\frac{dV}{V}=\frac{dT}{\left(\frac{V}{\alpha_{0P}V_0}\right)}=\frac{dT}{\left(T-T_0+\frac{1}{\alpha_{0P}}\right)}, \tag{1.4}$$

where equation 1.2 has been utilise to rewrite the denominator on the right hand side of equation 1.4. Integrating equation 1.4 yields

$$\ln P+\ln V=\ln\left(T-T_0+\frac{1}{\alpha_{0P}}\right)+\ln R_P, \tag{1.5}$$

where R_P is a constant of integration (the P subscript indicating the isobaric case). Taking the antilogarithms of equation 1.5 yields

$$PV=R_P\left(T-T_0+\frac{1}{\alpha_{0P}}\right). \tag{1.6}$$

The isochoric form of equation 1.6 is likewise expressed as

$$PV=R_V\left(T-T_0+\frac{1}{\alpha_{0V}}\right). \tag{1.7}$$

Together, equations 1.6 and 1.7 form Clapeyron's equation of state of a gas, although it is understood that they are approximations and do not reflect the behaviour of a real gas.

The terms in parentheses in these equations are respectively known as the isobaric and isochoric cubical coefficients of the expansion of a gas. In 1845, Victor Regnault found that when a gas was heated between the ice and steam points of water at atmospheric pressure, the mean of this coefficient in both the isobaric and isochoric cases was around 1/273 per Celsius degree [22]. Given his findings, Regnault was interested in developing an absolute temperature scale. However, while the mean of the expansion coefficients in the isobaric and isothermic cases was in good agreement, for any given value of pressure, the coefficient was only approximately equal to its respective volume counterpart. Further, the coefficients for different permanent gases were also only approximately equal.

To circumvent this problem, Regnault devised the *ideal gas*, a gas which perfectly satisfied both the isobaric and isochoric forms of the Boyle-Mariotte Law (equations 1.2 and 1.3). This required that $\alpha_{0P}=\alpha_{0V}=\alpha^0$ and $R_P=R_V=R$, so as to create a single Clapeyron equation of state independent of pressure and volume

$$PV=R\left(T-T_0+\frac{1}{\alpha^0}\right). \tag{1.8}$$

The term in parenthesis is therefore the temperature on the ideal gas absolute temperature

scale. The constant of integration R is defined differently here as compared to equations 1.6 and 1.7. To avoid a dependence on either pressure or volume, R is defined to be dependent on molecular weight MW such that

$$R = \frac{\mathbf{R}}{MW}, \tag{1.9}$$

where $\mathbf{R}$ is the *universal gas constant*, given by

$$\mathbf{R} = 8316 \frac{\text{J}}{\text{kg.mol.K}}. \tag{1.10}$$

Despite the relative success of Regnault's ideal gas, it ultimately proved lacking in defining an absolute temperature scale as such a reference scale could only be defined by a definite thermometric substance at a definite pressure or volume, depending on the type of gas thermometer in use [5].

Where Regnault fell short in defining an absolute temperature scale, William Thomson (Lord Kelvin) succeeded. Taking inspiration from Sadi Carnot's analysis of a reversible heat engine in 1824 [12], Kelvin realised that such an engine operating between two isotherms and two adiabats provided the basis for an absolute thermometric scale, for two reasons. Firstly, the efficiency of a Carnot engine was independent of a working substance. Secondly, it was *only* dependent on two empirical temperatures. Thomson thus suggested an arbitrary, absolute temperature function Θ, expressed in terms of the reversible Carnot heats as [39]

$$\frac{\delta Q}{Q} = \frac{d\Theta}{\Theta} = f(T)dT, \tag{1.11}$$

where Q is heat and T is empirical temperature.

Thomson defined his function Θ using the zero of the air thermometer and set $\Theta \approx T - T_0 + \frac{1}{\alpha_{0P}} \approx T - T_0 + \frac{1}{\alpha_{0V}}$. He then took the constant $\frac{1}{\alpha_{0V}}$ to be equal to 273, such that the Kelvin scale is related to the Celsius scale by

$$\Theta_C = T(^\circ C) + 273, \tag{1.12}$$

since the reference temperature T_0 was taken as 0°C. Kelvin also related his scale to the empirical scale by setting $\Theta_{steam} - \Theta_{ice} = T_{steam} - T_{ice}$, thus succeeding in completely defining the absolute thermodynamic temperature scale. Thanks to the work of Carnot, Kelvin made the theoretical advances Regnault couldn't. Yet despite Kelvin's progress, there remained one nagging issue: the *experimental* determination of absolute temperature.

Here, Kelvin could do no more than refer to the gas thermometer. In practice, this technological constraint meant compromising his theoretical ideas when measuring temperature. The gas thermometer restricted Kelvin to the approximation

$$\frac{\Theta_2}{\Theta_1} \approx \left(\frac{P_2}{P_1}\right)_V \approx \left(\frac{V_2}{V_1}\right)_P. \tag{1.13}$$

Kelvin knew that, as Clapeyron before him had discovered, the cubic coefficients of the expansion of gas were only approximately correct, the implication of which meant that in an *empirical* context, Kelvin's new theory was just re-expressing the ideal gas formula

$$PV = R\Theta. \tag{1.14}$$

The empirical realisation of an absolute temperature required yet further developments of thermodynamics.

1.3.2 Temperature and the Zeroth, First, and Second Laws of Thermodynamics

The Zeroth, First, and Second Laws of Thermodynamics are the axioms upon which modern thermodynamics is built. Interestingly enough, the Zeroth Law of Thermodynamics was developed in 1872 by James Clerk Maxwell, *after* the First and Second Laws. The Zeroth law states that:

> *Two systems brought into thermal equilibrium with a third system are in thermal equilibrium with each other.*

The implication of the Zeroth Law is that each state of thermal equilibrium between any given substance and a reference substance can be labeled, these arbitrary labels known as empirical temperatures T.

The first and second laws were developed around the same time during the 1850s, and are the results of work done by Lord Kelvin, Rudolf Clausius and William Rankine. The First Law states that any work done during an adiabatic change of state is specified by the end states of the substance. More simply, it states that 'energy is conserved'; the change in a system's total energy U is equal to the work done on the system W and the heat Q added or subtracted [37]

$$\Delta U = W + Q. \tag{1.15}$$

The Second Law of Thermodynamics states that the entropy S of a closed system (in the infinite particle limit) always increases, unless the system reaches thermal equilibrium in which case it has reached a maximum [37]. Entropy is given by

$$S \equiv k_B \ln \Omega, \tag{1.16}$$

where k_B is Boltzmann's constant and Ω is the multiplicity of the system. At thermal equilibrium, the system will be in or close to the state with the greatest multiplicity.

The development of these axioms of thermodynamics ultimately provided the grounds upon which temperatures on the absolute scale could be measured experimentally. One of the many thermodynamic identities that follows from the above axioms is the Maxwell relation

$$\left(\frac{\delta h}{\delta P}\right)_T = V - T\left(\frac{\delta V}{\delta T}\right)_P, \tag{1.17}$$

which relates the rate of change of enthalpy h with respect to pressure, volume and the rate of change of volume with respect to temperature. T is the absolute temperature of thermodynamics and the enthalpy is defined as [37]

$$h \equiv U + PV. \tag{1.18}$$

From equation 1.17, it can be shown that the product of pressure and volume PV, in the limit where pressure approaches zero, is finite [4] such that

$$(PV)^0 = RT. \tag{1.19}$$

Because of the limiting behaviour of the pressure-volume product, it can be seen that

$$\frac{T_2}{T_1} = \lim_{P \to 0} \frac{(PV)_2}{(PV)_1} = \frac{(PV)_2^0}{(PV)_1^0} = \frac{\Theta_2}{\Theta_1}. \tag{1.20}$$

Consequently, once a reference temperature along a given isotherm has been established, or a definite temperature difference between two isotherms, equation 1.20 can be used to determine all other temperatures on the absolute temperature scale.

1.4 Bose-Einstein Condensation

The development of quantum mechanics at the beginning of the twentieth century changed the way physicists understood the universe, particularly on atomic and sub-atomic scales. As a natural consequence, the way in which physicists understood thermodynamics changed, leading to some spectacular discoveries. One such discovery was that of Bose-Einstein condensation (BEC). The ability to experimentally observe a BEC not only offered further empirical validity for quantum theory but, for the first time, quantum behaviour could be observed on a macroscopic scale. As a result, the fertile ground of atom-optics has lead to an enormous amount of interest in BEC since they were observed in 1995 [1, 15, 11].

1.4.1 Statistical mechanics and the emergence of Bose-Einstein Condensation

The Ideal Gas revisited

The ideal gas discussed in section 1.3.1 can be analysed using statistical mechanics, the fundamental axiom of which is that *in thermal equilibrium, every distinct state of a system, with a total energy E, is equally probable.* The total temperature T in such a system is a measure of the total energy of the system in thermal equilibrium. In order to understand the properties of a system in the context of the above axiom, the relationship between the number of distinct states, the energy of each distinct state, the number of particles in each state, and the total number of particles in the system, needs to be understood.

Consider an ideal gas in thermal equilibrium. It is comprised of N total atoms with n possible states, each of degeneracy d_n and energy E_n. The total number of atoms in any given state of the gas can take on many values, depending on the configuration $Q(N_1, N_2, N_3, ...)$ of the atoms within the respective states of the system [37]. Conservation of atom number and energy for the system yields the constraints

$$\sum_{n=1}^{\infty} N_n = N \tag{1.21}$$

and

$$\sum_{n=1}^{\infty} E_n = E \tag{1.22}$$

The configuration of the ideal gas system which can be achieved the largest number of different ways, is the one for which $Q(N_1, N_2, N_3, ...)$ is a *maximum.* Taking into account the axiom that all states are equally likely at thermal equilibrium, when

$Q(N_1, N_2, N_3, ...)$ is a maximum, the system is in its most probable configuration. Maximising $Q(N_1, N_2, N_3, ...)$ is therefore of interest, and the method of Lagrange multipliers can be used to maximise a function $F(x_1, x_2, x_3, ...)$ subject to the constraints $f_1(x_1, x_2, x_3, ...)$, $f_2(x_1, x_2, x_3, ...)$ etc. [21] [8]. To do so, the introduction of a new function G is necessary

$$G(x_1, x_2, x_3, ..., \lambda_1, \lambda_2, \lambda_3, ...) \equiv F + \lambda_1 f_1 + \lambda_2 f_2 + ... \tag{1.23}$$

Further, the derivatives of G are set to zero

$$\frac{\delta G}{\delta x_n} = 0; \qquad \frac{\delta G}{\delta \lambda_n} = 0. \tag{1.24}$$

In the context of the ideal gas, equation 1.23 can be written

$$G \equiv \ln Q + \alpha \left[N - \sum_{n=1}^{\infty} N_n \right] + \beta \left[E - \sum_{n=1}^{\infty} N_n E_n \right], \tag{1.25}$$

where α and β are the Lagrange multipliers. Equation 1.25 can be rewritten in a more convenient form for algebraic manipulation by substituting in the functional form of $Q(N_1, N_2, N_3, ...)$ and by using Stirling's approximation. Firstly, for $Q(N_1, N_2, N_3, ...)$, if the atoms in the gas are assumed to be *distinguishable*, that is to say we can keep track of each atom and its place in any given state, the number of unique configurations of the system [21] is

$$Q(N_1, N_2, N_3, ...) = N! \prod_{n=1}^{\infty} \frac{d_n^{N_n}}{N_n!}. \tag{1.26}$$

For cases where this assumption does not hold, the different forms of the function $Q(N_1, N_2, N_3, ...)$, and the subsequent statistical implications of these different forms, are discussed later in this section.

For large numbers of atoms N_n in each state, Stirling's approximation can be used and is defined as

$$\ln z! \approx z \ln z - z \qquad for z \gg 1. \tag{1.27}$$

Consequently, using Stirling's approximation and the functional form of $Q(N_1, N_2, N_3, ...)$, equation 1.25 can be rewritten as

$$G \approx \sum_{n=1}^{\infty} [N - n \ln d_n - N - n \ln N_n + N_n - \alpha N_n - \beta E_n N_n] + \ln N! + \alpha N + \beta E. \tag{1.28}$$

Setting the derivative of G with respect to N_n to zero and solving for N_n, the most probable occupation number N_n for a given energy E_n is given by

$$N_n = d_n e^{-\alpha + \beta E_n}. \tag{1.29}$$

For the ideal gas, it can be shown [21] that the physical significance of α is related to the chemical potential μ

$$\mu(T) \equiv -\alpha k_B T. \tag{1.30}$$

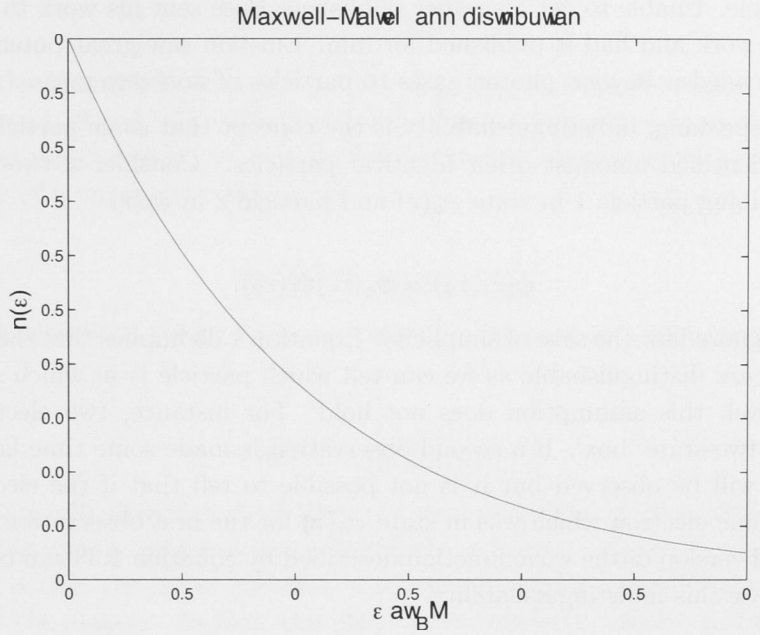

Figure 1.2: The The Maxwell-Boltzmann distribution, expressed as a function of the dimensionless ratio ϵ/k_BT.

Likewise, it can be shown that β is related to temperature T

$$\beta = \frac{1}{k_BT}. \tag{1.31}$$

Substituting equations 1.30 and 1.31 into equation 1.29 and dividing through by the degeneracy d_n, the expression for the most probable number of particles in a particular (single-particle) state with energy ϵ is derived

$$n(\epsilon) = \frac{1}{e^{(\epsilon-\mu)/k_BT}}. \tag{1.32}$$

This, of course, is the famous *Maxwell-Boltzmann* distribution, whose functional form is graphically illustrated in figure 1.2.

While the Maxwell-Boltzmann distribution is a good approximation in instances where the particles comprising the system are *distinguishable*, it fails to adequately describe systems whose constituent particles are considered *indistinguishable*.

Indistinguishability

As quantum mechanics was rapidly developing in the first half of the twentieth century, physicists began looking at statistical mechanics in light of the new theory. One such consequence of these investigations was the concept of *indistinguishability*, and one key physicist involved in the development of quantum statistical mechanics was Indian Satyendra Nath Bose.

Interested in both Plank's blackbody radiation law and Einstein's idea that light was comprised of discrete quanta of energy, Bose set out to derive Planck's law using statistical

mechanics [10]. In successfully doing so, Bose assumed the photons in his system were indistinguishable. Unable to get his paper published, Bose sent his work to Einstein who translated his work and had it published for him. Einstein saw great potential in Bose's work, and extended it beyond photon gases to particles of non-zero mass.

Generally speaking, indistinguishability is the concept that some particles can not be individually identified amongst other identical particles. Consider a two-particle wave function describing particle 1 in state $\psi_a(r)$ and particle 2 in $\psi_b(r)$

$$\psi(r_1, r_2) = \psi_a(r_1)\psi_b(r_2), \tag{1.33}$$

where spin is ignored for the sake of simplicity. Equation 1.33 implies that the two particles in the system *are* distinguishable as we can tell which particle is in which state. But on a quantum level, this assumption does not hold. For instance, two electrons may be observed in a two-state 'box'. If a second observation is made some time later, the same two electrons will be observed but it is not possible to tell that if the electron in state $\psi_a(r)$ is the *same* electron which was in state $\psi_a(r)$ for the first observation. In this case, a more general version of the wave function described by equation 1.33 can be constructed to accommodate this indistinguishability

$$\psi_{\pm}(r_1, r_2) = \frac{1}{\sqrt{2}} A \left[\psi_a(r_1)\psi_b(r_2) \pm \psi_b(r_1)\psi_a(r_2)\right]. \tag{1.34}$$

The wave function described by equation 1.34 yields two options for identical particles. In the instance where the subtraction sign is used, it describes **fermions**. Where the addition sign is used, it describes **bosons**. The impact of indistinguishability on the statistics of a system such as an ideal gas can now be analysed; indeed, a subtle yet profound departure from the Maxwell-Boltzmann statistics, described by equation 1.32, is observed. Following a similar analysis used to derive the Maxwell-Boltzmann distribution for an ideal gas (equation 1.32), an expression for the most probable number of particles in a particular energy state ϵ can be derived for both fermions and bosons.

It can be shown [21] that the number of configurations $Q(N_1, N_2, N_3, ...)$ for a system comprised of fermions is

$$Q(N_1, N_2, N_3, ...) = \prod_{n=1}^{\infty} \frac{d_n!}{N_n!(d_n - N_n)!}. \tag{1.35}$$

For bosons, the number of configurations $Q(N_1, N_2, N_3, ...)$ for such a system is

$$Q(N_1, N_2, N_3, ...) = \prod_{n=1}^{\infty} \frac{(N_n + d_n - 1)!}{N_n!(d_n - 1)!}. \tag{1.36}$$

Using the constraints described in equations 1.21 and 1.22, and also using the method of Lagrange multipliers described through equations 1.23 to 1.29, the most probable occupation number N_n for a given energy state E_n can be derived for systems comprised of both fermions and bosons. In the case of the former, the expression is given by

$$N_n = \frac{d_n}{e^{(\alpha+\beta E_n)} + 1}. \tag{1.37}$$

For bosons, for the most probable occupation number is given by

$$N_n = \frac{d_n}{e^{(\alpha+\beta E_n)} - 1}. \tag{1.38}$$

As with the Maxwell-Boltzmann case for N_n, substitutions for α and β can be made using equations 1.30 and 1.31. Dividing through by the degeneracy d_n yields an expression for the most probable number of particles in a particular (single-particle) state with energy ϵ. In the case of fermions, the expressions is

$$n_{FD}(\epsilon) = \frac{1}{e^{(\epsilon-\mu)/k_B T} + 1}. \tag{1.39}$$

Equation 1.39 describes *Fermi-Dirac* statistics. In the case of bosons, the expression for $n(\epsilon)$ is

$$n_{BE}(\epsilon) = \frac{1}{e^{(\epsilon-\mu)/k_B T} - 1}, \tag{1.40}$$

where equation 1.40 describes *Bose-Einstein* statistics. The striking difference between the Mawell-Boltzmann and Fermi-Dirac distributions, when compared to the Bose-Einstein distribution, is that the latter does not converge on a finite value for the lowest energy state ϵ_{min} of the system. In fact, the distribution tends to infinity as the temperature T tends to zero. The number of particles in every energy state ϵ above the minimum ϵ_{min} is finite and limited by the chemical potential μ; if $\mu > \epsilon$, then $n(\epsilon)$ would return negative values at low temperatures, which is unphysical. However, at zero temperature the number of particles that can occupy the minimum energy state ϵ_{min} is infinite. The Bose-Einstein distribution is compared to both the Maxwell-Boltzmann and Fermi-Dirac distributions in figure 1.3.

When a significant fraction of a system's atoms fall into the ground state, the system is said to contain a *Bose-Einstein Condensate*, or BEC. A system whose atoms are *all* in the lowest energy state may be referred as a *pure* condensate. While the phenomenon of Bose-Einstein Condensation was predicted as early as 1925 [17], it wasn't until 1995 when the first BECs were observed in the laboratory [1, 15, 11]. The ability to measure the temperature of a BEC is critical in most BEC experiments, not only as a parameter of interest in its own right, but also as a validation that condensation has occurred.

1.4.2 Measuring the temperature of a Bose-Einstein Condensate

When making a BEC in the laboratory, it is common to cool atoms in two stages; first, using a Magneto-Optical Trap (MOT), and secondly by using RF evaporation [28]. The condensate is then usually held in a magnetic trap and its temperature can then be measured. However, it is common, as in the present study, to release the BEC from the trap and to let it ballistically expand before imaging. By understanding the dynamics of a BEC in a magnetic trap and how it expands after being released from a trap, the measurement of temperature can be understood.

Cold thermal or condensed atoms are usually trapped in a magnetic potential that is harmonic in nature. Magnetic traps only work for atoms which have a ground- or meta-stable state magnetic dipole moment $\mathbf{u}$. BECs investigated in the present study are comprised of Rb^{87} atoms, which have a ground state magnetic dipole moment of $\mathbf{u} = \hbar \cdot 84.7185$ MHz. The force exerted on the atoms by the trap is

$$\mathbf{F} = -\nabla(\mathbf{u} \cdot \mathbf{B}). \tag{1.41}$$

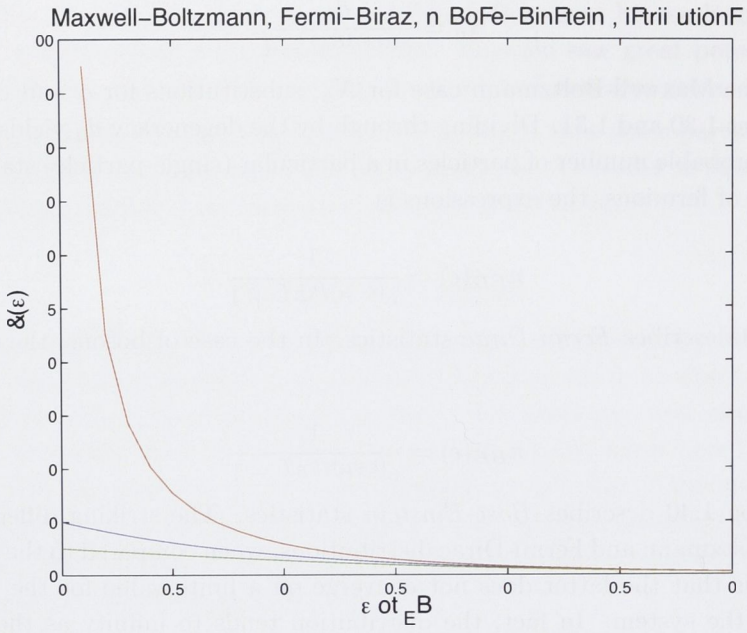

Figure 1.3: Comparing the Maxwell-Boltzmann (blue), Fermi-Dirac (green), and Bose-Einstein (red) distributions, expressed as functions of the dimensionless ratio ϵ/k_BT. Note how n(ϵ) asymptotes toward infinity as ϵ approaches zero for the Bose-Einstein distribution.

The harmonic nature of the trap's magnetic potential is a product of the geometry of the coils that comprise the trap [28], and can be expressed as

$$V(\mathbf{r}) = \frac{1}{2}m\left(\omega_1^2x^2 + \omega_2^2y^2 + \omega_3^2z^2\right), \tag{1.42}$$

where ω_1, ω_2, and ω_3 are the trap frequencies in the x, y, and z directions respectively. The corresponding energy levels permitted by the trap are given by [31]

$$\epsilon(n_1, n_2, n_3) = \left(n_1 + \frac{1}{2}\right)\hbar\omega_1 + \left(n_2 + \frac{1}{2}\right)\hbar\omega_2 + \left(n_3 + \frac{1}{2}\right)\hbar\omega_3, \tag{1.43}$$

where the n_i values are integers. For a non-interacting Bose gas in a harmonic potential given by equation 1.42, the density of states can be shown [31] to be

$$g(\epsilon) = \frac{\epsilon^2}{2\hbar^3\omega_1\omega_2\omega_3}. \tag{1.44}$$

Before arriving at an expression for the temperature of the condensate T, it is first useful to derive an expression for the critical temperature T_c. The critical temperature is the temperature at which macroscopic observation of ground state population can be observed.

The number of particles in excited states is given by

$$N_{ex} = \int_0^\infty g(\epsilon)n_{BE}(\epsilon)d\epsilon, \tag{1.45}$$

which is a maximum for $\mu = 0$. The transition temperature T_c is determined by using the condition that all atoms in the system can be found in the excited states

$$N = N_{ex}(T_c, \mu = 0) = \int_0^\infty g(\epsilon) \frac{1}{e^{\epsilon/k_B T_c} - 1} d\epsilon. \tag{1.46}$$

Writing equation 1.46 in terms of the dimensionless variable $x = \epsilon/k_B T_c$, it can be expressed as

$$N = C_\alpha (kT_c)^\alpha \int_0^\infty \frac{x^{\alpha-1}}{e^x - 1} dx = C_\alpha \Gamma(\alpha)\zeta(\alpha)(kT_c)^\alpha, \tag{1.47}$$

where C_α is a constant, $\Gamma(\alpha)$ is the gamma function, and $\zeta(\alpha) = \sum_{n=1}^\infty n^{-\alpha}$ is the Riemann zeta function. It can be shown [31] that for a harmonic oscillator, $\alpha = 3$ and $C_{\alpha=3}$ is given by

$$C_3 = \frac{1}{2\hbar^3 \omega_1 \omega_2 \omega_3}. \tag{1.48}$$

Thus we can find an expression for the critical temperature T_c by transposing equation 1.47

$$kT_c = \frac{N^{1/\alpha}}{[C_\alpha \Gamma(\alpha)\zeta(\alpha)]^{1/\alpha}} = \frac{\hbar \overline{\omega} N^{1/3}}{[\zeta(3)]^{1/3}} \approx 0.94 \cdot \hbar \overline{\omega} N^{1/3}, \tag{1.49}$$

where $\overline{\omega}$ is the geometric mean of the trapping frequencies, given by

$$\overline{\omega} = (\omega_1 \omega_2 \omega_3)^{1/3}. \tag{1.50}$$

The critical temperature is an important parameter both experimentally and theoretically. It indicates the temperature at which the occurrence of condensation can be expected based on the total number of atoms in the system N and the trap frequencies ω_i. If the total number of atoms N and condensate fraction N_0 are obtained experimentally, and the trap frequencies known, then the temperature of the condensate can be determined using the critical temperature.

Below the critical temperature, the number of particles remaining in the excited state N_{ex} is given by equation 1.47. Using this expression and that of equation 1.49, we can express N_{ex} as

$$N_{ex} = N \left(\frac{T}{T_c} \right)^\alpha. \tag{1.51}$$

Recalling that $\alpha = 3$ for a harmonic potential, we can use equation 1.51 to find an expression for the number of atoms in the condensate

$$N_0 = N \left[1 - \left(\frac{T}{T_c} \right)^3 \right], \tag{1.52}$$

where we have used the assumption that total atom number is conserved between the atoms in the excited states (the *thermal fraction*) and the condensate fraction, which is appropriate over the lifetime of the experiment.

Temperature fitting

If we can experimentally determine the parameters N_0, N, and T_c, the temperature of a BEC can be obtained using expression 1.52. Using absorption imaging (the technology of which is discussed in section 5.1), the column density distribution $n_{CD}(\mathbf{r})$ of an atomic cloud can be measured. The column density is the three-dimensional density of the atomic cloud integrated along the direction of the imaging laser, the exact form of which depends on the temperature of the system. Generally, it is expressed as

$$n_{CD}(\mathbf{r}) = \int_{-\infty}^{\infty} n(x, y, z)dx, \tag{1.53}$$

where it has been assumed the imaging laser is imaging in the x direction.

For temperatures at or above T_c, the column density is single-mode. For temperatures below T_c but above 0K, the distribution is *bi-modal*. Finally, for a condensate at 0K, the distribution is again single-mode. Example column density distributions in these three temperature regimes, as well as their respective cross sectional profiles, are illustrated in figure 1.4. Understanding the analytical form of the density distribution in these three regimes allows us to determine N_0, N, and T_c by fitting a two-dimensional curve to data obtained experimentally.

Firstly, in the purely thermal regime where $T > T_c$ and $T \gg \hbar\omega_{x,y,z}$, the density distribution can be shown [27, 20, 26, 2] to have the form

$$n_{therm}(\mathbf{r}) = \frac{1}{\lambda_{dB}^3} g_{3/2}(z(\mathbf{r})) \approx \frac{1}{\lambda_{dB}^3} z(\mathbf{r}), \tag{1.54}$$

where

$$\lambda_{dB} = \left(\frac{2\pi\hbar^2}{m k_B T}\right)^{1/2}, \tag{1.55}$$

and

$$z(\mathbf{r}) = \exp\left(\frac{\mu - V(\mathbf{r})}{k_B T}\right). \tag{1.56}$$

The Bose function $g_j(z) = \sum_i z^i / i^j$ is approximated as having a negligible effect on the gaussian form of $z(\mathbf{r})$, given by equation 1.56. This simplifies the fitting function, which fits to parts of the distribution essentially unaffected by Bose-enhancement.

At zero temperature, the resulting density distribution can be derived from the Gross-Pitaevskii equation [27, 3, 16, 14], the form of which is

$$i\hbar\frac{d\psi}{dt} = -\frac{\hbar^2}{2m}\nabla^2\psi + V(\mathbf{r})\psi + U|\psi|^2\psi. \tag{1.57}$$

The third term on the right hand side of equation 1.57 is the non-linear interaction term

$$U = \frac{4\pi\hbar^2 a}{m}, \tag{1.58}$$

which describes the effect of two-body collisions, where a is the scattering length. In the limit of strong interactions, where $nU \gg \hbar\omega_{x,y,z}$, the kinetic energy term in equation 1.57 is small compared to the potential and non-linear interaction terms, so it can be ignored.

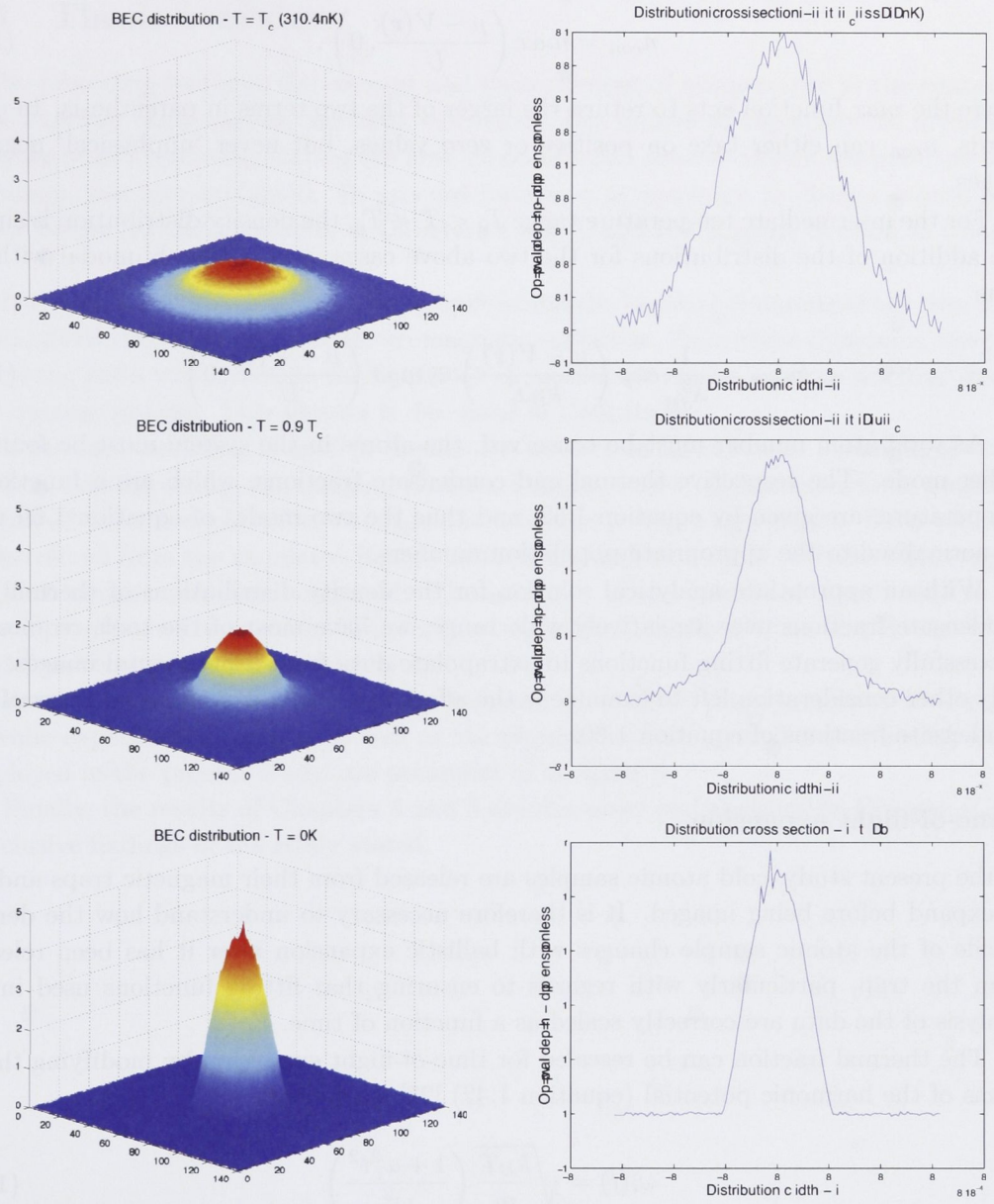

Figure 1.4: Example column density distributions in the three temperature regimes $T = T_c$, $T_c > T > 0$ K and $T = 0$ K. For $T = T_c$, the distribution is gaussian; for $T = 0$K, the distribution is parabolic, and for $T_c > T > 0$ K the distribution is bi-modal consisting of a summed gaussian and parabola, as shown in the respective distribution cross sections. These simulated, example distributions, integrated along the weak trapping axis, were simulated with harmonic trap frequencies of $2 \times \pi \times 128$ Hz in the tight trapping directions and in $2 \times \pi \times 12.8$ Hz in the weak trapping direction. The Rb^{87} atoms were set to free-fall 16.9ms before being 'imaged' using a system with a magnification of $M = 2.4$. There are $N = 1.77 \times 10^6$ atoms in the samples. These example parameters are typical of those used in the laboratory for the present study.

This is known has the *Thomas-Fermi approximation*, and given the harmonic form of $V(\mathbf{r})$, solving equation 1.57 for ψ yields an atomic density of

$$n_{con} = max\left(\frac{\mu - V(\mathbf{r})}{U}, 0\right), \tag{1.59}$$

where the *max* function acts to return the larger of the two terms in parenthesis. In other words, n_{con} can either take on positive or zero values, but never 'unphysical' negative values.

For the intermediate temperature range $T_0 < T < T_c$, the density distribution is simply the addition of the distributions for the two above cases, and is thus bi-modal with the form

$$n_{mix} = \frac{1}{\lambda_{dB}^3} exp\left(\frac{\mu - V(\mathbf{r})}{k_B T}\right) + max\left(\frac{\mu - V(\mathbf{r})}{U}, 0\right). \tag{1.60}$$

As total atom number must be conserved, the atoms in the system must be found in either mode. The respective thermal and condensate fractions, which are a function of temperature, are given by equation 1.52, and thus the two modes of equation 1.60 must be normalised to the appropriate population numbers.

With an appropriate analytical solution for the density distributions of thermal and condensate fractions over a relatively wide range, we have most of the tools required to successfully generate fitting functions to extrapolate data from experimental images. The only other consideration left to examine is the affect of ballistic expansion on thermal and condensate fractions of equation 1.60.

Time-of-flight expansion

In the present study, cold atomic samples are released from their magnetic traps and left to expand before being imaged. It is therefore necessary to understand how the density profile of the atomic sample changes with ballistic expansion after it has been released from the trap, particularly with regards to ensuring that fitting functions used in the analysis of the data are correctly scaled as a function of time.

The thermal fraction can be rescaled for time-of-flight expansion by modifying the ω_i terms of the harmonic potential (equation 1.42) [27], such that

$$\omega_i(t) = \sqrt{\frac{k_B T}{m}}\left(\frac{1 + \omega_i^2 t^2}{\omega_i^2}\right) \tag{1.61}$$

Re-scaling the condensate fraction for time-of-flight expansion is dependent on the aspect ratio ε of the condensate. It is common, as is the case in the present study, to hold BECs in a 'cigar' shapped harmonic potential, where one trapping frequency is set to a lower value than the other two such that $\omega_1 < \omega_2 = \omega_3$. The aspect ratio of the trap is $\varepsilon^{-1} = \omega_{tight}/\omega_{weak}$, where ω_{tight} are the higher trapping frequencies. It can be shown [27] that the appropriate re-scaling factors for the condensate are

$$\sqrt{1 + \tau^2} \tag{1.62}$$

for the 'tight' trapping directions, where $\tau = \omega_{tight} t$, and

$$\varepsilon^{-1}\left(1 + \varepsilon^2\left[\tau \arctan \tau - \ln\sqrt{1 + \tau}\right]\right) \tag{1.63}$$

for the weak trapping frequency direction.

1.5 Thesis overview

In the preceding sections, the concept and measurement of temperature in the context of Bose-Einstein condensation has been discussed. The motive of the study, to investigate whether or not scattering during the absorption imaging process affects temperature measurement, was also explained. To proceed further, it is necessary to discuss several more topics before presenting results in Chapters 4 and 5, and the analysis thereof, in Chapter 6.

It is essential to the present study to understand the physical dynamics of the 'two-level' atom interacting with resonant electromagnetic radiation. From these dynamics come the scattering rates which dictate the equations of motion for atoms 'random walking' during the imaging process. This physics is discussed in Chapter 2.

Numerical modeling is used to predict the statistical behaviour of a sample of atoms random walking during the imaging process. Further, based on this behaviour, simulated images of what is expected to occur in the laboratory may be produced. Data can then be extracted from the simulated images in the same fashion as it is extracted from experimental images, and then compared. The workings of the numerical model used in the present study are presented in Chapter 3, along with discussions of the limitations of the model and the tests used to validate it.

Results from the numerical model discussed in Chapter 3 are presented in Chapter 4, while experimental results, as well as the imaging technology and experimental set-up employed in the present study, are presented in Chapter 5.

Finally, the results of Chapters 4 and 5 are discussed and analysed in Chapter 5, and conclusive findings of the study stated.

Chapter 2

Atom Optics: relevant theory and imaging technology

"The whole Universe can be explained by the harmonic oscillator!"

- John Close

Chapter 2 explores the physics relevant to the absorption imaging process used to measure the temperature of Bose-Einstein Condensates in the present study. Such physics includes the two-level atom, quantum statistics pertaining to photon counting, and the statistics of atomic random walking.

2.1 Atomic Physics

2.1.1 The two-level atom

As the aim of the present study is to determine whether or not atomic motion during the absorption imaging process affects temperature measurements of BECs, it is evident that the physical dynamics of interest derive from the interaction between atoms and light. The advantage of using alkalis in the production of BECs is that they all have one valance electron. If driven by laser light of the appropriate wavelength and polarisation, this valence electron gives rise to the atom exhibiting 'two-level' behaviour [35], whereby the atom exists in one of either two states (see figure 2.1). For Rb^{87}, one such transition, when driven by σ^+ light, is the $F = 2, m_f = 2 \rightarrow F' = 3, m_f = 3$ transition. Light used in the absorption imaging process in the present study is resonant with this transition. Further, all the physical dynamics of resonant light interacting with the above Rb^{87} transition, and how this affects the motion of an atom exposed to imaging light, can be understood using a semi-classical approach to modeling the system. Inter-atomic scattering is not considered here as the atomic densities under study are sufficiently low and consequently is negligible.

In the semi-calssical approach, the atom is treated as having two discrete eigenstates

$$\Psi(\mathbf{r}, t) = c_g(t)\phi_g(t)e^{-i\omega_a t} + c_e(t)\phi_e(t)e^{i\omega_a t}, \tag{2.1}$$

where $\omega_a \equiv \omega_{eg}$. The driving electromagnetic field is treated classically, and can be written as

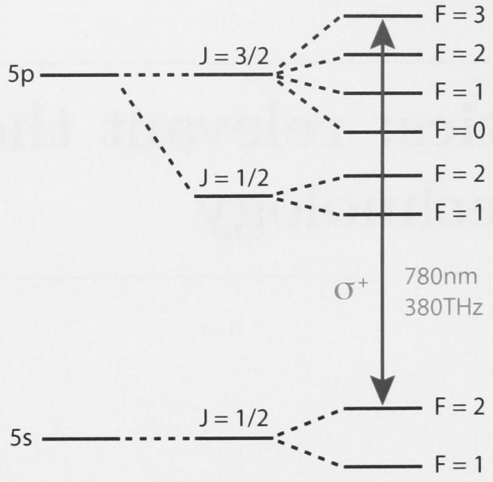

Figure 2.1: The electronic structure of Rb^{87} relevant to the present study. The $F = 2, m_f = 2 \rightarrow F' = 3, m_f = 3$ transition of interest is shown.

$$\mathcal{E}(\mathbf{r}, t) = E_0 \hat{\varepsilon} \cos(kz - \omega_l t). \tag{2.2}$$

The dipole approximation is used here; any components of the electric field that have a wavelength long compared to the wavelength of the atom are considered constant.

The density matrix for the two-level atom can be written as follows

$$\rho = \begin{pmatrix} \rho_{ee} & \rho_{eg} \\ \rho_{ge} & \rho_{gg} \end{pmatrix} = \begin{pmatrix} c_e c_e^* & c_e c_g^* \\ c_g c_e^* & c_g c_g^* \end{pmatrix}. \tag{2.3}$$

It can be shown [28] that the elements of the density matrix have the following time derivatives:

$$\frac{d\rho_{gg}}{dt} = +\gamma \rho_{ee} + \frac{i}{2}\left(\Omega^* \tilde{\rho}_{eg} - \Omega \tilde{\rho}_{ge}\right) \tag{2.4}$$

$$\frac{d\rho_{ee}}{dt} = -\gamma \rho_{ee} + \frac{i}{2}\left(\Omega \tilde{\rho}_{ge} - \Omega^* \tilde{\rho}_{eg}\right) \tag{2.5}$$

$$\frac{d\tilde{\rho}_{ge}}{dt} = -\left(\frac{\gamma}{2} + i\delta\right)\tilde{\rho}_{ge} + \frac{i}{2}\Omega^*\left(\rho_{ee} - \rho_{gg}\right) \tag{2.6}$$

$$\frac{d\tilde{\rho}_{eg}}{dt} = -\left(\frac{\gamma}{2} - i\delta\right)\tilde{\rho}_{ge} + \frac{i}{2}\Omega\left(\rho_{gg} - \rho_{ee}\right) \tag{2.7}$$

where δ is laser detuning. The decay rate of the excited state population γ is given [28, 38] by

$$\gamma = \frac{1}{t_\gamma} = \frac{\omega^3 \mu^2}{3\pi\epsilon_0 \hbar c^3}, \tag{2.8}$$

where μ is the dipole moment. The Rabi frequency Ω is given by

$$\Omega \equiv \frac{-eE_0}{\hbar}\langle e|r|g\rangle. \tag{2.9}$$

Equations 2.4 to 2.7 are known as the Optical Bloch equations. The first term on the right hand side of all of these equations pertains to spontaneous emission, while the second term pertains to the electromagnetic field driving transitions between the ground and excited states at a frequency Ω.

Scattering rates and times are of primary interest in the present study as they are required to derive the analytical expressions for the random walk process discussed in section 2.1.3. These analytics are important for the development of the numerical model discussed in Chapter 3, which is used for the theoretical predictions of how random walking affects broadening of density distribution images, and hence possibly temperature measurements as well.

Scattering rates are related to cross-sections, and for a two-level atom it can be shown [19] that the absorption cross section σ is given by

$$\sigma = \frac{\sigma_0}{1 + \frac{I}{I_{sat}} + \left(\frac{2\delta}{\gamma}\right)^2} = \frac{\hbar\omega}{I}\Lambda, \tag{2.10}$$

where I is intensity, I_{sat} is saturation intensity, δ is detuning, γ is given by equation 2.8, σ_0 is

$$\sigma_0 = \frac{3\lambda^2}{2\pi}, \tag{2.11}$$

and Λ is the scattering rate given by

$$\Lambda = \frac{1}{t_\Lambda} = \frac{1}{t_\gamma + t_\alpha}. \tag{2.12}$$

In equation 2.12, t_γ is the average time the atom spends in the excited state, given by equation 2.8, and t_α is the average time the atom spends in the ground state, which can be found by algebraic manipulation of equation 2.10 as follows:

$$\frac{\hbar\omega}{I}\Lambda = \frac{\hbar\omega}{I}\frac{1}{t_\alpha + t_\gamma} = \frac{\sigma_0}{1 + \frac{I}{I_{sat}} + \left(\frac{2\delta}{\gamma}\right)^2}. \tag{2.13}$$

So,

$$t_\alpha = \frac{\hbar\omega}{I}\frac{1}{\sigma_0}\left(1 + \frac{I}{I_{sat}} + \left(\frac{2\delta}{\gamma}\right)^2\right) - t_\gamma. \tag{2.14}$$

The above scattering rates and times are instrumental to the analytical discussion in section 2.1.3.

2.1.2 Quantum statistics

While the semi-classical approach to understanding the two-level atom is both appropriate and intuitive, quantifying the nature of noise inherent to the imaging light field must be done quantum mechanically, as photon scattering, and subsequent counting, are inherently quantum processes. It is therefore necessary to describe the imaging light as a quantised, coherent state [40]. This can be done in the Fock state basis

$$|\alpha\rangle = e^{\frac{-|\alpha|^2}{2}} \sum \frac{\alpha^n}{(n!)^{\frac{1}{2}}} |n\rangle, \tag{2.15}$$

where n is an integer and $|n\rangle$ a Fock state. The probability distribution of photons in a coherent state is given by

$$P(n) = |\langle n|\alpha\rangle|^2 = \frac{|\alpha|^{2n} e^{-|\alpha|^2}}{n!}, \tag{2.16}$$

and is thus a Poisson distribution. Using creation and annihilation operators, the average number of photons is given by

$$N = \langle \hat{a}^\dagger \hat{a} \rangle_\alpha = \alpha^\star \alpha = |\alpha|^2. \tag{2.17}$$

The variance in the average number of photons given by 2.17 is therefore

$$\Delta N = Var(\hat{a}^\dagger \hat{a}) = \langle (\hat{a}^\dagger \hat{a})^2 \rangle - \langle \hat{a}^\dagger \hat{a} \rangle^2. \tag{2.18}$$

It can thus be seen from 2.17 and 2.18 that the variance of the coherent state is

$$\Delta\alpha = \sqrt{N}, \tag{2.19}$$

as suggested by the fact that equation 2.16 is Poissonian. In the laboratory, $\sqrt{N}$ represents the noise of a signal N, where N is the number of photons counted by a photon counting device. The signal-to-noise ratio SNR of Poissonian process is therefore given by

$$SNR = \frac{N}{\sqrt{N}}. \tag{2.20}$$

While the noise of a signal measured in the lab increases with the signal as $\sqrt{N}$, the noise relative to the signal is increasingly less significant. The signal-to-noise ratio of equation 2.20 is a measure of signal resolution, and in that respect the resolution increases with N, despite the $\sqrt{N}$ noise associated with it. In the context of counting photons with a CCD camera in the present study, the larger the number of photons detected on any given pixel, the 'better' the quality of information stored in that pixel. The technological aspects of this are discussed at length in section 5.1.3.

2.1.3 Scattering-induced random walking of atoms

During the absorption imaging process, atoms in the sample being imaged scatter many photons, acquiring a net momentum kick for each scattering event. As a result of acquiring many momentum kicks, the atoms undertake a 'random walk' in coordinate space. In this section, the statistics of this random walk are analysed. Of principle interest is the variance of the final positions of the atoms, in all three dimensions of coordinate space, after their random walks have been completed. These variances can then be used to validate the random walk statistics of the numerical model, discussed in Chapter 3, used for the theoretical results presented in the present study (see Chapter 5).

To ultimately arrive at an expression for the variance of the final positions of m random-walked atoms, several aspects of the scattering process must first be understood. As the scattering rate is stochastic in nature, there will be an associated variance V_n in the number of scattering events n that occur for an exposure time t_{exp} during the imaging process. With the variance V_n known, it is then possible to derive equations of motion for the

randomly walking atoms using Wiener functions. From these equations, expressions for the variances V_x, V_y and V_z in coordinate space can then also be derived.

The variance V_n will be related to the duration of time an atom spends in both the ground and excited states. An atom being imaged acquires a $\hbar\mathbf{k}$ momentum kick in the beam direction. At some time t_γ later, the atom decays and emits a photon, acquiring a $\hbar\mathbf{k}$ momentum kick in a direction which is approximated as being uniformly random over a sphere. One absorption and one emission event constitute *one* scattering event. If t_γ and t_α are the times an atom spends in the excited and ground states of the atom respectively, then the total time of a scattering event is

$$t_\Lambda = t_\gamma + t_\alpha. \tag{2.21}$$

Consequently, scattering occurs at a rate $1/t_\Lambda$, given by equation 2.12, while the rate of emission γ is given by equation 2.8. The rate of absorption is

$$\alpha = \frac{1}{t_\alpha} = \left[\frac{\hbar\omega}{I}\frac{1}{\sigma_0}\left(1 + \frac{I}{I_{sat}} + \left(\frac{2\delta}{\gamma}\right)^2\right) - t_\gamma\right]^{-1}. \tag{2.22}$$

The resonant, Rb^{87} transition of interest has a mean lifetime $t_\gamma = 26.24$ ns (see equation 2.8). At saturation, the atom spends a similar amount of time in the ground state, as per equation 2.22 above. Each atom in the condensate therefore undergoes many scattering events during the imaging process, as the smallest exposure times are on the order of 10^{-5} s.

While the number of absorption and emission events in a given time t_{exp} are Poissonian in nature for *each* process, a single scattering event contains *both* of these processes. Thus, as demonstrated below, scattering events do not adhere to Poissonian stastistics. In fact, the variance of one scattering event is *less* than the sum of the variances of an absorption and emission event.

The Poisson distribution of emission event times, that is, the distribution of possible times the atom spends in the excited state, is given by

$$P_\gamma(t_\gamma) = \gamma e^{-\gamma t_\gamma}. \tag{2.23}$$

Similarly, the Poisson distribution of absorption events, that is, the distribution of possible times the atom spends in the ground state, is given by

$$P_\alpha(t_\alpha) = \alpha e^{-\alpha t_\alpha}. \tag{2.24}$$

Considering the above probability distributions and the excited and ground state times t_γ and t_α respectively, the average time $\overline{t_\Lambda}$ of a scattering event may be calculated

$$\begin{aligned}
\overline{t_\Lambda} &= \int_0^\infty \int_0^\infty P_\gamma(t_\gamma) P_\alpha(t_\alpha)(t_\gamma + t_\alpha)\, dt_\gamma\, dt_\alpha \\
&= \int_0^\infty P_\gamma(t_\gamma) t_\gamma dt_\gamma \int_0^\infty P_\alpha(t_\alpha) dt_\alpha \\
&+ \int_0^\infty P_\gamma(t_\gamma) dt_\gamma \int_0^\infty P_\alpha(t_\alpha) t_\alpha dt_\alpha \\
&= \frac{1}{\gamma} + \frac{1}{\alpha}.
\end{aligned} \tag{2.25}$$

Similarly, the variance in time can be calculated, and is

$$\begin{aligned} V_{t_\Lambda} &= \int_0^\infty \int_0^\infty P_\gamma(t_\gamma) P_\alpha(t_\alpha)(t_\gamma^2 + t_\alpha^2)\, dt_\gamma\, dt_\alpha \\ &= \frac{1}{\gamma^2} + \frac{1}{\alpha^2}. \end{aligned} \tag{2.26}$$

For n events, equation 2.26 is simply

$$nV_{t_\Lambda} = n\left(\frac{1}{\gamma^2} + \frac{1}{\alpha^2}\right). \tag{2.27}$$

The above expression gives the variance in *time* for n events. However, an expression for the variance V_n in the number of events occurring within a fixed time t_{exp} is required, with n the mean number of events. It can be seen that

$$\begin{aligned} \frac{\Delta t}{t} &= \frac{\Delta n}{n} \\ &\Rightarrow \frac{\Delta t^2}{t^2} = \frac{\Delta n^2}{n^2} \\ &\Rightarrow \frac{V_t}{\bar{t}^2} = \frac{V_n}{\bar{n}^2}, \end{aligned} \tag{2.28}$$

where V_t is the variance in time t. So, from equation 2.28, the variance of n can be derived:

$$\begin{aligned} V_n &= \bar{n}^2 \frac{V_t}{t^2} \\ &= \left(\frac{t}{\bar{t}}\right)^2 \frac{V_t}{t^2} \\ &= \frac{V_t}{\bar{t}^2} \\ &= \bar{n} \frac{\left(\frac{1}{\gamma^2} + \frac{1}{\alpha^2}\right)}{\left(\frac{1}{\gamma} + \frac{1}{\alpha}\right)^2}. \end{aligned} \tag{2.29}$$

Equation 2.29 describes the variance V_n of the number of scattering events n in an exposure time t_{exp}. It is now possible to develop an expression for the variances V_x, V_y, and V_z of m particles which have randomly walked in coordinate space.

The random walk described above consists of scattering processes which are discrete in time. If enough of these processes happen over a period of time which is large compared to the scattering time t_λ, then the process can be approximated as being continual using Wiener functions. This has the advantage of making analysis easier. Before the Wiener functions are used, the means and variances of a sampled process must be known.

The mean of the sum of the of n random variables X_j, weighted by the probability distribution $P_{\bar{n}}(n)$, is given by

$$\begin{aligned}\langle\sum_{j=1}^{n} X_j\rangle &= \mathbb{E}\left[\sum_{n=0}^{\infty} P_{\overline{n}}(n)\sum_{j=1}^{n} X_j\right] \\ &= \sum_{n=0}^{\infty} P_{\overline{n}}(n) n\overline{X} \\ &= \overline{n}\overline{X}, \end{aligned} \tag{2.30}$$

where $\mathbb{E}$ is used to denote the expectation value. Equation 2.30 is true whether $P_{\overline{n}}(n)$ is Poissonian or otherwise. The variance of this sum is given by

$$\begin{aligned} V(\sum_{j=1}^{n} X_j) &= \mathbb{E}\left[\sum_{n=0}^{\infty} P_{\overline{n}}(n)\left(\sum_{j=1}^{n} X_j - \overline{n}\overline{X}\right)^2\right] \\ &= \sum_{n=0}^{\infty} P_{\overline{n}}(n)\mathbb{E}\left[\left(\sum_{j=1}^{n} X_j\right)^2 + \overline{n}^2\overline{X}^2 - 2\overline{n}\overline{X}\sum_{j=1}^{n} X_j\right]. \end{aligned} \tag{2.31}$$

The term in parenthesis within the brackets can be expanded using the Central Limit Theorem, such that

$$\begin{aligned} V(\sum_{j=1}^{n} X_j) &= \sum_{n=0}^{\infty} P_{\overline{n}}(n)\left(nV_x + n^2\overline{X}^2 - \overline{n}^2\overline{X}^2 - 2\overline{n}n\overline{X}^2\right) \\ &= \overline{n}V_x + \overline{X}^2\left(V_n + \overline{n}^2\right) + \overline{n}^2\overline{X}^2 - 2\overline{n}^2\overline{X}^2 \\ &= \overline{n}V_x + \overline{X}^2 V_n \end{aligned} \tag{2.32}$$

Equation 2.32 represents a general expression for the variance $V(\sum_{j=1}^{n} X_j)$. For a Poissonian process specifically, it can be expressed as

$$V(\sum_{j=1}^{n} X_j) = \overline{n}V_x + \overline{n}\overline{X}^2. \tag{2.33}$$

The variance V_i^1 of a single-kick process in a random direction must now be calculated in order to set up the equations of motion. The variance of the final positions of m random-walked atoms can then be found.

The variance V_x^1 of a single-kick process in the x direction is given by

$$\begin{aligned} V_x^1 &= \int_0^{\pi}\int_0^{2\pi} \frac{\sin\theta}{4\pi}\left[k_L\cos\phi\sin\theta\right]^2 d\theta d\phi \\ &= \frac{k_L^2}{3}, \end{aligned} \tag{2.34}$$

where k_L is the wave number associated with an imaging laser photon. Similarly, the

variance V_y^1 of a single-kick process in the y direction is given by

$$\begin{aligned} V_y^1 &= \int_0^{\pi}\int_0^{2\pi} \frac{\sin\theta}{4\pi} \left[k_L \sin\phi \sin\theta\right]^2 d\theta d\phi \\ &= \frac{k_L^2}{3}. \end{aligned} \tag{2.35}$$

Finally, the variance V_z^1 of a single-kick process in the z direction is given by

$$\begin{aligned} V_z^1 &= \int_0^{\pi}\int_0^{2\pi} \frac{\sin\theta}{4\pi} k_L^2 \cos^2\theta d\theta d\phi \\ &= \frac{k_L^2}{3}. \end{aligned} \tag{2.36}$$

Equations 2.34 - 2.36 can be more conveniently expressed in the compact form

$$V_i^1 = k_L^2 \left\{\frac{1}{3}, \frac{1}{3}, \frac{1}{3}\right\}. \tag{2.37}$$

The equivalent expression for the mean of a single-kick process in the beam direction is

$$\overline{x} = k_L^2 \left\{1, 0, 0\right\}, \tag{2.38}$$

as the beam is always operating in one direction.

An expression for the mean number of kicks in a time t_{exp} can be sought by combining equation 2.30 with 2.38, such that

$$\overline{n}\overline{X} = \Lambda t_{exp} k_L^2 \left\{1, 0, 0\right\}. \tag{2.39}$$

Likewise, by combining equations 2.32 and 2.37, the variance of the number of kicks in a time t_{exp} is given by

$$\begin{aligned} \overline{n}V_x + \overline{n}\overline{X}^2 &= \Lambda t_{exp} k_L^2 \left\{\frac{1}{3}, \frac{1}{3}, \frac{1}{3}\right\} + \Lambda t_{exp} \left(\frac{\frac{1}{\gamma^2} + \frac{1}{\alpha^2}}{\left(\frac{1}{\gamma} + \frac{1}{\alpha}\right)^2}\right) \left\{1, 0, 0\right\} \\ &= \Lambda t_{exp} k_L^2 \left\{\frac{\frac{1}{\gamma^2} + \frac{1}{\alpha^2}}{\left(\frac{1}{\gamma} + \frac{1}{\alpha}\right)^2} + \frac{1}{3}, \frac{1}{3}, \frac{1}{3}\right\}. \end{aligned} \tag{2.40}$$

Equations of motion can now be set up and the variances of m atoms random walking in coordinate space, for walks of a fixed time t_{exp}, can be derived. Wiener functions will be used in the equations of motion to approximate the random walk in discrete time space as continuous in time. This is an appropriate approximation so long as there are many scattering events in time t_{exp}, and that $t_{exp} \gg t_\Lambda$, which is always the case in practice for the present study. Before the Wiener functions are employed in the equations of motion, it is useful to state the following Wiener function properties:

$$\mathbb{E}\left[dW(t)\right] = 0, \tag{2.41}$$

$$\mathbb{E}\left[dW(t)^2\right] = dt, \tag{2.42}$$

and

$$\mathbb{E}\left[dW(t_1)dW(t_2)\right] = \delta(t_1 - t_2)dt_1 dt_2, \tag{2.43}$$

where $\delta(t_1 - t_2)$ is the Dirac delta function.

The equation of motion for m atoms random walking in coordinate space can be stated as follows

$$d\mathbf{v}(t) = \Lambda\frac{\hbar k}{m}dt\hat{\mathbf{i}} + \sqrt{\Lambda\frac{\hbar^2 k_L^2}{m^2}}\left\{\left[\frac{\frac{1}{\gamma^2}+\frac{1}{\alpha^2}}{\left(\frac{1}{\gamma}+\frac{1}{\alpha}\right)^2}+\frac{1}{3}\right]^{\frac{1}{2}} dW_x, \frac{dW_y}{\sqrt{3}}, \frac{dW_z}{\sqrt{3}}\right\}. \tag{2.44}$$

Equation 2.44 exhibits the right average and variance for the velocity kicks, and can be integrated to find:

$$\mathbf{v}(t) = \mathbf{v}(0) + \Lambda\frac{\hbar k}{m}t\hat{\mathbf{i}} + \sqrt{\Lambda\frac{\hbar^2 k_L^2}{m^2}}\int_0^t\left\{\left[\frac{\frac{1}{\gamma^2}+\frac{1}{\alpha^2}}{\left(\frac{1}{\gamma}+\frac{1}{\alpha}\right)^2}+\frac{1}{3}\right]^{\frac{1}{2}} dW_x, \frac{dW_y}{\sqrt{3}}, \frac{dW_z}{\sqrt{3}}\right\}. \tag{2.45}$$

Integrating equation 2.45 thus yields an expression for position in coordinate space as a function of time:

$$\begin{aligned}\mathbf{x}(t) &= \mathbf{x}(0) + \mathbf{v}(0)t + \Lambda\frac{\hbar k}{2m}t^2\hat{\mathbf{i}} \\ &+ \sqrt{\Lambda\frac{\hbar^2 k_L^2}{m^2}}\int_0^t du\int_0^u\left\{\left[\frac{\frac{1}{\gamma^2}+\frac{1}{\alpha^2}}{\left(\frac{1}{\gamma}+\frac{1}{\alpha}\right)^2}+\frac{1}{3}\right]^{\frac{1}{2}} dW_x, \frac{dW_y}{\sqrt{3}}, \frac{dW_z}{\sqrt{3}}\right\},\end{aligned} \tag{2.46}$$

where u is a dummy variable in time. The expectation values of position and velocity, as well as the expectation values of the variance in position and velocity, can now be calculated using the Wiener function relations of equations 2.41 to 2.43. The expectation value of the velocity $\mathbf{v}(t)$ of an ensemble of m atoms is given by

$$\mathbb{E}\left[\mathbf{v}(t)\right] = \mathbf{v}(0) + \frac{\Lambda\hbar k_L}{m}t^2\hat{\mathbf{i}}. \tag{2.47}$$

The associated expectation value of the variance in velocity $\mathbf{v}(t)$ of an ensemble of m atoms is given by

$$\begin{aligned}
\mathbb{E}\left[(\mathbf{v}_j(t)-\overline{\mathbf{v}}_j(t))^2\right] &= \mathbb{E}\left[\Lambda\frac{\hbar^2k_L^2}{m}\int_0^t dW_u\int_0^t dW_v\left\{\frac{\frac{1}{\gamma^2}+\frac{1}{\alpha^2}}{\left(\frac{1}{\gamma}+\frac{1}{\alpha}\right)^2}+\frac{1}{3},\frac{1}{3},\frac{1}{3}\right\}_j\right] \\
&= \mathbb{E}\left[\Lambda\frac{\hbar^2k_L^2}{m}\int_0^t du\int_0^t dv\delta(u-v)\left\{\frac{\frac{1}{\gamma^2}+\frac{1}{\alpha^2}}{\left(\frac{1}{\gamma}+\frac{1}{\alpha}\right)^2}+\frac{1}{3},\frac{1}{3},\frac{1}{3}\right\}_j\right] \\
&= \Lambda\frac{\hbar^2k_L^2}{m}t\left\{\frac{\frac{1}{\gamma^2}+\frac{1}{\alpha^2}}{\left(\frac{1}{\gamma}+\frac{1}{\alpha}\right)^2}+\frac{1}{3},\frac{1}{3},\frac{1}{3}\right\}_j . \qquad (2.48)
\end{aligned}$$

The expectation value of the position $\mathbf{x}(t)$ of an ensemble of m atoms is given by

$$\mathbb{E}\left[\mathbf{x}(t)\right]=\mathbf{x}(0)+\mathbf{v}(0)t+\frac{\Lambda\hbar k_L}{2m}t^2\hat{\mathbf{i}}. \qquad (2.49)$$

The associated expectation value of the variance in position $\mathbf{x}(t)$ of an ensemble of m atoms is given by

$$\begin{aligned}
\mathbb{E}\left[(\mathbf{x}_j(t)-\overline{\mathbf{x}}_j(t))^2\right] &= \Lambda\frac{\hbar^2k_L^2}{m^2}\left\{\frac{\frac{1}{\gamma^2}+\frac{1}{\alpha^2}}{\left(\frac{1}{\gamma}+\frac{1}{\alpha}\right)^2}+\frac{1}{3},\frac{1}{3},\frac{1}{3}\right\}_j\int_0^t du_1\int_0^t du_2\mathbb{E}\left[\int_0^{u_1}dW_{s_1}\int_0^{u_2}dW_{s_2}\right] \\
&= \Lambda\frac{\hbar^2k_L^2}{m^2}\left\{\frac{\frac{1}{\gamma^2}+\frac{1}{\alpha^2}}{\left(\frac{1}{\gamma}+\frac{1}{\alpha}\right)^2}+\frac{1}{3},\frac{1}{3},\frac{1}{3}\right\}_j\int_0^t du_1\int_0^t du_2\int_0^{u_1}ds_1\int_0^{u_2}ds_2\delta(s_1-s_2) \\
&= \Lambda\frac{\hbar^2k_L^2}{m^2}\left\{\frac{\frac{1}{\gamma^2}+\frac{1}{\alpha^2}}{\left(\frac{1}{\gamma}+\frac{1}{\alpha}\right)^2}+\frac{1}{3},\frac{1}{3},\frac{1}{3}\right\}_j\int_0^t du_1\int_0^t du_2\min(u_1,u_2) \\
&= \Lambda\frac{\hbar^2k_L^2}{m^2}\left\{\frac{\frac{1}{\gamma^2}+\frac{1}{\alpha^2}}{\left(\frac{1}{\gamma}+\frac{1}{\alpha}\right)^2}+\frac{1}{3},\frac{1}{3},\frac{1}{3}\right\}_j\left(\int_0^t du_1\int_0^{u_1}du_2u_2+\int_0^t du_1\int_{u_1}^t du_2u_1\right) \\
&= \frac{\Lambda}{3}\frac{\hbar^2k_L^2}{m^2}t^3\left\{\frac{\frac{1}{\gamma^2}+\frac{1}{\alpha^2}}{\left(\frac{1}{\gamma}+\frac{1}{\alpha}\right)^2}+\frac{1}{3},\frac{1}{3},\frac{1}{3}\right\}_j . \qquad (2.50)
\end{aligned}$$

The three terms above in equation 2.50 give the variance of atomic motion in each of the three spatial dimensions. As one would intuitively expect, the variance is dependent on scattering rates, the momentum of scattered photons and the time over which scattering takes place. The dependence of variance on all these parameters is reflected in the common factors before the bracketed terms. It can be seen from the first of the bracketed terms that the variance in the direction of the imaging beam is different to directions orthogonal to the beam. Recall that an atom being imaged absorbs an imaging laser photon and gains a momentum kick in the direction of the laser. Because there is a variance in the

time an atom 'waits' in between absorbing photons, there is an additional spatial variance in the direction of the beam.

The statistical analysis undertaken above forms a basis upon which validation of the numerical model used in the present study, discussed in Chapter 3, can be done to ensure the model is functioning appropriately.

Chapter 3

Numerical modeling

"I think there is a world market for maybe five computers."

- Thomas Watson, IBM 1943

Numerical modeling is used in the present study to theoretically predict the imaging regime within which atomic motion, due to scattering, affects temperature measurements in absorption imaging. Chapter 3 explores the features of this model, its limitations, and also validations used to ensure the model is behaving as it is designed to.

3.1 Features of the numerical model

3.1.1 Generating random walk statistics

In section 2.1.3, the underlying physical processes that lead to atoms random walking when exposed to laser radiation, were explained. The random walk statistics of interest are the standard deviations of n 'particles' that have random walked for an exposure time t_{exp}. These standard deviations are needed to gauge how much the random walk effect 'blurs' a BEC density distribution during the imaging process. The first step in creating the model used for the theoretical aspect of the present study was to replicate the random walk process numerically.

As discussed in section 2.1.3, one scattering event consists of absorbing a photon in the beam direction, taken to be in the x direction in the present study unless otherwise stated, followed by a random scattering event in any direction with equal probability. The model is designed to be able to replicate as many randomly distributed scattering events as would occur in a given exposure time. This can be done for as many particles as desired, although as it will be shown below, there is a minimum value which yields sufficiently accurate statistics; additional particles add to simulation time without contributing significantly to statistical accuracy.

To replicate the random walk of an atom, the model steps a particle one unit of $\hbar\mathbf{k}$ in the x direction of momentum space. As this step is always in the beam direction x, it is simply a matter of adding a unit of $\hbar\mathbf{k}$ in the x direction of momentum space for every scattering event.

For the emission part of the scattering process, a momentum kick of $\hbar\mathbf{k}$ needs to be added in a random direction. The software package *Matlab*, which is used for the numerical modelling in the present study, has an inbuilt function capable of producing random numbers uniformly distributed on the unit interval [0, 1]. Thus it is necessary to

create two random variables, which could use such random numbers, to produce a random direction in three-dimensional momentum space. Only two are required as the magnitude of the kick is always a constant unit of $\hbar k$.

Using spherical polar coordinates, these two random variables are the azimuthal angle ϕ and the polar angle θ. If R_1 is a random number uniformly distributed on the unit interval [0, 1], and ϕ is an angle between 0 and 2π, then we can chose a random value for ϕ using the algorithm

$$\phi = 2\pi R_1. \tag{3.1}$$

Generating a random value for θ is not so straight forward. The angle θ needs to be some value between 0 and π. If an algorithm such as $\theta = \pi R_2$ is used, similar to that of equation 3.1, then bunching will occur about the poles of a unit sphere over which the random direction is chosen (see Figure 3.1 in section 3.2). In other words, the distribution will not be uniform and momentum kicks in the direction of the poles will be more likely. To circumvent this problem, the distribution of randomly chosen values of θ needs to be weighted to favour the equatorial directions on the sphere to counter the polar bunching effect.

Geometric considerations suggest the appropriate weighting function is sinusoidal in nature. Thus the probability density distribution function for θ, as produced by a random variable X, is

$$Pr(X) = sin(\theta), \qquad \theta \in [0, \pi]. \tag{3.2}$$

The corresponding Cumulative Distribution Function (CDF) is

$$CDF(X) = \frac{1}{2}\int_0^X \sin\theta d\theta = \frac{1 - \cos X}{2}, \tag{3.3}$$

which appropriately equals unity for $X = \pi$. From equation 3.3, it is easily seen that $\cos\theta = 1 - 2r$, the inverse of which is

$$\theta = \arccos 1 - 2X. \tag{3.4}$$

Equation 3.4 represents the correct algorithm used for generating random values of θ, which is verified in section 3.2.

To obtain the standard deviation of a sample of n particles in each of the three dimensions of coordinate space, the random walk in momentum space needs to be transformed into coordinate space. A step in coordinate space is calculated using the following transformation:

$$\mathbf{r} = \mathbf{p}\frac{t_{\alpha/\beta}}{m}, \tag{3.5}$$

where $t_{\alpha/\beta}$ is the amount of time an atom spends in either the ground or excited state (see section 2.1.3) and m is the mass of a Rb^{87} atom. The model code has been written such that the final position coordinates for all the m particles are stored. Using the *Matlab* standard deviation function *std*, the standard deviation of the particles is calculated.

The statistical accuracy of the standard deviation improves as the sample number of particles n increases. However, simulation running times also increase. Beyond a certain sample size n, the improved statistical accuracy of the standard deviation becomes

n	Mean std - n	Error - $+/-n$	Error - %	Avg. simulation time - s
300	2.1708×10^{-6}	1.92×10^{-7}	8.84	8.7
600	2.1536×10^{-6}	1.14×10^{-7}	5.28	17.55
900	2.1682×10^{-6}	8.59×10^{-8}	3.96	26.3
1200	2.1632×10^{-6}	7.57×10^{-8}	3.5	35.05
1500	2.1480×10^{-6}	6.59×10^{-8}	3.07	43.5
1800	2.1583×10^{-6}	7.05×10^{-8}	3.27	52.55
2100	2.1503×10^{-6}	5.02×10^{-8}	2.33	60.9

Table 3.1: for $m = 1,500$, the error associated with the standard deviation is sufficiently small.

increasingly small while simulation running times become prohibitively large. Therefore, an optimum number of particles is required such that statistical accuracy is sufficient while simulation time is minimised. The optimal number of particles is chosen as $n = 1,500$ in the present study.

To demonstrate the accuracy of choosing $n = 1,500$, table 3.1 shows the mean standard deviation of n particles in a direction perpendicular to the imaging beam. The mean is obtained from 20 simulations and the error is defined as half of the total range of the mean standard deviation values, $(std_{max} - std_{min})/2$. The average simulation time for each of the 20 runs is also given. Obviously the statistics in table 3.1 would be more accurate for a greater number of runs, however, table 3.1 is only intended as a guide as opposed to a rigorous analysis. The exposure time for which the particles are walking is fixed at $t_{exp} = 50\ \mu s$ for the data in table 3.1.

3.1.2 Constructing optical depth images

With the analytical form of cold thermal and Bose-condensed atomic density distributions known (see section 1.4.2), a simulated image of an atomic sample can be created. With the random walk statistics described in the preceding section, the 'blurring' effect of atomic random walk motion can thus be added to such an image and its magnitude evaluated.

The process of simulated image generation mimics that of the process of image generation in the laboratory. Firstly, an image of the atomic density distribution is generated. Secondly, a 'background' image is generated and subtracted from the first; this is done primarily as a means of replicating noise present in the imaging system. This gives an *optical depth* image as per Beer's law (equation 5.2), discussed at length in section 5.1.3.

To generate the simulated atomic density distribution image, an $m \times m \times m$ grid is generated and an atomic density is assigned to each grid point using the analytical expressions in section 1.4.2. The grid points are then integrated along one direction to generate an $m \times m$ column density distribution. The atomic density distribution image replicates shining light at the imaging camera in the presence of an atomic sample. Each grid point is set to be the pixel size of the CCD camera used in the present study ($9\ \mu m^2$).

Next, a number of photon counts is assigned to each grid point in the $m \times m$ array using Beer's law (equation 5.2); the count is dependent on the intensity of the imaging laser and the density of the atomic sample. Generally speaking, if the atomic density per grid point is high, the corresponding photon count for that grid point will be low. The converse is also true.

The background image is then created by generating an $m \times m$ grid and assigning

to it a photon count proportional to the intensity of the imaging laser. This replicates shining light at the imaging camera in the absence of an atomic sample. The dimensions of each grid point are the same as the pixel size, as per the grid dimensions for the density distribution image discussed above.

The simulated optical depth image is thus obtained using equation 5.2, which can be expressed as

$$OD = -\ln \frac{I}{I_0}, \tag{3.6}$$

where I_0 is the intensity of the background image and I is the intensity correlating to the presence of an atomic sample.

3.1.3 Incorporation of CCD parameters

If the simulated images discussed above are to accurately replicate an image taken in the laboratory, then the model needs to incorporate the limitations of the imaging camera, discussed in section 5.1. Ensuring the grid sizes in the simulation correspond to the pixel size of the camera is one such example, as described in the preceding section. However, other considerations such as shot noise and well depth also need to be taken into account.

As discussed in section 2.1.2, there is an inherent source of poissonian shot noise on any camera, which is quantum mechanical phenomenologically. Thus, it is important to incorporate this noise into the simulated images as it is inherent to the real imaging system used in the present study.

Adding shot noise to an $m \times m$ array of grid points is straight forward in *Matlab* using the inbuilt function *imnoise*. By passing the appropriate arguments to the *imnoise* function, a random value is chosen for a grid point which is +/- $\sqrt{N}/2$ of the original value of N associated with that grid point.

Also incorporated into the model is the quantum efficiency η of the camera (refer to section 5.1.3). As $\eta = 0.45$ for the camera used in the present study, it is important to ensure that only 45% of the light incident on the simulation image grid gets counted.

The camera well depth limits the amount of photons that can be counted in a given exposure time. The model incorporates this effect by limiting the total amount of photons to be counted equal to the well depth (the impact of the quantum efficiency η is factored into this counting). Whether or not this limit is reached depends on the intensity of the imaging light, which dictates the rate at which photons arrive at the camera, and the exposure time, which dictates the total number of photons that arrive at the camera. It is thus possible to 'overexpose' a simulated image in the same imaging regimes for which a real image taken in the laboratory would be overexposed.

Finally, the model also accounts for the magnification of any image incident on the camera. While this is not strictly a camera parameter, it does effect the intensity and atomic distributions assigned to each grid point of the simulated image.

3.2 Validation of the model

Validation of the numerical model used in the present study can be done in two parts; firstly validating the random walk statistics, and secondly, validating the construction of the optical depth images.

Validating the random walk statistics

The first validation to be performed on the random walk statistics was to ensure that the direction of the momentum kicks corresponding to emission events was random over a unit sphere (see section 3.1). The azimuthal angle ϕ is chosen using the algorithm of equation 3.1 to generate a random value for ϕ between 0 and 2π. Initially, θ was chosen using the algorithm $\theta = \pi R_2$, where R_2 is a random number on the unit interval [0, 1]. However, if this algorithm is used in conjunction with that of equation 3.1, bunching occurs on the unit sphere as per Figure 3.1. Thus, the algorithm used to produce θ needs to be weighted according to the procedure in section 3.1. Once done, the random nature of the directions chosen on the unit sphere could be verified, the results of which can be seen in Figure 3.1 below. Figure 3.1 shows 10,000 points randomly chosen on the unit sphere before and after the random variable θ was weighted correctly.

After the random walk was verified in momentum space, the transformation into co-ordinate space needed to be made and verified also. This can be done by ensuring that the model exhibits the correct behaviour in the limits of certain parameters and also by checking that the analytical statistics of section 2.1.3 are faithfully reproduced.

The accuracy of the random walk in coordinate space depends on the correct inclusion of scattering rates. One of the features of the two-level atom predicted by the Optical Bloch equations (see section 2.1.1) is that the scattering rate increases for laser intensities I below the saturation intensity $I_{sat} = 16.69$ W.m^2. As the intensity approaches saturation, the derivative of the scattering rate decreases. Above saturation intensity, the scattering rate converges on 19 MHz, corresponding to the two-level Rb^{87} transition of interest. Consequently, in the limit of high laser intensity ($I \gg I_{sat}$), the model should also exhibit convergence in this regime, thus providing a good validation check. In Figure 3.2 below, analytical expressions for the scattering rate are compared to rates predicted by the model, and convergence in the appropriate limit is shown. The values predicted by the model are noisy due to their stochastic nature.

The most important model validation performed was to ensure the model exhibited the random walk variances predicted by the analysis of section 2.1.3. The random walk variances in coordinate space are critically important; in order for these numbers to be correct, the numerical model must successfully include accurately distributed random variables for the *direction* of 'emission' momentum kicks, the 'drift' momentum kicks absorbed by atoms in the beam direction, accurately distributed random variables for the duration (in *time*) of all momentum kicks and an accurate transformation from momentum space to coordinate space. The chance of there existing an error in any of these parameters while still accurately predicting the random walk variance in coordinate space is extremely unlikely.

The variance of m atoms random walked for a time t_{exp} can be checked against the theoretical predictions by creating plots of the final positions of the atoms in each dimension of cartesian coordinate space. The *Matlab* function *var* can then be used to extract the variance of the numerical data presented in the plots. For $m = 1,500$ particles random walking a time of $t_{exp} = 50$ μs, with a driving laser intensity of $I = I_{sat}$, a numerical simulation yielded variances of 1.35×10^{-11} m^2 for the x direction, 4.86×10^{-12} m^2 for the y direction, and 4.72×10^{-12} m^2 for the z direction. These results compare very accurately to the analytical expressions of section 2.1.3, which predict variances of 1.32×10^{-11} m^2, 4.59×10^{-12} m^2, and 4.59×10^{-12} m^2 in the x, y, and z directions respectively. It should be noted that a key feature predicted by the analytical expressions for variance, that of a

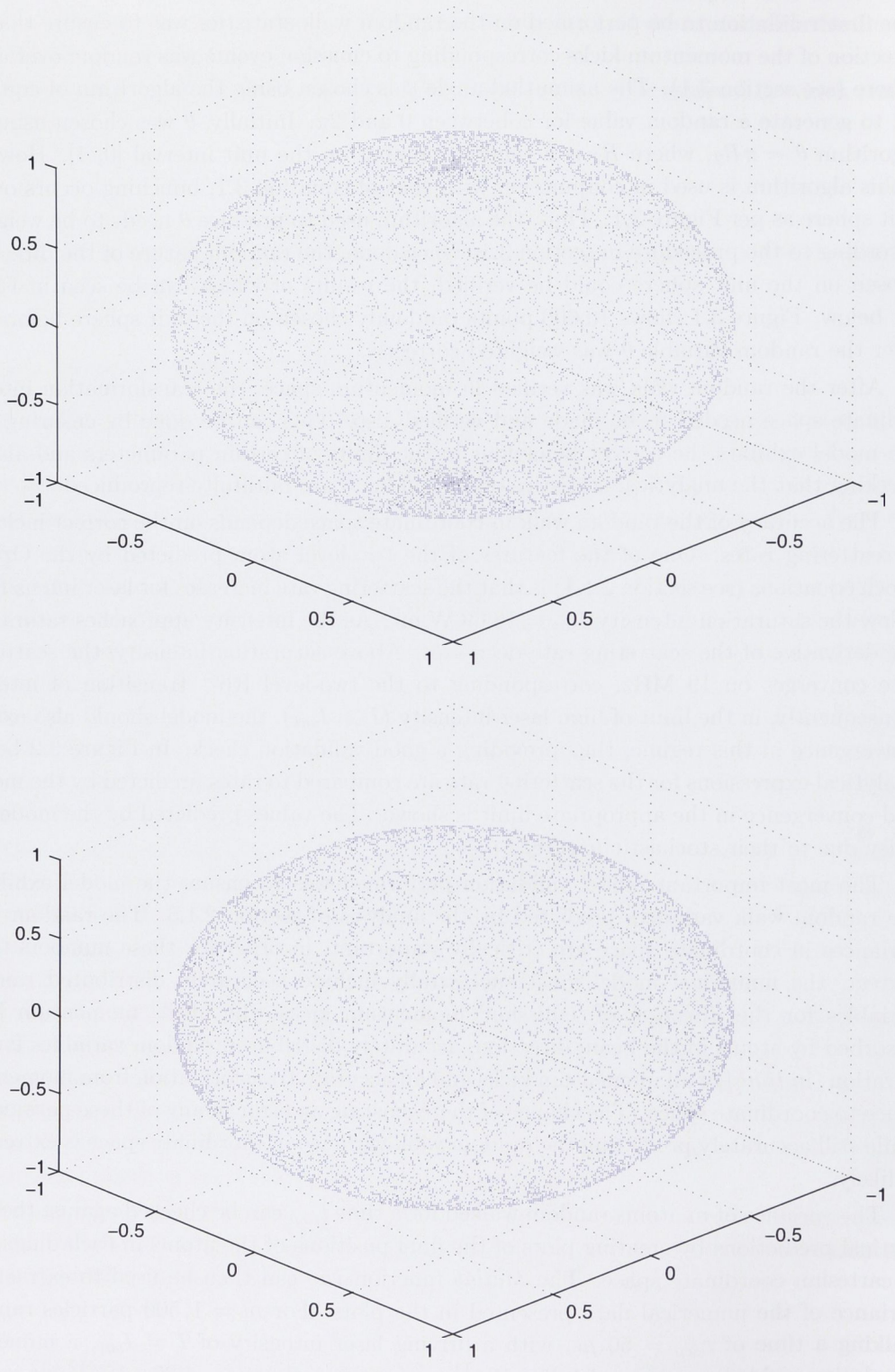

Figure 3.1: Above: polar bunching, and below: even distribution over the unit sphere after weighting the random variable θ.

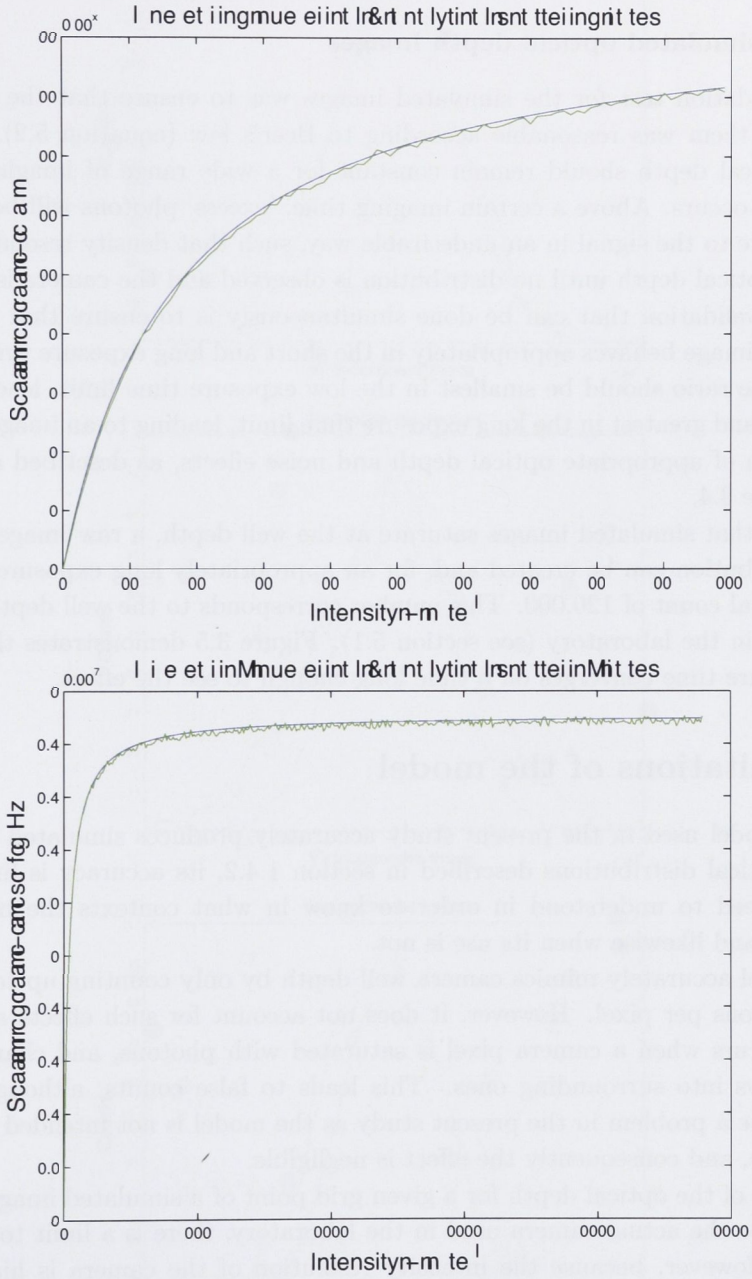

Figure 3.2: Top: scattering rate as a function of intensity in the vicinity of saturation intensity I_{sat} = 16.69 W.m^{-2}, and bottom: scattering rate converging on 19 MHz well above saturation intensity. The solid, blue line is the analytical prediction, while the noisy, green line is the numerical solution. Numerical data was taken using 250 atoms random-walked for an exposure time of t_{exp} = 5 μs.

greater variance in the x direction, is evident in the numerical data. Plots produced using data from the numerical model are compared directly to theoretical predictions, as shown in Figure 3.3.

Validating simulated optical depth images

The first validation test for the simulated images was to ensure that the optical depth indicated by them was reasonable according to Beer's law (equation 5.2). This meant that the optical depth should remain constant for a wide range of imaging times until overexposure occurs. Above a certain imaging time, 'excess' photons will be counted and will contribute to the signal in an undesirable way, such that density resolution decreases along with optical depth until no distribution is observed and the camera is saturated.

Another validation that can be done simultaneously is to ensure that Poisson noise added to the image behaves appropriately in the short and long exposure time limits. The signal to noise ratio should be smallest in the low exposure time limit, leading to a very noisy image, and greatest in the long exposure time limit, leading to an image of low noise.

Validation of appropriate optical depth and noise effects, as described above, can be seen in Figure 3.4.

To check that simulated images saturate at the well depth, a raw image of an atomic density distribution can be created and, for an appropriately long exposure time, should indicate a total count of 120,000. This number corresponds to the well depth of the CCD camera used in the laboratory (see section 5.1). Figure 3.5 demonstrates this saturation as the exposure time converges on a time long enough to see the effect.

3.3 Limitations of the model

While the model used in the present study accurately produces simulated images based on the analytical distributions described in section 1.4.2, its accuracy is limited. These limitations need to understood in order to know in what contexts the model's use is appropriate, and likewise when its use is not.

The model accurately mimics camera well depth by only counting up to a maximum value of photons per pixel. However, it does not account for such effects as 'blooming'. Blooming occurs when a camera pixel is saturated with photons, and charge from that pixel overflows into surrounding ones. This leads to false counts, although this is not expected to be a problem in the present study as the model is not intended to be used in such a regime, and consequently the effect is negligible.

The value of the optical depth for a given grid point of a simulated image can take on any value. For the actual camera used in the laboratory, there is a limit to the intensity resolution. However, because the intensity resolution of the camera is high enough to resolve even shot noise, it is reasonable to ignore this limitation in the model.

For some frequencies of detuned imaging light, lensing effects may be evident in an experimental image of a BEC. While imaging light used in all aspects of the present study is on resonance, the numerical model is not capable of replicating lensing effects, and should not be used in regimes where lensing may be an issue.

An important limitation inherent of the model is that atomic motion can only result after the absorption of an imaging laser photon. Atoms cannot absorb photons which have been re-emitted by another atom after scattering an original laser photon. This effectively results in a reduction of flux compared to what may be present in a real system. For

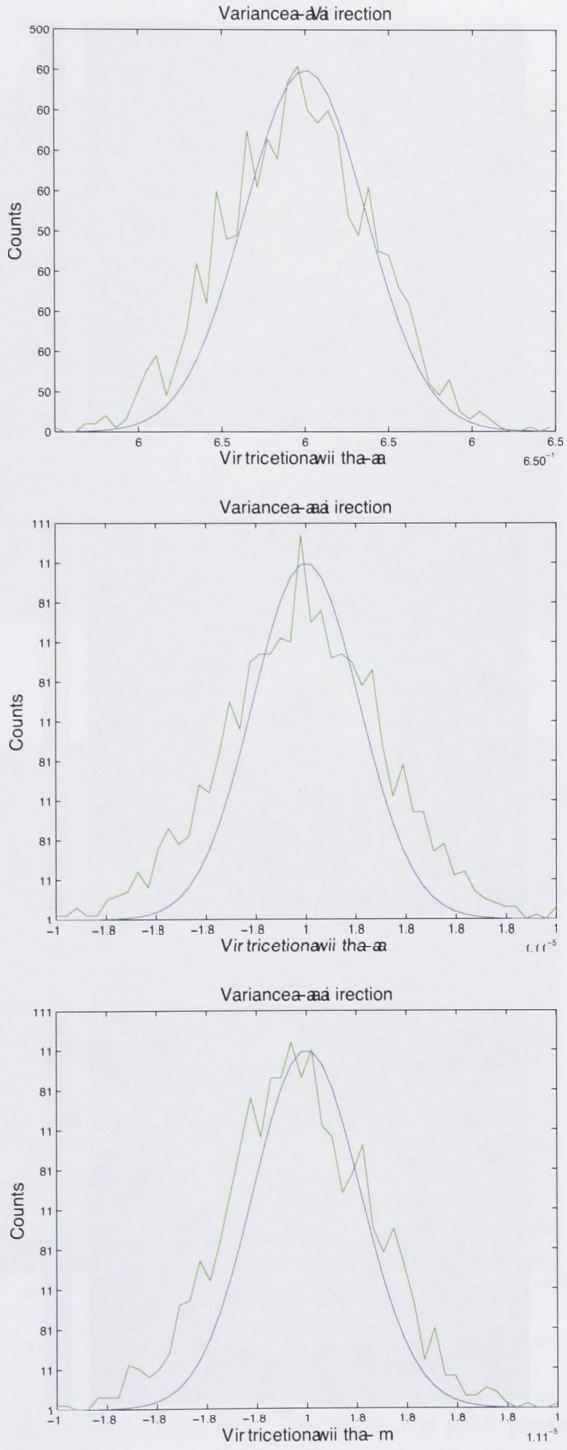

Figure 3.3: Plots showing the variance of $m = 1,500$ particles, after a random walk of duration $t_{exp} = 50$ μs. The noisy, numerical data is shown in green, while the theoretical curve is blue. Variances extracted from the numerical data of 1.35×10^{-11} m^2 for the x direction, 4.86×10^{-12} m^2 for the y direction, and 4.72×10^{-12} m^2 for the z direction, accurately reflect the analytical predictions of 1.32×10^{-11} m^2, 4.59×10^{-12} m^2, and 4.59×10^{-12} m^2 in the x, y, and z directions respectively. Note the greater variance in the x direction, caused by an additional *time* variance in the duration of momentum kicks corresponding to imaging photons absorbed in the beam direction.

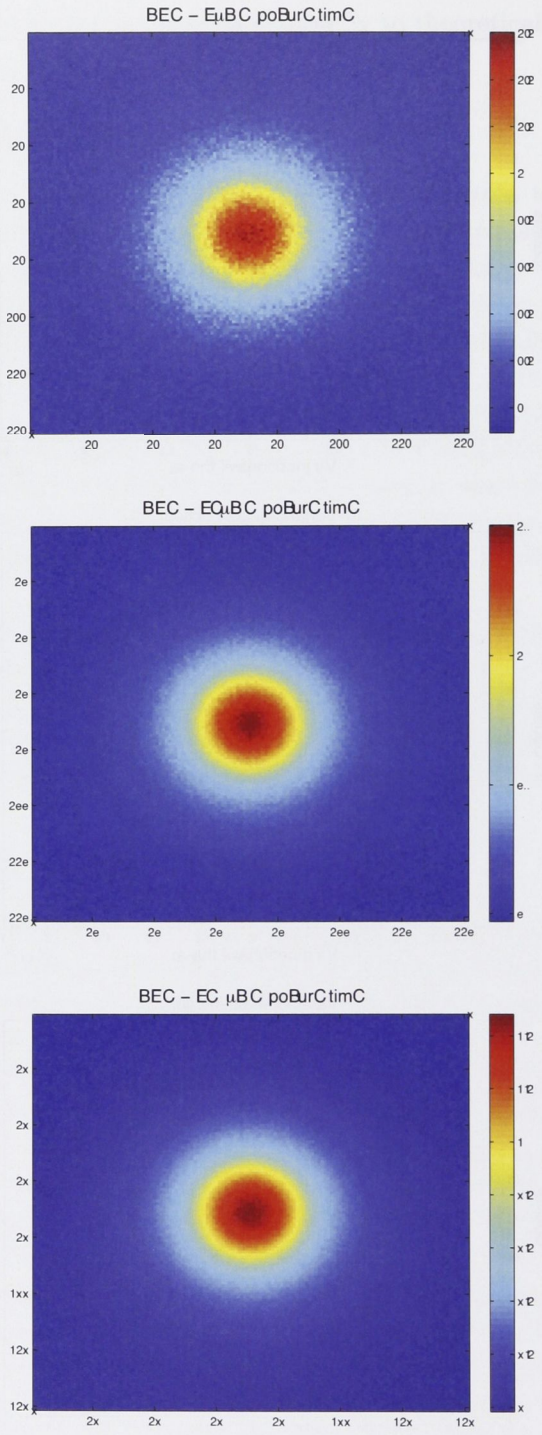

Figure 3.4: From top to bottom, the signal to noise ratio can be seen to improve with exposure time as expected. For the longest exposure time of $t_{exp} = 150$ μs, a reduction in optical depth can be seen as a result of overexposure. The x and y axes are both labeled in pixel number, so as to show the width of the atomic distribution in camera pixels, where the pixel width is 9 μm. The above images are for a simulated condensate comprised of 1.77×10^6 Rb^{87} atoms at 292 nK, which is $0.94\times T_c$ in this case.

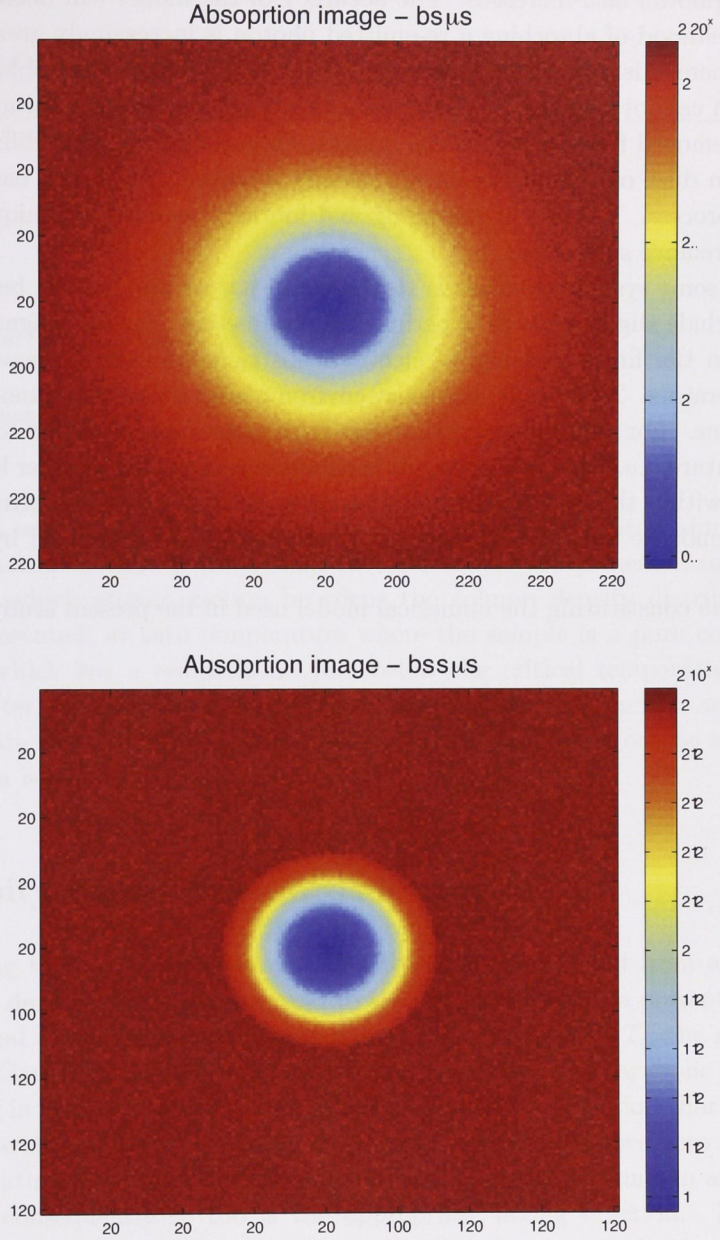

Figure 3.5: Top: for an exposure time of $t_{exp} = 50$ μs, the peak photon count is less than the fictitious well depth of 30,000 (a relatively small value was chosen to highlight the saturation effect), and bottom: for an exposure time of $t_{exp} = 100$ μs, saturation has begun (giving the impression of a smaller distribution) and background counts are capped at the well depth. The x and y axes are both labeled in pixel number, so as to show the width of the atomic distribution in camera pixels, where the pixel width is 9 μm. The above images are for a simulated condensate comprised of 1.77×10^6 Rb^{87} atoms at 292 nK, which is $0.94\times T_c$ in this case.

optically thin systems ($k \ll 1$), absorption of re-emitted atoms is of negligible consequence. However, as the atomic density of system increases, the likelihood of an atom absorbing a re-emitted photon also increases. The accuracy of the model will decrease for systems where the likelihood of absorbing a re-emitted photon is increasingly great.

Finally, there exists systematic noise in any experimental images obtained in the laboratory which cannot be accounted for. Some systematic noise is deterministic in nature and *can* be removed from experimental images. One such example is diffraction patterns resulting from dust on a lens, which are usually removed during the background image subtraction process. The use of averaging and fourier transform techniques may also be employed to remove such noise.

However, some systematic noise is stochastic in nature and cannot be removed. Such noise may include slight drifts in experimental parameters, such as magnetic field offsets, resulting from the finite stability of electrical instruments such as power supplies and function generators. There may also exist environmental noise for unknown and random periods of time. For example, experimental apparatuses are sensitive to noise which is acoustic in nature, i.e. doors slamming or the footsteps of people in other locations around the building within the vicinity of the laboratory. As this noise is arbitrarily random in nature, it cannot be accounted for in the simulated images produced by the analytical model.

The *Matlab* constituting the numerical model used in the present study is displayed in Appendix A.

Chapter 4

Theoretical results

"If the facts don't fit the theory, change the facts."

- Albert Einstein

Theoretical results pertaining to the impact of scattering-induced atomic motion on temperature measurements of Bose-Einstein condensates are presented in this chapter. The nature in which atomic motion broadens the column density distributions in two regimes are presented; at zero temperature where the sample is a pure condensate, and for a sample which has a temperature just below the critical temperature T_c. In the case of the latter, the sample is comprised of a large thermal fraction and a relatively small condensate fraction. The impact of the random walk effect on the temperature of simulation data is then shown.

4.1 Density distribution broadening

Data pertaining to the widths of atomic distributions is extracted from a fit applied to the theoretical data, presented below, and to the experimental data presented in Chapter 5. For a thermal cloud above the condensate critical temperature T_c, the atomic density distribution is Gaussian. At zero temperature, a condensate has a parabolic atomic density profile. Fitting in these temperature regimes requires a fitting function that is respectively Gaussian or parabolic. For a condensate with a temperature above zero but below the critical temperature T_c, the atomic distribution is the sum of a Gaussian and a parabolic function, and consequently so too is the appropriate fitting function. The functional form of theses atomic distributions is discussed in detail in section 1.4.2, while a graphic depiction of them can be found in figure 1.4. Temperatures will be derived from the relative amplitudes of the two components of the fitting function.

The general form of the gaussian function used for fitting is

$$f_g = \frac{1}{\sigma\sqrt{2\pi}} \exp\left(\frac{(x-\mu)^2}{2\sigma^2}\right). \tag{4.1}$$

In the *Matlab* function used for fitting, the denominator in the exponent of equation 4.1 is represented by one free parameter. This free parameter is used to define the width of the thermal fraction.

The general form of the parabolic function used for fitting is

$$f_p = \alpha \mathbb{R}\mathrm{e}\left[\left(1 - 0.5\left(\frac{(x-\mu)^2}{\sigma^2}\right)\right)^{\frac{3}{2}}\right]. \tag{4.2}$$

Similar to the *Matlab* function used for fitting a gaussian distribution, the σ^2 term in the denominator of the fraction in parenthesis of equation 4.2 is described by one free parameter, which is used to define the parabola's width.

4.2 Temperature measurement of the $T = 0$ condensate

For a variety of exposure times ranging from 30 μs to 270 μs, the numerical model described in Chapter 3 was used to produce a zero temperature condensate without the random walk effect present. Then, for the same exposure times, a zero temperature condensate *with* the random walk effect present was also produced. The width of the distributions in both cases were measured, for each exposure time, using the fitting functions described in section 4.1. The distributions are compared and the impact of the random walk effect on temperature discussed.

For both the cases under study in this section, the condensate is comprised of $N = 5.65 \times 10^5$ Rb^{87} atoms, having 'fallen' from a harmonic trap with trap frequencies ω_{tight} of $2 \times \pi \times 128$ Hz in the tight directions and $2 \times \pi \times 12.8$ Hz in the weak trapping ω_{weak} direction. These parameters yield a critical temperature T_c of 221.2 nK for this condensate. The free-fall time t_{ff} of the condensate is 16.9 ms, while the scattering length a is 5.77 nm. The atoms are 'imaged' in the simulation using resonant light at the saturation intensity $I = 16.69$ W.m^{-2}, and the atomic distribution has a peak optical depth of 2.2, which is at a maximum for the shortest exposure time t_{exp} of 30 μs.

The results for the case of a pure condensate without the random effect are displayed in figure 4.1, where the error bars were generated using the 95% confidence intervals produced when fitting. The 95% confidence interval is the interval over which there is a 95% chance of finding the actual value of the parameter for which the fit has produced. Figure 4.1 shows the width of the pure condensate slowly broadening in a linear fashion as the exposure time increases. This slow, linear broadening simply reflects the ballistic expansion of the condensate as expected (see section 1.4.2). If this result was not evident, it would infer a fault in the simulation code.

Although the distribution broadens as a function of exposure time, it still retains a *parabolic* form, as expected if *all* the atoms in the simulation were in the ground state of the trap before being released. Consequently, using the parabolic fitting function is suitable for all exposure times and, because there is no thermal fraction present, the temperature of the system is accurately measured as 0 K, as it is programmed to be.

When the simulation is repeated *with* the random walk effect present, the results are markedly different, for two reasons. Firstly, the random walk effect results in the distribution broadening at a rate faster than the expected ballistic expansion. Further, it is not linear in nature like ballistic expansion, but rather has an approximately quadratic nature. This 'additional' broadening as a result of the random walk effect is shown in figure 4.2. Again, the error bars in figure 4.2 were generated using the 95% confidence intervals produced when fitting.

The second consequence of the random walk effect is that the *shape* of the density distribution changes; it no longer retains its parabolic form for any exposure time. Therefore a standard fitting function which is the sum of a parabola (for the condensate) and a gaus-

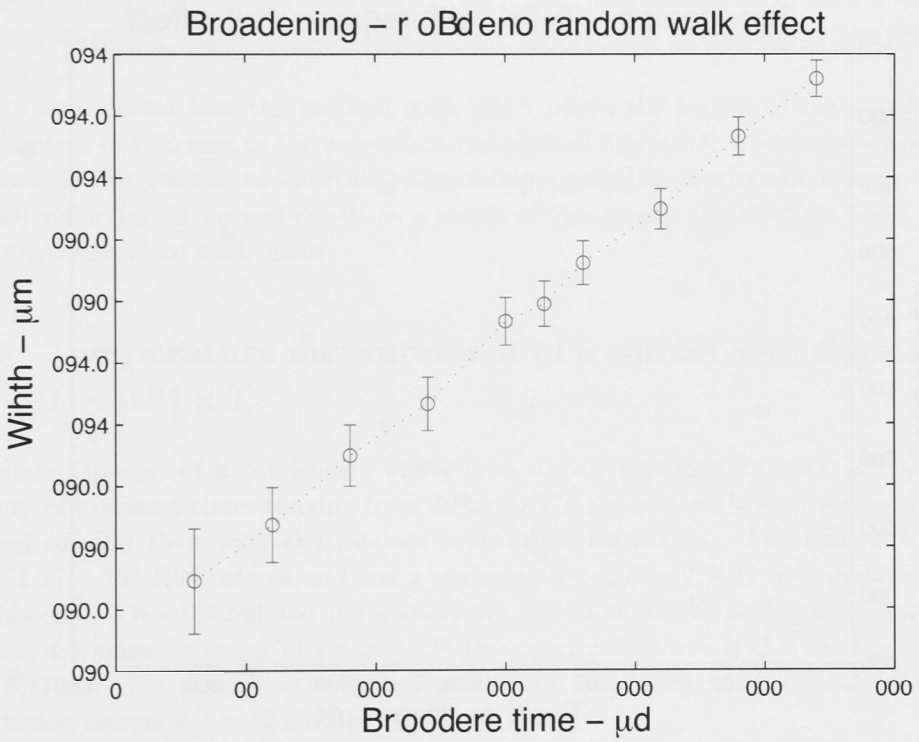

Figure 4.1: Theoretical prediction of density distribution broadening of the zero temperature Rb^{87} condensate, *without* random walk effects. $N = 5.65 \times 10^5$ atoms, $T_c = 221.2$ nK, $\omega_{tight} = 2 \times \pi \times 128$ Hz, $\omega_{weak} = 2 \times \pi \times 12.8$ Hz, $t_{ff} = 16.9$ ms, $a = 5.77$ nm and $I = 16.69$ W.m^{-2}.

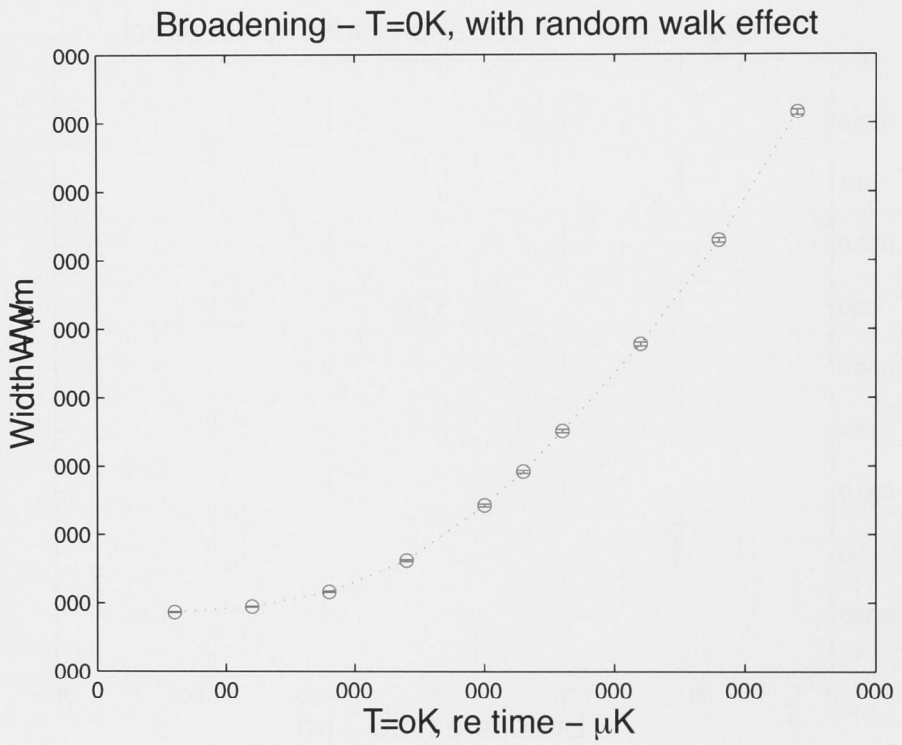

Figure 4.2: Theoretical prediction of density distribution broadening of the zero temperature Rb^{87} condensate, *with* random walk effects. $N = 5.65 \times 10^5$ atoms, $T_c = 221.2$ nK, $\omega_{tight} = 2 \times \pi \times 128$ Hz, $\omega_{weak} = 2 \times \pi \times 12.8$ Hz, $t_{ff} = 16.9$ ms, $a = 5.77$ nm and $I = 16.69$ W.m^{-2}.

sian (for the thermal fraction) can be used. The effect of the random walk is to add 'wings' to the atomic distribution such that as exposure time increases and the effect becomes more noticeable, the distribution changes from a parabolic form to something resembling a gaussian. As a result, the fitting function 'thinks' there is a thermal fraction associated with the distribution which grows larger with time, and fits accordingly. For exposure times upward of 210 μs, a false thermal fraction is completely dominant in the fitting function. In fact, the condensate fraction essentially 'disappears', leaving only the thermal fraction and the implication that the measured temperature should increase, which it does. Under such circumstances, it would be expected that the measured temperature would converge on the critical temperature T_c according to equation 1.52. Indeed, this is evident in figure 4.4, which shows the impact of random walking on the measurement of temperature in this case. In addition to this effect, we also *lose* some information about the system as the signal to noise ratio for any given pixel is reduced as the distribution increases.

An example of how the random walk effect alters the profile of the atomic density distribution can be seen in the cross-sectional plots of figure 4.3. The transformation from a parabolic distribution to something resembling a gaussian distribution is clear. Note the overall reduction in optical depth as a result of the atomic distribution being 'smeared out' by the random walk effect.

4.3 Temperature measurement of a condensate simulated at $T = 0.94 \times T_c$

Simulated images of a condensate above zero degree temperature were produced for a variety of exposure times ranging from 30 μs to 270 μs, first with the random walk effect turned off and then with the random walk effect turned on. The system consists of $N = 1.77 \times 10^6$ Rb^{87} atoms and has a temperature of $T = 279.37$ nK, which is $0.94 \times T_c$ in this case. Other simulated parameters are the same as the zero temperature case of section 4.2, namely: $\omega_{tight} = 2 \times \pi \times 128$ Hz, $\omega_{weak} = 2 \times \pi = \times 12.8$ Hz, $t_{ff} = 16.9$ ms, $a = 5.77$ nm. The atoms are again 'imaged' in the simulation using resonant light at the saturation intensity $I = 16.69$ W.m^{-2}.

For the case where the random walk has been excluded, the width of the thermal fraction was measured for each exposure time and is displayed in figure 4.5. As with the zero degree temperature condensate without random walk effects, the width of the distribution slowly increases in a linear manner. This slow linear increase reflects the expected ballistic expansion and, as with the plots of the preceding section, the error bars in figure 4.5 were generated using the 95% confidence intervals. As seen in figure 4.8, when the random walk has been excluded, the measured temperature of the system remains essentially constant.

Figure 4.6 shows the broadening of a condensate at $0.94 \times T_c$ for a range of exposure times, where the random walk effect has been included. As with the case where random walking hasn't been included, the system has a temperature of $T = 279.37$ nK. Unlike the case where random walks haven't been included (figure 4.5), the width increases approximately in a quadratic fashion. Consequently, the width for exposure times above 120 μs is significantly larger than when random walk effects have been ignored. To gauge the significance of this effect, a cross-sectional plot of the atomic density distribution profiles for both cases, with and without the random walk effect, is presented in figure 4.7. Not

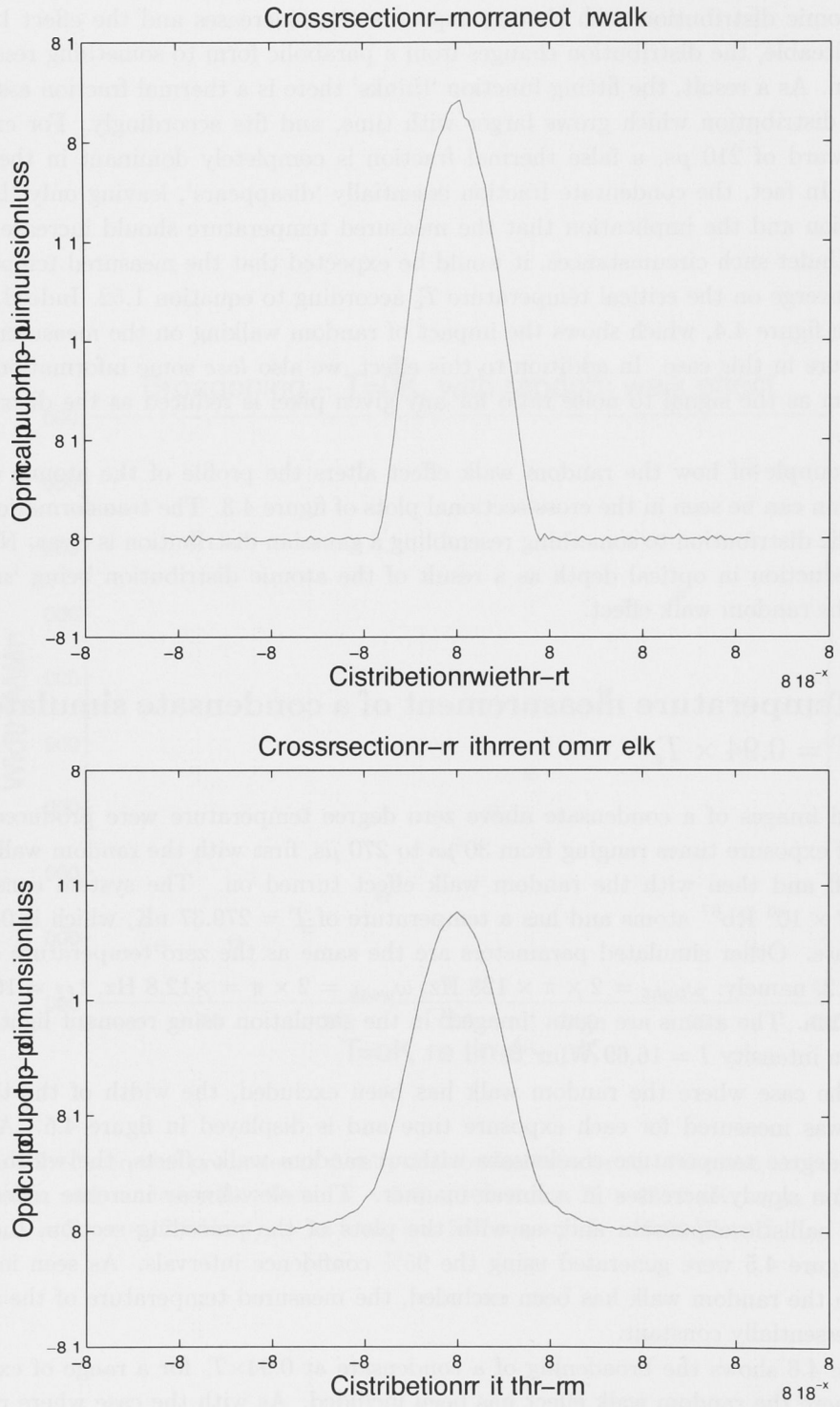

Figure 4.3: Above: a zero temperature condensate 'imaged' for an exposure time of $t_{exp} = 270\mu$s without the random walk effect, while below: the same condensate 'imaged' for the same exposure time *with* the random walk effect included. $N = 5.65 \times 10^5$ atoms, $T_c = 221.2$ nK, $\omega_{tight} = 2 \times \pi \times 128$ Hz, $\omega_{weak} = 2 \times \pi \times 12.8$ Hz, $t_{ff} = 16.9$ ms, $a = 5.77$ nm and $I = 16.69$ W.m^{-2}.

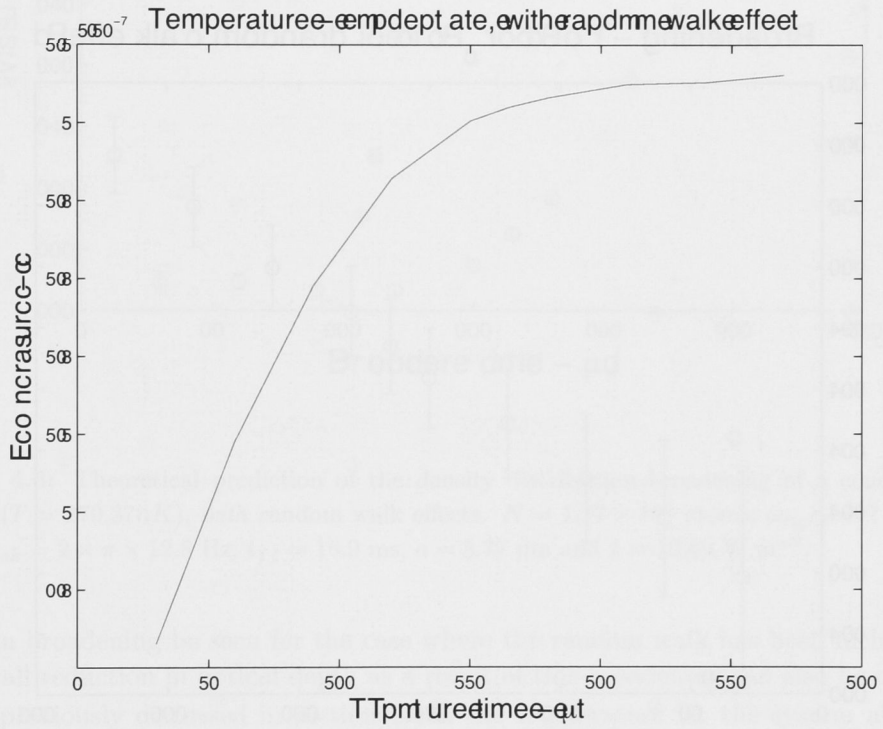

Figure 4.4: Measured temperature of a Rb^{87} condensate, simulated with the random walk effect on and simulation temperature set to zero (without the random walk effect, the measured temperature of the system remains zero for all exposure times as there is never a perceived thermal fraction present). $N = 5.65 \times 10^5$ atoms, $T_c = 221.2$ nK, $\omega_{tight} = 2 \times \pi \times 128$ Hz, $\omega_{weak} = 2 \times \pi \times 12.8$ Hz, $t_{ff} = 16.9$ ms, $a = 5.77$ nm and $I = 16.69$ W.m^{-2}.

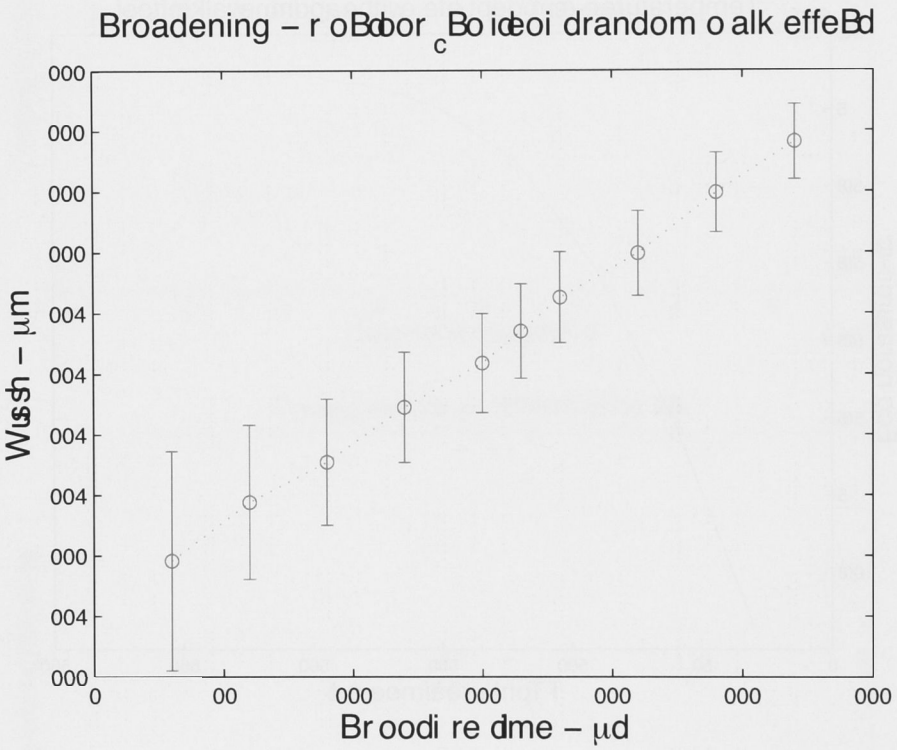

Figure 4.5: Theoretical prediction of the density distribution broadening of a condensate at $0.94 \times T_c$ ($T = 279.37nK$), *without* random walk effects. $N = 1.77 \times 10^6$ atoms, $\omega_{tight} = 2 \times \pi \times 128$ Hz, $\omega_{weak} = 2 \times \pi \times 12.8$ Hz, $t_{ff} = 16.9$ ms, $a = 5.77$ nm and $I = 16.69$ W.m^{-2}.

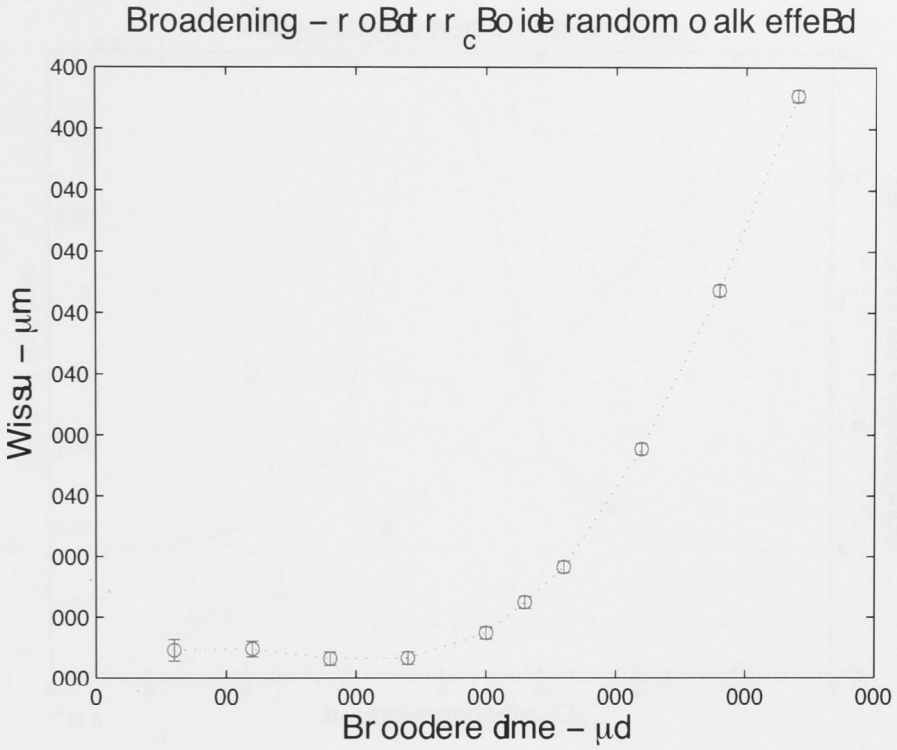

Figure 4.6: Theoretical prediction of the density distribution broadening of a condensate at $0.9 \times T_c$ ($T = 279.37nK$), *with* random walk effects. $N = 1.77 \times 10^6$ atoms, $\omega_{tight} = 2 \times \pi \times 128$ Hz, $\omega_{weak} = 2 \times \pi \times 12.8$ Hz, $t_{ff} = 16.9$ ms, $a = 5.77$ nm and $I = 16.69$ W.m^{-2}.

only can broadening be seen for the case where the random walk has been included, but an overall reduction in optical depth as a result of this broadening can also be observed.

As previously discussed in section 1.4.2, the temperature for the system above zero temperature is related to the relative size of the thermal and condensate fractions. For the bimodal system under study here, the condensate fraction contains $\sim 1.07 \times 10^5$ atoms while the thermal fraction contains a significantly larger number of $\sim 1.66 \times 10^6$ atoms. Thus the system is at a temperature cooler than, but close to, the critical temperature of $T_c = 310.4$ nK.

As can be seen in figure 4.8, the temperature of the system appears to actually increase with exposure time, in an approximately linear way, for the case where the random walk *has* been included in the mixed system. This is in contrast to the case where the random walk has been left off; there is essentially no change in measured temperature, also shown in figure 4.8. This increase in temperature implies that, as exposure time increases, the random walk effect increasingly alters the atomic distribution in a way such that the thermal fraction becomes larger relative to the condensate fraction when the fitting function is applied to the data. Consequently, the random walk effect *does* appear to affect the accuracy of temperature measurement in this case, where the temperature measured increases monotonically with exposure time. Further, broadening due to the random walk effect reduces the signal to noise ratio for the counts on any given pixel, resulting in the loss of some information pertaining to the atomic distribution of the system. The implications of

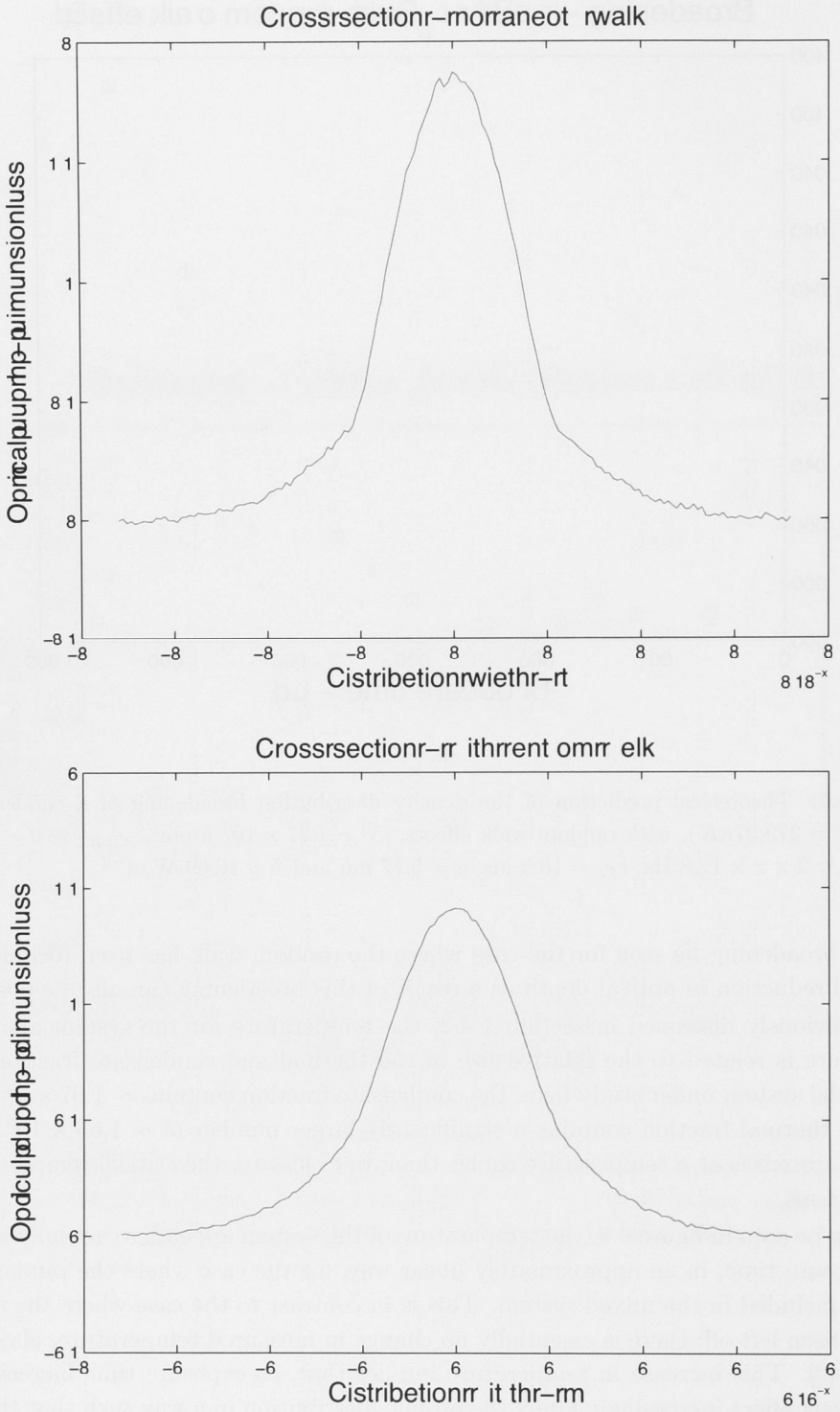

Figure 4.7: Above: a condensate with temperature $T = 0.94 \times T_c$ ($T = 279.37$ nK) 'imaged' for an exposure time of $t_{exp} = 270$ *mus* without the random walk effect, and below: the same condensate 'imaged' for the same exposure time *with* the random walk effect included. $N = 1.77 \times 10^6$ atoms, $\omega_{tight} = 2 \times \pi \times 128$ Hz, $\omega_{weak} = 2 \times \pi \times 12.8$ Hz, $t_{ff} = 16.9$ ms, $a = 5.77$ nm and $I = 16.69$ W.m^{-2}.

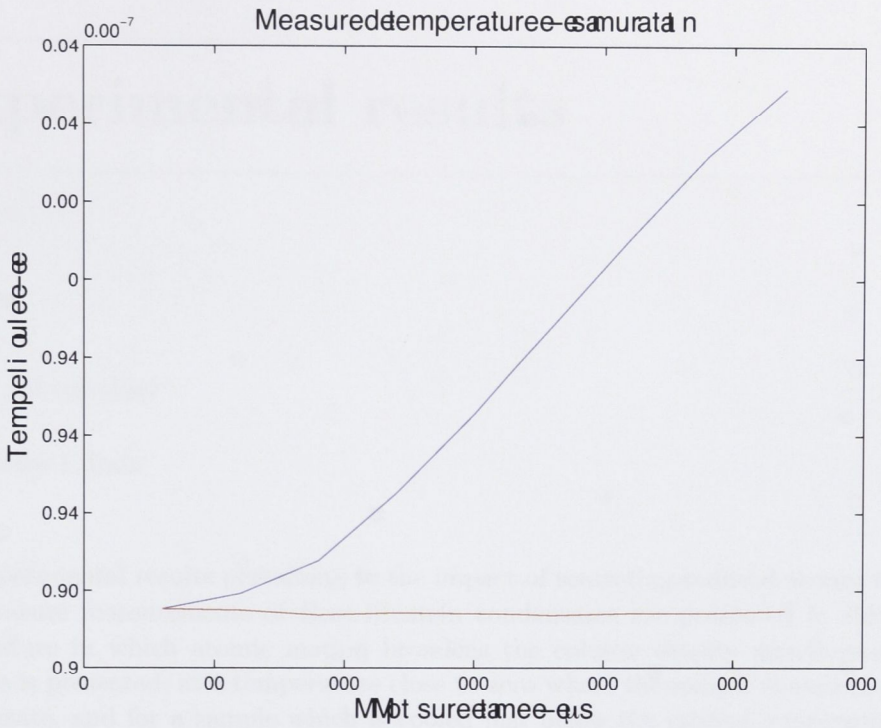

Figure 4.8: Measured temperature of a simulated condensate at $0.94 \times T_c$ ($T = 279.37$ nK), as a function of exposure time. The blue line shows the case with the random walk effect on, the red line when it is not. $N = 1.77 \times 10^6$ atoms, $\omega_{tight} = 2 \times \pi \times 128$ Hz, $\omega_{weak} = 2 \times \pi \times 12.8$ Hz, $t_{ff} = 16.9$ ms, $a = 5.77$ nm and $I = 16.69$ W.m^{-2}.

this increase in temperature will be discussed in Chapter 6, after the results of Chapter 5 have been presented.

Chapter 5

Experimental results

"Who ordered that?"

- Isidor I. Rabi

Experimental results pertaining to the impact of scattering-induced atomic motion on temperature measurements of Bose-Einstein condensates are presented in this chapter. The nature in which atomic motion broadens the column density distributions in two regimes is presented; at a temperature close to zero where the sample is essentially a pure condensate, and for a sample which is cooled just below the critical temperature T_c. In the case of the latter, the sample is comprised of a large thermal fraction and a relatively small condensate fraction. The impact of the random walk effect on the temperature measurement of experimental data is then shown.

5.1 Experimental setup & imaging technology

Experimental data presented in this chapter was created using the third generation BEC machine of ANU's BEC & atom laser group. The machine, shown in figure 5.1, is comprised of three stages, each of which trap and cool atoms such that a BEC can be produced in the last stage.

The first stage of the machine is a two-dimensional magneto-optical trap (MOT) which is used to 'catch' Rb atoms from a dispenser over a period of around ten seconds. The atoms are then moved to a three-dimensional compression MOT in the second stage where polarisation gradient cooling is used to cool atomic samples to an appropriate temperature in preparation for RF-induced evaporative cooling. The atoms are then transported to the third stage of the machine over a period of around seven seconds using a translation stage mounted on skateboard wheels. Once trapped in the third stage using a magnetic harmonic potential, an atomic sample may then be further cooled over a period of around twenty seconds to produce a Bose-Einstein condensate using RF-induced evaporative cooling.

5.1.1 Imaging laser

The laser used for imaging the Bose-Einstein Condensate in the present study is an external cavity diode laser with a wavelength of 780 nm, chosen with consideration to the resonant, Rb^{87} transition depicted in figure 2.1. The laser is locked to a Rb^{87} reference cell such that it is kept on the above transition, the linewidth of which is $2\pi \times 6.6$ MHz (see equation

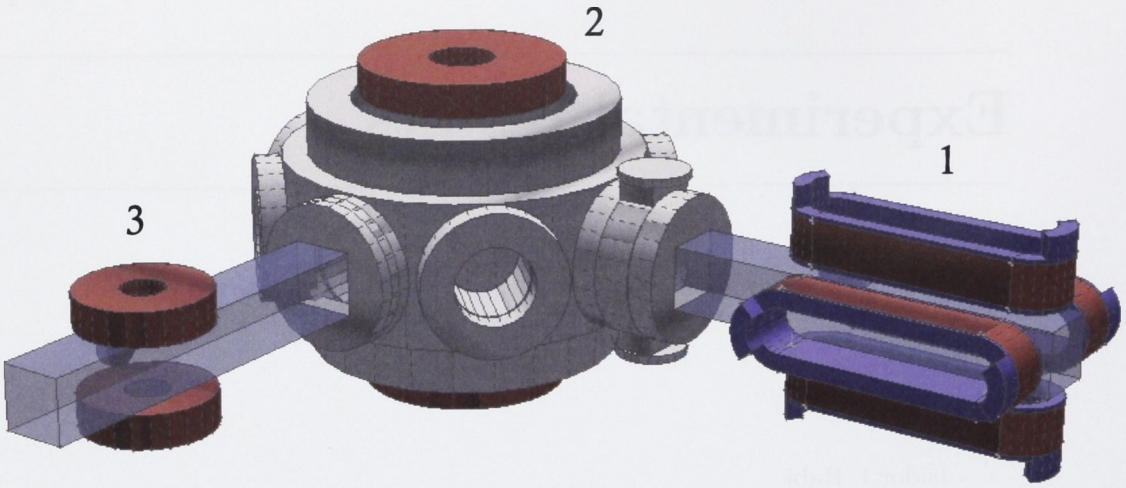

Figure 5.1: A three dimensional view of the third generation BEC machine made by ANU's BEC & atom laser group. The three regions within the vacuum system where the various stages of trapping and cooling occur are labelled 1 (2D MOT), 2 (3D compressed MOT and polarisation gradient cooling) and 3 (evaporative cooling & BEC) respectively. Thank you to Cristina Figl and Matt Jeppeson for allowing use of the image.

2.8). As the linewidth of the imaging laser is 130 kHz, it can effectively be considered monochromatic as it is more narrow than the 6MHz transition it drives.

The imaging exposure time and laser intensity is controlled by an Acousto-Optical Modulator (AOM). Imaging times used in the present study are as short as 30 μs, and since lasers cannot be switched on, stablised, and switched off again this quickly, an AOM is used for 'switching'. The AOM can be switched on and off on the order of tens of nano-seconds, more than sufficiently quick for the minimum exposure time. When the AOM is off, the laser beam passes straight through it and into a beam dump. When it is switched on, acoustic waves set up in a piezo-electric crystal housed inside the AOM redirect the beam into the path of the BEC such that it can be imaged. The magnitude of these acoustic waves determines the intensity of the imaging light, and can be controlled by varying an input voltage to the AOM.

5.1.2 Optics

The imaging optics employed in the present study are basic and straight forward. The atomic samples under study are produced in a glass cell. Imaging light is shone through the glass cell in the region where the atomic sample is present. Any light which is not absorbed by the sample exists the other side of the cell and is magnified, using a lens, by a magnification factor of $M = 2.4$. The imaging set-up can be viewed in figure 1.1, section 1.1.

The most significant parameter of the optics set-up with regards to limitations is the diffraction limit ℓ_{diff}. The diffraction limit is a function of the wavelength λ of the imaging light, the width w of the magnification lens, and the distance d between the lens and the imaging camera. The diffraction limit is defined as

$$\ell_{diff} = 1.22\lambda\frac{d}{w} \approx 1.22 \times 780 \cdot 10^{-9}\text{nm} \times \frac{33\text{cm}}{5\text{cm}} = 6.3\mu\text{m}. \tag{5.1}$$

Referring to the schematic diagram of figure 1.1, the lens width in the present study is 5 cm while the distance between the lens and camera is 33 cm, resulting in a diffraction limit of 6.3 μm. While this is a fundamental limit of spatial resolution, it is not the only one. The pixel size of the camera used for imaging is also a fundamental limit on the same order of magnitude, and the larger of these two values sets the absolute resolution limit of the system. Spatial resolution is discussed further in section 5.1.3.

5.1.3 Camera

A CCD (Charge-Coupled Device) camera is used to capture the image of the BEC during the absorption imaging process. The camera used in the present study has a Kodak KAF-0401E CCD image sensor. The sensor is comprised of an array of 393k effective pixels, each of which acts as photon counter such that information pertaining to the intensity of light incident on each pixel is stored.

The intensity of the light incident on the camera is dictated by Beer's law

$$I = I_0 e^{OD}, \tag{5.2}$$

where I_0 is the initial intensity of the imaging light and OD is the optical depth, given by

$$OD = \sigma \int n(x, y, z)dx, \tag{5.3}$$

where σ is the absorption cross section (see equation 2.10) and the integrated term is the column density, integrated along the direction of the imaging beam.

The characteristics and performance specifications of the camera limit the quality of the image captured. Consequently, these limitations imply that an optimum imaging regime exists, which will later be discussed later in Chapter 6. The most limiting characteristics of the camera, and therefore the most relevant when imaging, include pixel size, well depth, quantum efficiency, camera noise, and digital conversion rate.

Pixel size

Like the diffraction limit discussed in section 5.1.2, the pixel size also limits the spatial resolution of the image. The larger of these two parameters sets the maximum spatial resolution of the image, and any image structure which occurs on a smaller length scale cannot be resolved. The pixel size of the KAF-0401E CCD image sensor is 9 μm^2, and given the diffraction limit in the imaging plane is 6.3 μm, the pixel size is the limiting factor with respect to the spatial resolution of the image. Therefore, any image structure on a scale smaller than 9 μm cannot be resolved by the imaging system used in the present study. In fact, given the condensate trap frequencies used in the present study are $2\pi \times 12.8$ MHz (weak axis) and $2\pi \times 128$ MHz (tight axis), a trapped condensate has a width close to $M \times 6$ μm in the imaging plane. This is on the order of the diffraction limit! This is one reason why the condensate is released from the trap before imaging, as balistic expansion increases the size of the condensate image. This expansion, combined with magnification, allows for greater spatial resolution during the imaging process.

Well depth & quantum efficiency

Each camera pixel has associated with it a 'well depth' which is defined as the number of electrons located in each pixel available to store as charge during the imaging process. For the KAF-0401E CCD image sensor, the well depth is specified as 120,000 electrons. When a photon is incident on a pixel, the energy of the photon 'pushes' an electron from within the 'well' to the back of the pixel where it is stored as a unit of charge. The magnitude of charge built up per pixel during the imaging process is directly proportional to the number of photons incident on the pixel. However, the photon counting process is not perfect; not all photons incident on the pixel will be counted. Thus each pixel also has associated with it a quantum efficiency η, which is uniform across all pixels for a given camera. For the KAF-0401E CCD image sensor, $\eta = 0.45$ for photons with a wavelength of 780 nm, so 45% of photons incident on each pixel will be detected in the case of the present study.

In the case where the number of photons incident on a pixel is greater than well depth divided by η, saturation of the pixel may occur and charge from a saturated pixel may spill into the surrounding pixels, registering false counts. This phenomenon is sometimes referred to as 'blooming', and can be avoided by keeping camera exposure times within an appropriate range depending on the intensity of the imaging light.

Camera noise & digital conversion

There are two types of noise that affect the number of photon counts per pixel during absorption imaging; the quantum mechanical shot noise, discussed in section 2.1.2, and the 'dark noise' inherent of the camera. The dark noise is attributable to thermal electrons within the pixel which register themselves as charge to be counted without having been influenced by an incident photon, thereby contributing a false count to the total photon count per pixel. Such false counts are known as 'dark counts'.

The larger of these two types of noise determines the minimum amount of noise per pixel. The nominal dark noise for the KAF-0401E CCD image sensor is given by the technical specifications as 25 electrons per pixel, per second, with a maximum possible number of 50 electrons per pixel, per second (averaged over all pixels at 25 °C with no illumination). In the present study, the maximum exposure time is 300 μs, which means that at most, we would expect a maximum dark count of 300 μs $\times$ 50 = 0.015 electrons.

It is worth digressing here to consider the digital conversion rate of the KAF-0401E. The digital conversion rate, or bit rate, is a measure of how well the camera is capable of resolving the charge that is stored in a pixel during the imaging process. The KAF-0401E CCD image sensor is specified as having a conversion rate of 12-bits, which means it can resolve the full scale charge range of 120,000 electrons (the well depth) into 2^{12} = 4,096 increments. Thus, the camera can resolve 29 units of charge, or 29 photon counts. This means that the camera will never be able to resolve the dark noise discussed in the preceding paragraph.

Further, the camera will be shot noise limited for counts per pixel in excess of 29^2 = 841 counts (refer to equation 2.19). The minimum exposure time used for imaging in the present study is 30 μs. Given the intensity of the imaging laser is always 16.69 W.m^{-2}, the maximum count per pixel is 12,475 counts over 30 μs. Of course, the number of counts for some pixels will be reduced as the atomic sample under study will absorb light according to equation 5.2. This implies that for every exposure time, there will be a maximum optical depth (OD) below which shot noise can be resolved by the detector. The maximum OD for which images are shot noise limited is shown for various exposure

t_{exp} - (μs)	I_{min} - W.m^{-2}	OD
30	1.13	2.70
60	0.56	3.39
90	0.38	3.80
120	0.28	4.08
150	0.23	4.31
165	0.20	4.40
180	0.19	4.49
210	0.16	4.64
240	0.14	4.78
270	0.13	4.89
300	0.11	5.00

Table 5.1: The minimum intensity per pixel, and corresponding maximum optical depth measured per pixel, for which the signal on the pixel is shot noise limited. The minimum OD increases with the exposure times t_{exp} used in the experiment, as displayed above.

times in table 5.1.

5.2 Temperature of a $T = 0.94 \times T_c$ condensate

The sequence of experimental images from which the broadening data of a non-zero temperature condensate is extracted, is shown in figure 5.2. Broadening of the atomic distribution beyond that of ballistic expansion can be seen.

Figure 5.3 shows a plot of the broadening of a $T = 0.94 \times T_c$ (T =305 nK) condensate produced in the laboratory for a range of exposure times between 30 μs and 270 μs. The condensate is comprised of $N = 1.77 \times 10^6$ Rb^{87} atoms with a scattering length $a = 5.77$ nm. For all exposure times, the condensate free-fell $t_{ff} = 16.9$ ms before being imaged with resonant light at the saturation intensity $I = 16.69$ W.m^{-2}. The 'cigar' shaped condensate was made in a three-dimensional harmonic trap with a 10:1 ratio and imaged along the weak trapping axis; the trapping frequencies in the tight directions were $\omega_{tight} = 2 \times \pi \times 128$ Hz, while the trapping frequency in the weak direction was $\omega_{weak} = 2 \times \pi \times 12.8$ Hz.

The error bars in figure 5.3 were generated using the 95% confidence intervals produced when fitting. In this instance, the thermal fraction broadens approximately in a quadratic manner. This is simlar to the theoretical case of a $T = 0.94 \times T_c$ condensate where random walk effects have been included, also shown in figure 5.3. This suggests that random walking is present and further, it appears to adhere to the analytical statistics presented in section 2.1.3.

While there seems to be good correlation between the theoretical and experimental broadening *trends*, theoretical data for any given exposure time is offset from the experimental data such that the theoretical predicitions are generally 'larger'. This offset is the result of an assumption made in the functional form of the fitting function. Recall that the width of the system is defined as the width of the system's thermal fraction, as per equation 4.1 of section 4.1. The gaussian form of this function is an approximation of the Bose function, as described in equation 1.54 of section 1.4.2. This assumption is made as the gaussian form of the fitting function easier to work as well as being less computationally intensive throughout the fitting process. This assumption is also used in

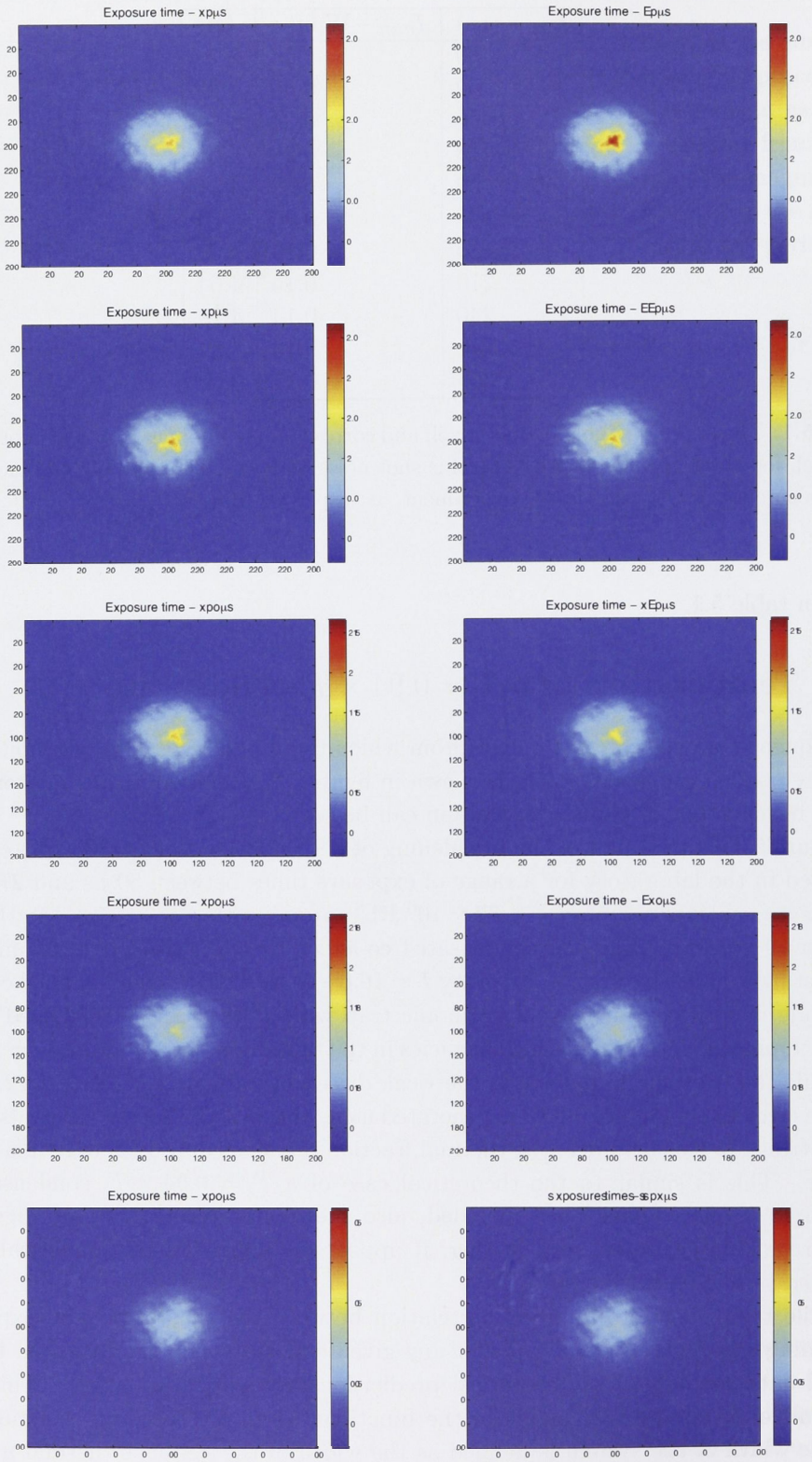

Figure 5.2: Raw experimental images of a $T = 0.94 \times T_c$ system expanding as exposure time increases. The false colour scale indicates optical depth while the x and y axes represent pixel numbers associated with the imaging camera.

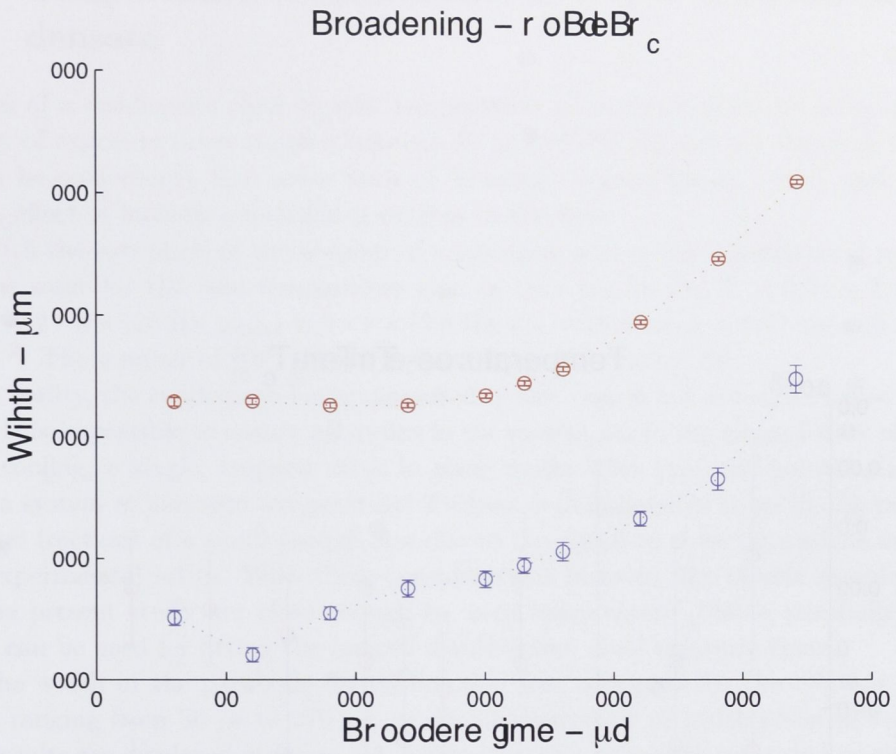

Figure 5.3: In blue, the experimental results of the density distribution broadening of a T = $0.94 \times T_c$ condensate, as measured in the laboratory. For comparison, the theoretical results, first presented in section 4.3, are also shown here in red. Relevant experimental parameters pertaining to the experimental data presented in this figure are: $N = 1.77 \times 10^6$ Rb^{87} atoms, $\omega_{tight} = 2 \times \pi \times 128$Hz, $\omega_{weak} = 2 \times \pi \times 12.8$ Hz, $t_{ff} = 16.9$ ms, $a = 5.77$ nm and $I = 16.69$ W.m^{-2}.

the creation of the simulated data, so the fitting function is expected to fit the simulated data more accurately than experimental data in this regime. As it can be seen in figure 5.4, the impact of this assumption appears to very small given the difference in measured temperatures in either the simulated or experimental cases for any given exposure time.

In the theoretical case of $T = 0.94 \times T_c$ condensate, the impact of scattering-induced broadening appeared to result in a slight, gradual increase in temperature. However, for the experimentally similar system, the temperature actually appears to *decrease* with exposure time, as seen in figure 5.4. This implies that the size of the thermal fraction grows smaller relative to the condensate fraction, in contrast to the simulated case. Although the decrease in temperature is generally linear, the trend is not strong; the noise associated with the temperature trend is relatively large. Again, the difference in results is related to the assumption that absorption of light from re-emitting photons does not occur. These results, as well as the results presented in the next section (5.3), will be discussed further in Chapter 6.

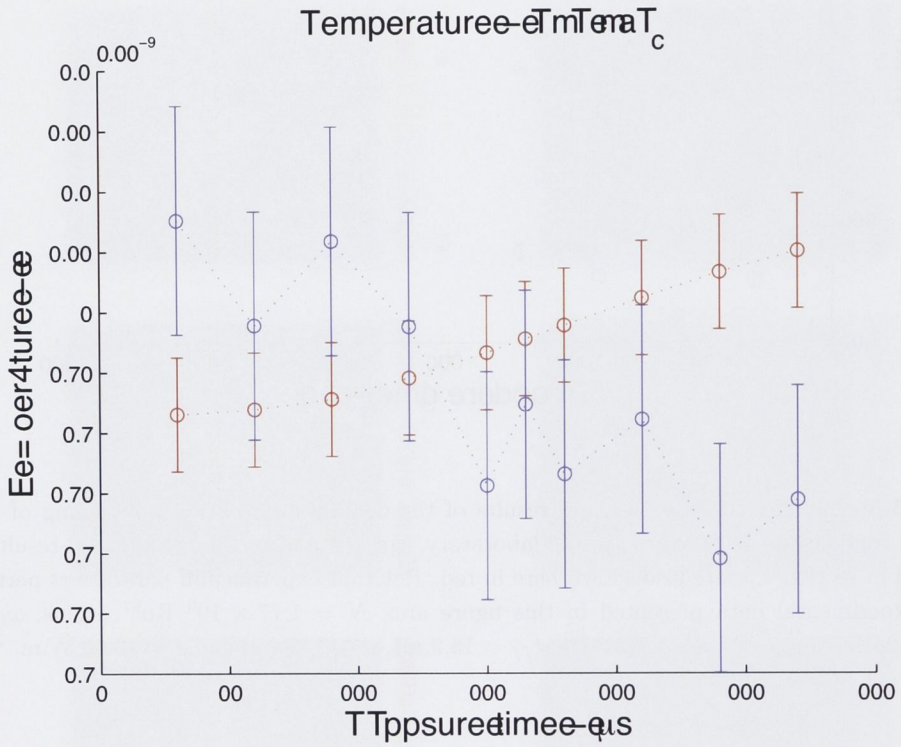

Figure 5.4: In blue, the experimentally measured temperature of the $T = 0.94 \times T_c$ condensate, where T is determined from the average, measured values of the condensed/thermal fractions. Shown in red are the theoretical predictions of measured temperature stated previously in section 4.3. The relevant experimental parameters concerning the above data are: $N = 1.77 \times 10^6$ Rb^{87} atoms, $\omega_{tight} = 2 \times \pi \times 128$ Hz, $\omega_{weak} = 2 \times \pi \times 12.8$ Hz, $t_{ff} = 16.9$ ms, $a = 5.77$ nm and $I = 16.69$ $W.m^{-2}$.

5.3 Temperature measurement of a zero temperature condensate

Images of a condensate close to zero temperature were obtained in the laboratory for a variety of exposure times ranging between 30 μs and 270 μs, and are shown in figure 5.5. It can be seen clearly that some form of 'blurring' beyond the expected, and relatively slight, effect of ballistic expansion is evident in the data.

With the exception of the number of condensate atoms, the experimental parameters are the same for the zero temperature case as they are for the $T = 0.94 \times T_c$, namely: $\omega_{tight} = 2 \times \pi \times 128$ Hz, $\omega_{weak} = 2 \times \pi \times 12.8$ Hz, $t_{ff} = 16.9$ ms, $a = 5.77$ nm and $I = 16.69$ W.m^{-2}. The number of Rb^{87} atoms in this case is $N = 5.65 \times 10^5$.

In reality, the condensate being measured in this case is not actually at zero temperature. It is impossible to ensure *all* atoms in the system are in the ground state of the trap after cooling; a single, trapped atom in some mode other than the ground state would yield a system at non-zero temperature! Further, it is impossible to verify the presence of thermal fractions of a small enough size due to the signal to noise limitations inherent of any experimental setup. With these considerations in mind, the atomic samples imaged for the present study are close enough to 'zero temperature' that a parabolic function alone can be used for fitting the imaged distributions of all exposure times.

The width of the parabolic fitting function was measured for the relevant exposure times ranging from 30 μs to 270 μs, as per the definition of width given in section 4.1. The results are displayed in figure 5.6, where the error bars were generated using the 95% confidence intervals.

The experimental data for the density distribution of the 'zero temperature' condensate shows that its width does indeed broaden at a rate faster than can be expected from ballistic expansion alone. This implies that scattering-induced atomic motion does impact the real distribution, with two interesting consequences. Firstly, like the theoretical result for the broadening of a zero temperature condensate with the random-walk effect off (presented in section 4.2), a real condensate appears to retain its parabolic shape throughout the imaging process, implying that no atoms were ever occupying the thermal fraction. Consequently, no error in the measurement of temperature is made. Secondly, the way a real, 'zero temperature' condensate broadens due to scattering-induced atomic motion is *not* quadratic as in the case of the theoretical model with random walking on (also shown in figure 5.6 for comparison to the experimental data); the width of the distribution tends to increase in a linear fashion. These results, as well as those presented in section 5.2, are discussed further in Chapter 6.

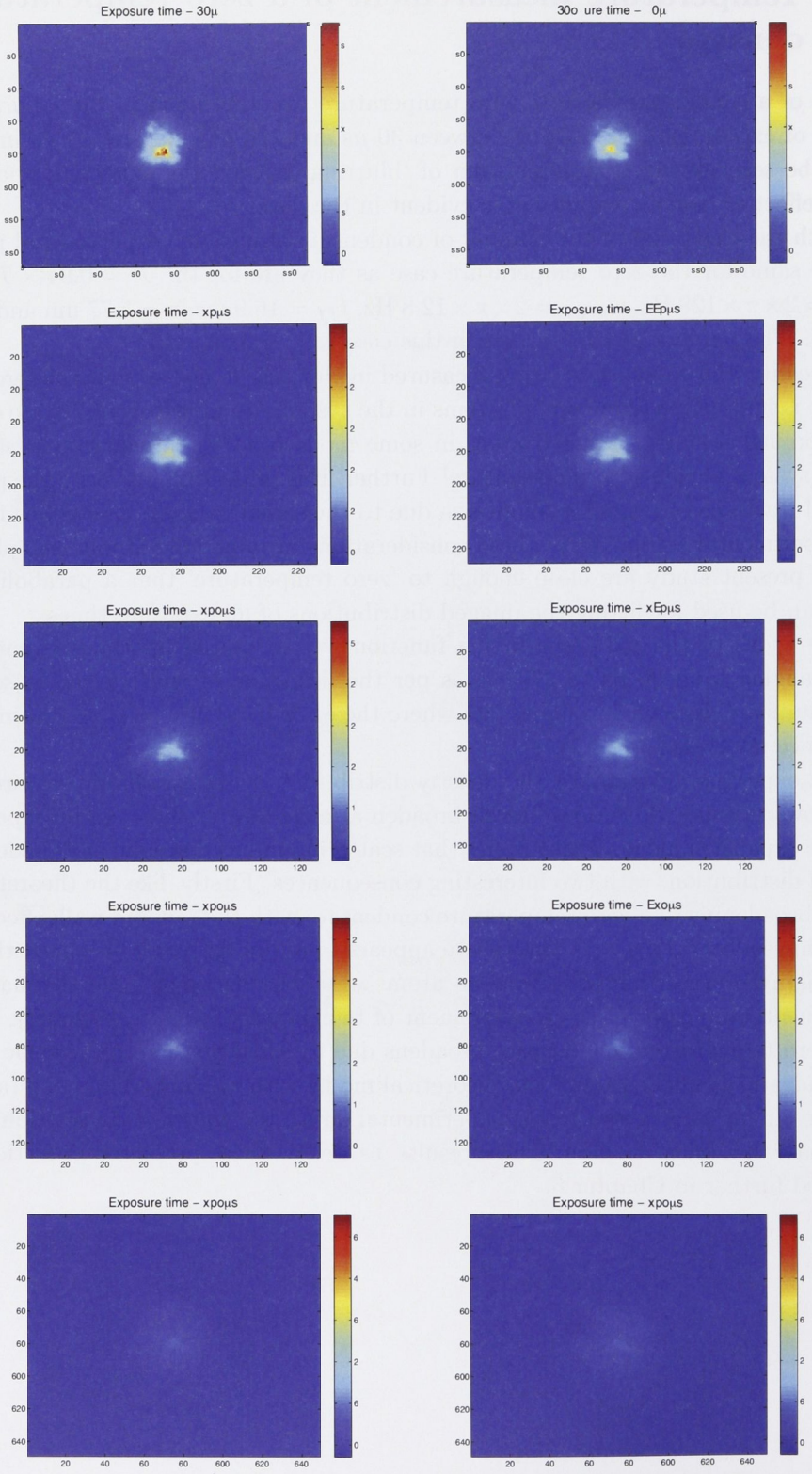

Figure 5.5: Raw experimental images of a pure condensate expanding as exposure times increases. The false colour scale indicates optical depth while the x and y axes represent pixel numbers associated with the imaging camera.

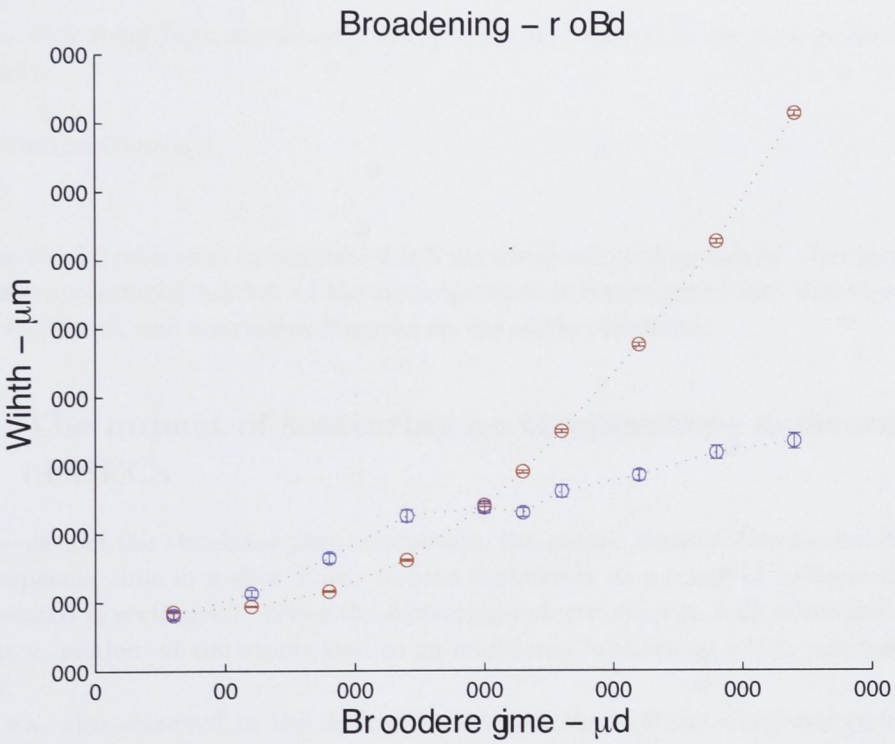

Figure 5.6: In blue, the experimental results of the density distribution broadening of a T≈0 K condensate produced in the laboratory. Theoretical predictions of this behaviour, first presented in section 4.2, are shown in red. Relevant experimental parameters pertaining to the experimental data presented in this figure are: $N = 5.65 \times 10^5$ Rb^{87} atoms, $\omega_{tight} = 2 \times \pi \times 128$ Hz, $\omega_{weak} = 2 \times \pi \times 12.8$ Hz, $t_{ff} = 16.9$ ms, $a = 5.77$ nm and $I = 16.69$ W.m^{-2}.

Chapter 6

Discussion and conclusive remarks

"I pass with relief from the tossing sea of cause and theory to the firm ground of result and fact"

- Winston Churchill

The results presented in chapters 4 & 5 are discussed in this chapter. The implications of scattering-induced motion of the measurement of temperature and other parameters are investigated, and conclusive remarks on the study presented.

6.1 The impact of scattering on temperature measurements of BECs

For the case of the *simulated* pure condensate, the atomic density distribution broadened with exposure time in a slow, linear fashion exclusively as a result of ballistic expansion, as presented in section 4.2. When the scattering-induced random walk effect was included, the extra 'motion' of the atoms lead to an additional broadening which was quadratic in nature.

It was also observed in the data of section 4.2 that for the simulated pure condensate, a parabolic fitting function could be used to fit data without the random walk effect present, as the atomic density distribution retained its parabolic form regardless of exposure time. However, with the inclusion of the random walk effect, the distribution was no longer parabolic such that a standard fitting function, which has both parabolic (for the condensate) and gaussian (for a thermal fraction) components, was necessary to fit accurately. Consequently, the fitting included a gaussian component as if a thermal fraction was present. This resulted in a false temperature measurement which grew increasingly inaccurate with exposure time until converging on the critical temperature T_c.

For the case of the $T = 0.94 \times T_c$ condensate presented in section 4.3, the simulation suggests that, in the absence of the random walk effect, the atomic density distribution should increase in a slow linear fashion as a result of ballistic expansion. When the random walk effect is included, the simulation predicts that the distribution should increase with exposure time in an approximately quadratic fashion.

When the random walk effect is not present in this case, temperature measurements are consistent for all exposure times. However, when the random walk effect is included, the distribution changes increasingly with exposure time in such away that the thermal fraction is measured as getting larger relative to the condensate fraction. This is similar to

the simulated case of the pure condensate, although as a thermal fraction already exists for the mixture, the effect is significantly less dramatic; the temperature appears to increase approximately in a linear fashion, but only over a range of around 14 nK (as compared to around 221 nK in the pure condensate case). In other words, the simulation model predicts that in this temperature regime, we should expect to see a quadratic broadening of the atomic density distribution, and this should result in the temperatures being measured as increasingly 'warm' with exposure time.

For both temperature regimes discussed above, the empirical data presented in chapter 5 does not match the simulated cases where the random walk effect *isn't* present, suggesting that there may in fact be measurable atomic motion present in the experimental data. Further, in the case of the $T = 0.94 \times T_c$ system, the simulated and experimental data exhibit very similar broadening trends, suggesting that not only may atomic motion be present and measurable, but also that it behaves statistically similar to the expectations of the simulation.

For the zero-temperature condensate case, the empirical data also shows broadening as a result of atomic motion. However, while the broadening is evident in the data, it does not exhibit the same broadening trend as in the $T = 0.94 \times T_c$ case; the broadening is linear instead of the approximately quadratic broadening trend predicted by the simulation.

While broadening is observed in both temperature regimes, simulated expectations of the functional form with which the broadening occurs are well correlated with empirical data in the $T = 0.94 \times T_c$ case, but less so in the $T = 0$ K case. To understand this behaviour, it is natural to contemplate any limits and assumptions inherent of the numerical model used in the present study and whether they lead to the observed discrepancy in the $T = 0$ K case.

Of the assumptions and limitations of the numerical model stated in chapter 3, there is one assumption that can directly affect atomic motion and may offer an explanation for the aforementioned discrepancy between the simulated and theoretical data taken in the $T = 0$ regime. This assumption is that, in the numerical model, no atomic motion will result from the absorption of photons re-emitted from atoms scattering light from the imaging laser, as discussed in section 3.3. It was also stated that in the optically thin regime, this assumption is valid as the likelihood of absorbing such a photon is small. However, as the atomic density approaches that of an optically thick system, the validity of this assumption breaks down as the likelihood of absorbing such a photon increases. As the width of the system under study in the $T = 0.94 \times T_c$ regime is measured from the gaussian thermal fraction, the optical depth of the measured component of the system is relatively low. However, in the $T = 0$ K regime, the width is measured from the parabolic form of the condensed system which, with a relatively high optical depth, is less likely to exhibit behaviour consistent with this assumption. Therefore, if this assumption was to break down in any regime, it would be that of the $T = 0$ K case, which may be indicated in the data.

The central question of the present study is to see whether atomic motion produced by the BEC imaging process used in the study affects the temperature measurement of the BEC. For the $T = 0$ K system, the numerical model predicted that atomic motion caused by the imaging process would blur the image to give the false impression that a thermal fraction was present. Further, the model predicted that this false thermal fraction would lead to a dramatic error in the measured temperature. However, while atomic motion and density profile broadening was observed in the empirical data, no error in temperature measurement was observed as the system retained it's parabolic form throughout the

imaging process (and thus, without a false thermal fraction present, was consistently measured at T = 0 K). Atomic motion produced by the scattering of imaging photons did not impact the measurement of temperature in the $T = 0$ K system.

For the $T = 0.94 \times T_c$, the numerical model predicted that a slight and gradual increase in temperature measurement would occur as atomic motion would give the false impression that the thermal fraction becomes slightly larger while the condensate fraction becomes slightly smaller. The empirical data suggests this does not occur and, while the trend is weak and noisy, the measured temperature tends to slightly decrease with exposure time. In the empirical measurements, the thermal fraction tends to broaden quicker and, consequently, becomes harder to fit to as the signal-to-noise ratio for the thermal fraction decreases at a rate faster than it does for the condensate fraction. It's a small effect, but it accounts for the slight decrease in the temperature of the system as the exposure time increases. It also accounts for why this decreasing trend is itself so noisy. Atomic motion produced by the scattering of imaging photons did impact the measurement of temperature in the atomic motion produced by the scattering of imaging photons did not impact the measurement of temperature in the $T = 0$ K system, although the effect is small and within acceptable error limits; the variance of the measured temperatures over all exposure times is small compared to the mean temperature measured.

6.2 The measurement of parameters other than temperature

One unexpected insight gained in the present study, which has not yet been discussed, is the way scattering-induced broadening has impacted parameters other than temperature. Although the atomic samples studied in the lab did broaden significantly as a result of being imaged, it was the lack of *change* in distribution *shape* which resulted in little change of measured temperature. But the widths of the distributions did change significantly and, as discussed in section 1.4.2, the trap frequencies used in the experiment are related to the widths of the distributions.

For an example of how trap frequencies will change with the widths of atomic distributions, consider the gaussian-shaped thermal fraction, given by

$$\begin{aligned} n_{therm}(\mathbf{r}) &= \frac{1}{\lambda_{dB}^3} g_{3/2}(z(\mathbf{r})) \\ &\approx \frac{1}{\lambda_{dB}^3} z(\mathbf{r}) \\ &= \frac{1}{\lambda_{dB}^3} \exp\left(\frac{\mu - V(\mathbf{r})}{k_B T}\right), \end{aligned} \tag{6.1}$$

where the harmonic potential $V(\mathbf{r})$, characterised by trap frequencies, determines the *width* of the gaussian-shaped thermal fraction. For the sake of simplicity, analysis of the way broadening impacts trap frequencies will be done in one dimension. The thermal distribution in one dimension is given by

$$n_{therm}(\mathbf{r}) = \frac{1}{\lambda_{dB}^3} \exp\left(\frac{\mu - \frac{1}{2} m \omega_x^2 x^2}{k_B T}\right), \tag{6.2}$$

and the chemical potential μ in one dimension is given by

$$\mu = \frac{m\omega_x^2}{2}\left(\frac{3NU}{2m\omega_x^2}\right)^{2/3}, \tag{6.3}$$

where N is the atom number and U is the scattering length. The full-width at half-maximum W_{FWHM} can be used to define the width of the thermal distribution, and is given by

$$W_{FWHM} = 2\left[\frac{k_B T \ln(2/n_{max}) + \mu}{m\omega_x^2}\right]^{1/2}, \tag{6.4}$$

where n_{max} is the maximum value of $n_{therm}(\mathbf{r})$. Transposing for ω_x, we see the trapping frequency is given

$$\omega_x = \left[\frac{4}{mW_{FWHM}^2}\left(k_B T \ln(2/n_{max}) + \mu\right)\right]^{1/2}. \tag{6.5}$$

With expression 6.5, we can plot the way in which the trapping frequency changes as the measured width W_{FWHM} of a condensate and thermal fraction mixture changes, as shown in figure 6.1. Recall that the plot of how the the measured width changes with exposure time is shown in figure 5.3 of section 5.2.

As with the measurement of temperature, figure 6.1 shows the change in measured trap frequency, as a result of scattering-induced broadening, is also relatively small. The value of trap frequency measured at the shortest exposure time of 30 μs is the most accurate; the values become progressively less accurate as exposure time increases. The maximum difference between measured trap frequencies is 4.5 Hz, which corresponds to 3.5% of the maximum value. For all but the largest of exposure times used in the present study, the error is therefore smaller than 3.5%, suggesting that the affect of scattering-induced broadening on the measurement of trap frequency is not a huge factor. The truth of this statement is really a matter of how this source of error compares with other sources of error pertaining to trap frequency; if they are comparable or larger, than the statement is likely true. A detailed discussion of the possible sources of error relating to trap frequency is beyond the scope of this study. At any rate, any significant error in the measurement of trap frequency due to scattering-induced broadening can be minimised by ensuring exposure times are kept small for these measurements.

6.3 Conclusive remarks

To the knowledge of the author, the work presented in the present study is the first study into the impact of scattering-induced atomic motion in the process of imaging a BEC. Atomic motion was observed in both temperature regimes studied and good, qualitative agreement was found between the numerical and empirical data in the $T = 0.94 \times T_c$ case. In the $T = 0$ K case, where the optical depth of the measured system was relatively greater compared to the $T = 0.94 \times T_c$ case, there was less agreement between numerical and empirical data. Assumptions inherent of the numerical model currently limit its use in the optical thick regime where the effect of atomic motion due to the absorption of re-emitted imaging photons becomes important.

While it was demonstrated the impact of atomic motion on the measurement of temperature was not critical, the fact that atomic motion is clearly present opens the door to

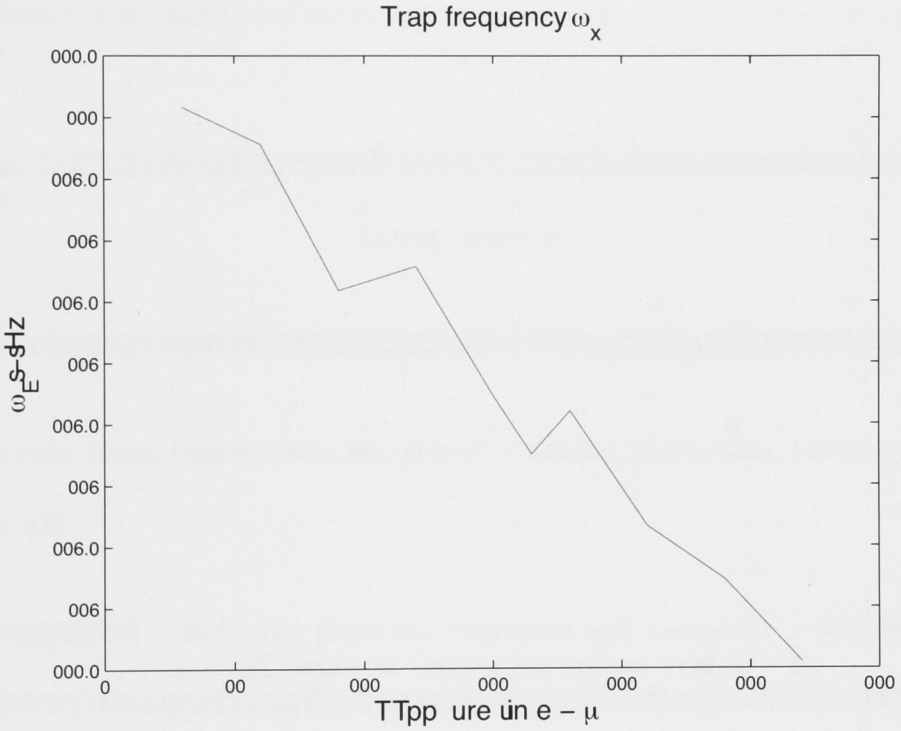

Figure 6.1: Measuring the trap frequency of a T $= 0.94 \times T_c$ condensate as the system's width changes with exposure time. Relevant experimental parameters pertaining to the experimental data presented in this figure are: $N = 1.77 \times 10^6$ Rb^{87} atoms, $\omega_{weak} = 2 \times \pi \times 12.8$ Hz, $t_{ff} = 16.9$ ms, $a = 5.77$ nm and $I = 16.69$ W.m^{-2}.

further questions about the role this effect plays in BEC measurements and experiments in general. For prospective experiments conducted in the optically thin regime, the model used in the present study offers a useful theoretical tool for the study of some experimental or BEC parameters. For prospective experiments in the optically thick regime, the model used in the present study could be modified to be a useful analytical tool in the optically thick regime. Further exploration of the role played by the atomic motion under study here should yield a greater confidence in interpreting data obtained in future BEC experiments conducted in the same or similar regimes.

Numerical model code

The *Matlab* code constituting the numerical model used in the present study is displayed below.

```
%%%%%%%%%%%%%%%%%%%%%%%%%%%%%%%%%%%%%%%%%%%%%%%%%%%%%%%%%%%%%%%%%%%%%%%%%%%%%%%%
%   %
%                                theory_model.m                                  %
%                                                                                %
%                                                                                %
%%%%%%%%%%%%%%%%%%%%%%%%%%%%%%%%%%%%%%%%%%%%%%%%%%%%%%%%%%%%%%%%%%%%%%%%%%%%%%%%


%function [mean_temperature,max_error] = theory_model(time_increment)
tic
clear all


%%%%%%%%%%%%% - Defining physical constants and variables - %%%%%%%%%%%%%
%                 % - All units SI unless otherwise stated - %                 %
%%%%%%%%%%%%%%%%%%%%%%%%%%%%%%%%%%%%%%%%%%%%%%%%%%%%%%%%%%%%%%%%%%%%%%%%%%%%%%%%

% - Fundamental constants - %

Hbar = 1.0546e-34;
H = 6.626e-34;
c = 2.99e8;

% - Optics - %

a = 50e-3; % Nominal distance between particle and lens
M = 2.4;  % Magnification
D = 50.8e-3; % Lens diameter

% - Trap - %

% Trapping frequenices, x, y, z
omegax = 2*pi*12.8;
```

```
omegay = 2*pi*128;
omegaz = 2*pi*128;


R = 6.3e-6;  % Thomas-Fermi radius

% - Atoms - %

% Number of atoms in BEC
N = 5.6540e+05;  % mean number for therm = 1.7710e+06, for pure = 5.6540e+05
mass = 1.443e-25;
scat_length = 5.77e-9;
mu = 0.5*(15*scat_length*Hbar^2*sqrt(mass)*omegax*omegay*omegaz*N)^(2/5);
mu_1d = ((mass*omegay^2)/2)*((3*N*scat_length)/(2*mass*omegay^2))^(2/3);
kB = 1.381e-23;
temp_c = 0.90*Hbar*N^(1/3)*(1/kB)*(omegax*omegay*omegaz)^(1/3)
temp_fraction = 0.9397;
temp = temp_fraction*temp_c;

kt = kB*temp;
lambda_dB = sqrt((2*pi*Hbar^2)/(mass*kt));
non_lin_term = (4*pi*scat_length*Hbar^2)/mass;
kinetic_energy = mu + non_lin_term;
atom_velocity = sqrt((2*kinetic_energy)/mass);

% - Detector - %

detector_eff = 0.45;
pixel_width = 9.0e-6;
pixel_area = (pixel_width)^2;
well_depth = 120e+3;

% - Imaging Laser - %

fftime = 16.9e-3;
time_iterations = 10;
time_increment = 3e-6;
exposure_time = 0;
total_exposure_time = time_iterations * time_increment

% - Universal Imaging Parameters - %

grid_dimension = 200;
x_min = -(grid_dimension/2)*pixel_width;
x_max = (grid_dimension/2)*pixel_width;
y_min = x_min;
y_max =  x_max;
z_min = x_min;
```

```
z_max = x_max;

x = linspace(x_min, x_max, grid_dimension+1);
y = linspace(y_min, y_max, grid_dimension+1);
z = linspace(z_min, z_max, grid_dimension+1);
BEC = zeros(grid_dimension,grid_dimension,grid_dimension);

% - 't' loop preallocation of variables - %

std_r_2_list = zeros(1:length(time_iterations));
mean_r_2_list = zeros(1:length(time_iterations));
max_r_2_list = zeros(1:length(time_iterations));
G2D_list = zeros(length(y),length(z),length(time_iterations));

for t = 1:1:time_iterations

exposure_time = exposure_time + time_increment;
lambda = 780e-9;
freq = 2.99e8/lambda;
ang_freq = 2*pi*(freq);
k = (2*pi)/lambda;
p = Hbar*k;
Gamma = 2*pi*6e6;
Isat = 16.69;
I = 1*16.69;
photon_energy = H*c*(1/lambda);
det = 0;


% - Cross sections/Scattering rates - %

sigma_0 = (3*lambda^2)/(2*pi);
sigma = sigma_0/(1+(I/Isat)+(2*det/Gamma)^2);
t_scat = 26.24e-9;
abs_rate = (I/(Hbar*ang_freq))*sigma;
t_abs = (Hbar*ang_freq)/(I*sigma_0) + (Hbar*ang_freq)/(Isat*sigma_0)...
+ ((Hbar*ang_freq)/(I*sigma_0)*((2*det)/Gamma)^2) - t_scat;
ppp_max = (I*exposure_time*pixel_area*detector_eff*(1/photon_energy))/M^2;
I_min = (M^2*841) / (exposure_time*pixel_area*detector_eff*(1/photon_energy));
new_OD = log(I/I_min);
shot_noise_ppp_max = sqrt(ppp_max);
scate_rate = 1/(t_scat+t_abs);


% - Numerics - %

num_particles = 1500;%1500;
excited_times = zeros(1, num_particles);
```

```
ground_times = zeros(1, num_particles);
P = zeros(1, num_particles);
norm_r_list = zeros(1, num_particles);
r_1_list = zeros(1, num_particles);
r_2_list = zeros(1, num_particles);
r_3_list = zeros(1, num_particles);
p_1_list = zeros(1, num_particles);
p_2_list = zeros(1, num_particles);
p_3_list = zeros(1, num_particles);
COUNTS = zeros(1, num_particles);


%%%%%%%%%%%%%%%%%%%%%%%% - Random walk code - %%%%%%%%%%%%%%%%%%%%%%%%
%                    Including statistical output code                 %
%%%%%%%%%%%%%%%%%%%%%%%%%%%%%%%%%%%%%%%%%%%%%%%%%%%%%%%%%%%%%%%%%%%%%%

    for m = 1:1:num_particles

        p_hat = [0,0,0];
        r = [0,0,0];

        counter = 0;
        total_time = 0;
        total_abs_time = 0;
        total_scat_time = 0;

            while (total_time < exposure_time)

            counter = counter + 1;

            t_scat_rand = -log(rand(1))*t_scat;
            t_abs_rand = -log(rand(1))*t_abs;
            total_time = total_time + t_scat_rand + t_abs_rand;

            total_scat_time = total_scat_time + t_scat_rand;
            total_abs_time = total_abs_time + t_abs_rand;

            p_hat(1) = p_hat(1)+1;
            r = r + p_hat*p*(1/mass)*t_scat_rand;

            phi = 2*pi*rand(1);
            theta = acos(rand(1)*2 -1);
            x = sin(theta)*cos(phi);
            y = sin(theta)*sin(phi);
            z = cos(theta);
            p_hat(1) = p_hat(1)+x;
            p_hat(2) = p_hat(2)+y;
            p_hat(3) = p_hat(3)+z;
```

```
            r = r + p_hat*p*(1/mass)*t_abs_rand;

            end

        norm_r_list(m) = norm(r);

        r_1_list(m) = r(1);
        r_2_list(m) = r(2);
        r_3_list(m) = r(3);

     COUNTS(m) = counter;

    end

std_of_norm_r = M*std(norm_r_list, 1);
variance_of_norm_r = M*var(norm_r_list, 1);

numerical_variance_r_1 = M*var(r_1_list, 1);
numerical_std_r_1 = M*std(r_1_list);
mean_r_1 = mean(r_1_list);
max_r_1 = max(r_1_list);

numerical_variance_r_2 = M*var(r_2_list, 1);
numerical_std_r_2 = M*std(r_2_list);
std_r_2_list(t) = M*std(r_2_list);
mean_r_2 = mean(r_2_list);
mean_r_2_list(t) = mean(r_2_list);
max_r_2 = max(r_2_list);
max_r_2_list(t) = max(r_2_list);

numerical_variance_r_3  = M*var(r_3_list, 1);
numerical_std_r_3 = M*std(r_3_list);
mean_r_3 = mean(r_3_list);
max_r_3 = max(r_3_list);


%%%%%%%%%%%%%%%%%%%%%% - Image generation  - %%%%%%%%%%%%%%%%%%%%%%%%%%
%       Gaussian, Thomas-Fermi, Background and P-Funktion images.       %
%%%%%%%%%%%%%%%%%%%%%%%%%%%%%%%%%%%%%%%%%%%%%%%%%%%%%%%%%%%%%%%%%%%%%%%

x = linspace(x_min, x_max, grid_dimension+1);
y = linspace(y_min, y_max, grid_dimension+1);
z = linspace(z_min, z_max, grid_dimension+1);

% - Image of random walk distribution - %

G = zeros(length(y),length(z),length(x));
```

```
    for j = 1:length(y);
        for k = 1:length(z);
          for i = 1:length(x);
                G(j,k,i) = (1/((numerical_std_r_1*numerical_std_r_2*numerical_std_r_3)...
                *sqrt(2*pi)^3))* exp( -( (x(i)/M)^2/(2*numerical_std_r_1^2) )...
                 -( (y(j)/M)^2/(2*numerical_std_r_2^2) )...
                  -( (z(k)/M)^2/(2*numerical_std_r_3^2) ) );
           end
        end
    end
    G2D = trapz(G,3);
    G2D_list(:,:,t) = G2D;

end

G2D_list_img = sum(G2D_list,3);

% - Thermal fraction distribution - %

Nth = N - ( N*(1 - (temp/temp_c)^3) );

std_dev_th_x = M*sqrt( ((kB*temp)/mass)*((1+(omegax^2*(fftime + exposure_time)^2))/omegax^2)
std_dev_th_y = M*sqrt( ((kB*temp)/mass)*((1+(omegay^2*(fftime + exposure_time)^2))/omegay^2)
std_dev_th_z = M*sqrt( ((kB*temp)/mass)*((1+(omegaz^2*(fftime + exposure_time)^2))/omegaz^2)

Gth = zeros(length(y),length(z),length(x));

for j = 1:length(y);
  for k = 1:length(z);
        for i = 1:length(x)
         Gth(j,k,i) = ( Nth/(std_dev_th_x*std_dev_th_y*std_dev_th_z*sqrt(2*pi)^3) )...
               * exp( -( x(i)^2/(2*std_dev_th_x^2) ) -( y(j)^2/(2*std_dev_th_y^2) )...
               -( z(k)^2/(2*std_dev_th_z^2) ) );
        end
    end
end

Gth_raw = trapz(x,Gth,3);
Gth_poly_resize = (Gth/max(max(max(Gth))))*0.1;
polylog_terms = 5;
Gth_poly_list = zeros(length(y),length(z),length(x));

for j = 1:length(y);
  for k = 1:length(z);
        for i = 1:length(x)
            Gth_poly_terms = zeros(1:length(polylog_terms));
            for l = 1:polylog_terms
                Gth_poly_terms(l) = (Gth_poly_resize(j,k,i)^l)/(l^(3/2));
```

```
            end
            Gth_poly = sum(Gth_poly_terms);
            Gth_poly_list(j,k,i) = Gth_poly;
        end
    end
end

Gth_poly2D = trapz(x,Gth_poly_list,3);
Gth_const = Nth/(trapz(y,trapz(z,Gth_poly2D)));
Gth_norm = Gth_const*Gth_poly2D;
integral_over_Gth_norm = trapz(y,trapz(z,Gth_norm));

max_Gth_raw = max(max(Gth_raw));
max_Gth_norm = max(max(Gth_norm));

%%% - Normalised thermal cloud absorption image

% - Thomas-Fermi Image Generation - %

scale_term_x = M*(1 + ( (omegax/omegaz)^2 * ( (omegaz*(fftime+exposure_time)...
*atan(omegaz*(fftime+exposure_time)))...
 - log(sqrt(1+(omegaz*(fftime+exposure_time))^2)) ) ));
scale_term_y = M*sqrt(1+(omegay*(fftime+exposure_time))^2);
scale_term_z = M*sqrt(1+(omegaz*(fftime+exposure_time))^2);

for j = 1:length(y);
  for k = 1:length(z);
        for i = 1:length(x)
            TF = (mu -((mass/2)*(((x(i)/scale_term_x)^2*omegax^2)...
             + ((y(j)/scale_term_y)^2*omegay^2)...
              + ((z(k)/scale_term_z)^2*omegaz^2))))/...
              (scale_term_x*scale_term_y*scale_term_z*non_lin_term);
                if TF < 0
                TF = 0;
                end
            BEC(j,k,i) = (1 - (Nth/N))*TF;
        end
    end
end

%%% - Normalised Thomas-Fermi absorption image

BEC2D_img = trapz(x,BEC,3);
integral_BEC2D_img = trapz(y,trapz(z,BEC2D_img));
BEC2D = trapz(x,BEC,3);
Ntf = N - Nth;
integral_over_BEC_volume = trapz(y,trapz(z,trapz(x,BEC)));
BEC2D = squeeze(BEC2D);
```

```
Gth_norm = squeeze(Gth_norm);
BEC_total2D = BEC2D + Gth_norm;

integral_over_BEC_total2D = trapz(x,trapz(y,trapz(z,BEC)));

BEC_abs_img_clean = ppp_max*exp(-sigma*BEC_total2D);
BEC_abs_img_clean = ( 0.5*((BEC_abs_img_clean - well_depth)...
 - abs(BEC_abs_img_clean - well_depth)) ) + well_depth;
BEC_img_add_noise = paulnoise((BEC_abs_img_clean/1e+12),'poisson');
BEC_abs_img = BEC_img_add_noise*1e+12;

integral_addition = integral_over_Gth_norm + integral_over_BEC_volume;

bgrnd_clean = ones(length(BEC2D),length(BEC2D))*ppp_max;
bgrnd_clean = ( 0.5*((bgrnd_clean - well_depth) - abs(bgrnd_clean...
 - well_depth)) ) + well_depth;
bgrnd_noise = paulnoise((bgrnd_clean/1e+12),'poisson');
bgrnd = bgrnd_noise*1e+12;

max_counts = max(max(bgrnd));

%%% - BEC absorption image

%img_one_term_1 = log(bgrnd_clean); % with NO noise
%img_one_term_2 = log(BEC_abs_img_clean); % with NO noise
img_one_term_1 = log(bgrnd); % with noise
img_one_term_2 = log(BEC_abs_img); % with noise
    for i = 1:size(img_one_term_2,1)
        for j = 1:size(img_one_term_2,1)
            if abs(img_one_term_2(i,j)) == Inf
                img_one_term_2(i,j) = 0;
            end
        end
    end

image_one = img_one_term_1 - img_one_term_2;

% figure(34), imagesc(image_one)
% title('BEC - 5\mus exposure time','fontsize',15)

% figure(33)
% surf(image_one)
% title('BEC distribution - T = 0.9 T_c','fontsize',15)
% shading interp,view(45,25);

%figure(333),plot(y,image_one((grid_dimension/2),:)),title('BEC: x-axis')

% figure(3332)
```

```
% plot(x,image_one(:,(grid_dimension/2)))
% title('Cross section - with random walk','fontsize',15)
% xlabel('Distribution width - m','fontsize',15)
% ylabel('Optical depth - dimensionless','fontsize',15)

% - P-Funktion Distribution - %

G2D_list_img = squeeze(G2D_list_img);
P_raw = conv2(BEC_total2D,G2D_list_img,'same');
P_max = max(max(P_raw));
P_norm = P_raw/P_max;
P_const = sum(sum(BEC_total2D))/sum(sum(P_norm));
P_N = P_const * P_norm;
integral_over_P_volume = pixel_width^2*sum(sum(P_N));
P_abs_img_clean = ppp_max*exp(-sigma*P_N);
P_img_add_noise = paulnoise((P_abs_img_clean/1e+12),'poisson');
P_abs_img = P_img_add_noise*1e+12;
P_abs_img = ( 0.5*((P_abs_img - well_depth) - abs(P_abs_img - well_depth)) )...
 + well_depth;

%%% - P-Function absorption image

%image_two = log(bgrnd_clean) - log(P_abs_img_clean); % with NO noise
image_two = log(bgrnd) - log(P_abs_img); % with noise

%figure(42), imagesc(image_two),title('P-Funktion')
%figure(44), surf(image_two),title('P-Funktion'),shading interp;

figure(444)
plot(y,image_two((grid_dimension/2),:))
title('Cross section - with random walk','fontsize',15)
xlabel('Distribution width - m','fontsize',15)
ylabel('Optical depth - dimensionless','fontsize',15)

toc
return

%%%%%%%%%%%%%%%%%%%%%%%%%%%%%%%%%%%%%%%%%%%%%%%%%%%%%%%%%%%%%%%%%%%%%%%
%%%%%%%%%%%%%%% passing to theory_fit %%%%%%%%%%%%%%%%
%%%%%%%%%%%%%%%%%%%%%%%%%%%%%%%%%%%%%%%%%%%%%%%%%%%%%%%%%%%%%%%%%%%%%%%

% [avg_temp,largest_error] = theory_fit(temp_c,grid_dimension,image_two);
% mean_temperature = avg_temp;
% max_error = largest_error;

% - Difference between TF & P-Function Distributions (with noise) - %

difference_img = image_one - image_two;
```

```
diff_img_squared = difference_img.^2;
diff_squared_number = trapz(y,trapz(z,diff_img_squared));

%figure(555),plot( y,Gth_norm((grid_dimension/2),:),...
 y,BEC2D_img((grid_dimension/2),:) , y,BEC_total2D((grid_dimension/2),:) ),...
 title('Polylog + TF: x-axis')

%%% - Difference between OD images of TF & P Functions
    %figure(5), imagesc(difference_img),title('Difference - 160');
    %figure(55), imagesc(diff_img_squared),title('Difference squared');
    %figure(55), surf(difference_img),title('Difference'),shading interp;

    %figure(6), imagesc(diff_img_squared),title('Difference squared - 160');
    %diff_image_2 = A - image_two;
    %figure(6), imagesc(diff_image_2),title('Difference between lab image and P-Fn');
    %max_difference_img = max(max(difference_img))
    %min_difference_img = min(min(difference_img))

toc
return
```

Bibliography

[1] M. H. Anderson, J. R. Ensher, M. R. Matthews, C. E. Wieman, and E. A. Cornell. Observation of bose-einstein condensation in a dilute atomic vapor. *Science*, 269(5221):198 – 201, 1995.

[2] V. Bagnato, D. E. Pritchard, and D. Kleppner. Bose-einstein condensation in an external potential. *Phys. Rev. A*, 1987.

[3] G. Baym and C. J. Pethick. Ground-state properties of magnetically trapped bose-condensed rubidium gas. *Phys. Rev. Lett.*, 1996.

[4] J. A. Beattie. *Temperature, its Measurement and Control in Science & Industry*, volume 1. Reinhold, 1941.

[5] R. P. Benedict. *Essentials of Thermodynamics*. Electro-Technol., 1962.

[6] R. P. Benedict. *Fundamentals of temperature, pressure, and flow measurements*. John Wiley & Sons, Inc., 3rd edition, 1984.

[7] T. H. Benzinger, editor. *Temperature - Arts and Concepts*, volume 1. Dowden, Hutchinson & Ross, Inc., 1977.

[8] M. Boas. *Mathematical Methods in the Physical Sciences*. Wiley, 2nd edition, 1983.

[9] H. C. Bolton. *Evolution of the Thermometer*. Chem. Pub. Co., 1900.

[10] S. N. Bose. Plancks gesetz und lichtquantenhypothese. *Zeitschrift für Physik*, 26:178–181, 1924.

[11] C. C. Bradley, C. A. Sackett, J. J. Tollett, and R. G. Hulet. Evidence of bose-einstein condensation in an atomic gas with attractive interactions. *Phys. Rev. Lett.*, 75:1687 – 1690, 1995.

[12] S. Carnot. *Reflections on the Motive Power of Fire*. Dover, 1960.

[13] S. Chu, L. Hollberg, J. E. Bjorkholm, A. Cable, and A. Ashkin. Three-dimensional viscous confinement and cooling of atoms by resonance radiation pressure. *Phys. Rev. Lett.*, 55:48–51, 1985.

[14] F. Dalfovo, S. Giorgini, L. P. Pitaevskii, and S. Stringari. Theory of bose-einstein condensation in trapped gases. *Rev. Mod. Phys.*, 71(3):463, 1999.

[15] K. B. Davis, M. O. Mewes, M. R. Andrews, N. J. van Druten, D. S. Durfee, D. M. Kurn, and W. Ketterle. Bose-einstein condensation in a gas of sodium atoms. *Phys. Rev. Lett.*, 75(3969 - 3973), 1995.

[16] M. Edwards and K. Burnett. Numerical solution of the nonlinear schrödinger equation for small samples of trapped neutral atoms. *Phys. Rev. A*, 1995.

[17] A. Einstein. Quantum theory of mono-atomic ideal gas. second paper. *SITZUNGSBERICHTE DER PREUSSICHEN AKADEMIE DER WISSENSCHAFTEN PHYSIKALISCH-MATHEMATISCHE KLASSE 3*, 1925.

[18] R. P. Feynman. Atomic theory of liquid helium near absolute zero. *Phys. Rev.*, 91(6), 1953.

[19] C. J. Foot. *Atomic Physics.* Oxford, 2005.

[20] V. V. Goldman, I. F. Silvera, and A. J. Leggett. Atomic hydrogen in an inhomogeneous magnetic field: Density profile and bose-einstein condensation. *Phys. Rev. B*, 1981.

[21] D. J. Griffiths. *Introduction to Quantum Mechanics.* Pearson Prentice Hall, 2nd edition, 2005.

[22] H. Guerlac. *Selected Readings in the History of Science*, volume 2. Cornell University, 1953.

[23] K. Huang and C. N. Yang. Imperfect bose gas with hard-sphere interaction. *Phys. Rev.*, 105, 1957.

[24] K. Huang and C. N. Yang. Quantum-mechanical many-body problem with hard-sphere interaction. *Phys. Rev.*, 105, 1957.

[25] K. Huang, C. N. Yang, and T. D. Lee. Eigenvalues and eigenfunctions of a bose system of hard spheres and its low-temperature properties. *Phys. Rev.*, 106(6), 1957.

[26] D. A. Huse and E. D. Siggia. The density distribution of a weakly interacting bose gas in an external potential. *Journal of Low Temperature Physics*, 1982.

[27] W. Ketterle, D. Durfee, and D. Stamper-Kurn, editors. *Making, probing and understanding Bose-Einstein condensates.* Contribution to the proceedings of the 1998 Enrico Fermi summer school on Bose-Einstein condensation in Varenna, Italy., April 1999.

[28] H. J. Metcalf and P. van der Straten. *Laser Cooling and Trapping.* Springer, 1999.

[29] A. Migdall, J. V. Prodan, W. D. Phillips, T. H. Bergeman, and H. J. Metcalf. First observation of magneticall trapped neutral atoms. *Phys. Rev. Lett.*, 54:2596 – 2599, 1985.

[30] S. H. Nasr. *Three Muslim Sages.* Caravan Books, 1976.

[31] C. J. Pethick and H. Smith. *Bose-Einstein Condensation in Dilute Gases.* Cambridge University Press, 2002.

[32] W. D. Phillips and H. Metcalf. Laser deceleration of an atomic beam. *Phys. Rev. Lett.*, 48:596 – 599, 1982.

[33] J. V. Prodan, A. Migdall, W. D. Phillips, I. So, H. Metcalf, and J. Dalibard. Stopping atoms with laser light. *Phys. Rev. Lett.*, 54:992 – 995, 1985.

[34] J. V. Prodan, W. D. Phillips, and H. J. Metcalf. Laser production of a very slow monoenergetic atomic beam. *Phys. Rev. Lett. 49*, 49:1149 – 1153, 1982.

[35] I. I. Rabi. Space quantization in a gyrating magnetic field. *Phys. Rep.*, 51(652), 1937.

[36] R. Roseman and S. Katzoff. The equation of state of a perfect gas. *J. Chem. Ed.*, page 350, June 1934.

[37] D. V. Schroeder. *An Introduction to Thermal Physics.* Addison Wesley Longman, 2000.

[38] D. A. Steck. Rubidium 87 d line data. Los Alamos National Laboratory, September 2001.

[39] W. Thomson. On an absolute thermometric scale founded on carnot's theory of the motive power of heat, and calculated from regnault's observations. *Cambridge Phil. Soc. Proc.*, June 5 1848.

[40] D. F. Walls and G. J. Milburn. *Quantum Optics.* Springer, 2nd edition, 1995.